MONASH University

Digital Signal Processing for Short-Haul Optical OFDM

Qibing Wang

B. Eng Chengdu University of Information Technology
M. Eng Institute of Microelectronics of Chinese Academy of Sciences

A thesis submitted for the Degree of Doctor of Philosophy at Monash University in 2018

Department of Electrical and Computer Systems Engineering,
Monash University, Clayton, Australia

Copyright Notice

Abstract

Driven by applications such as high-definition TV, videos and cloud computing, new datacenters are being established in recent years. Transmission speed becomes a bottleneck for intra- and inter-datacenter connections, whose distance is usually less than 100 km. As optical fiber is still the best choice for distances greater than tens of meters, new modulation schemes are required to be developed to further upgrade the data rate in short-haul optic-fiber links. Intensity modulation combined with direct-detection using directly modulated lasers is preferred in short-haul fiber-optical links, due to its low cost and compact size.

Orthogonal frequency division multiplexing (OFDM) is widely adopted in commercial RF-wireless systems. However, DC bias is required when OFDM signals are modulated on the intensity of optical carrier, because OFDM signals are bipolar. This method is called optical DC-biased OFDM (DCO-OFDM). The main drawback for DCO-OFDM is its low power efficiency due to the DC bias. Asymmetrical clipped optical OFDM (ACO-OFDM), which only uses the odd subcarrier to carry data, and pulse-amplitude-modulated optical DMT (PAM-DMT), which only uses the quadrature components of OFDM subcarriers, have been proposed to improve the power efficiency of DCO-OFDM. However, by sacrificing half of its spectral efficiency, they require either the bandwidth of the electrical and optical devices to be doubled, or higher-order constellations requiring higher signal to noise ratios to be used. Recently, layered asymmetrically clipped OFDM (LACO-OFDM) and augmented-spectral-efficiency DMT (ASE-DMT) have been proposed to improve the spectral efficiency of ACO-OFDM and PAM-DMT towards that of DCO-OFDM, while still maintaining their power advantage.

This thesis investigates these power-efficient OFDM algorithms (ACO-OFDM, LACO-OFDM, ASE-DMT) and their efficient implementation. All these power-efficient OFDM signals were generated in real-time using a FPGA and a DAC. By using real-time oscilloscope and offline digital signal processing in MATLAB, their signal quality was measured and analysed in a short-haul fiber-optic link.

First of all, the project has developed an efficient implementation of ACO-OFDM transmitters, by discarding the Hermitian symmetrical limits and taking advantage of all the zero-valued inputs on the IFFT. Real-time signal generation of ACO-OFDM based on Hermitian symmetrical and non-Hermitian symmetrical IFFT's inputs have been demonstrated separately and compared. The signal quality for both the two schemes is very similar after transmission over 15-km standard single-mode fiber (SSMF).

Then the power-efficiency of LACO-OFDM is verified by simulation and offline signal processing in an experiment. The results show that LACO-OFDM

iv

can reach the maximum transmission performance with a lower DC bias. Furthermore, a *middle-out* IFFT is proposed to generate the waveforms of all layers for LACO-OFDM simultaneously, by mapping the data of all the layers into a single IFFT's input and extracting the waveforms of higher layers within this IFFT before they pollute each other. By using this *middle-out* IFFT, a real-time generated LACO-OFDM signal has been successfully transmitted over 20-km SSMF for QPSK and 10-km SSMF for 16-QAM.

Finally, a modified *middle-out* IFFT is proposed for the generation of ASE-DMT signals, because ASE-DMT is also based on the layer concept to increase spectral efficiency. As the subcarriers in each layer for ASE-DMT only use inphase or quadrature component to carry data, the PAM signals with their Hermitian or skew-Hermitian counterparts are mapped into the imaginary parts of a single IFFT. By extracting waveforms of high layers within the IFFT to avoid pollution by waveforms from other layers, each layer's waveform can be obtained from the IFFT's inphase or quadrature components. By using this *middle-out* IFFT, a real-time generated ASE-DMT signal has been successfully transmitted over 20-km SSMF for PAM2 and 10-km SSMF for PAM4.

The developments in this thesis enable layered OFDM techniques to be efficiently implemented in transmitters, giving signals that are both spectrally and power efficient.

Declaration of Authorship

This thesis contains no material which has been accepted for the award of any other degree or diploma at any university or equivalent institution and that, to the best of my knowledge and belief, this thesis contains no material previously published or written by another person, except where due reference is made in the text of the thesis.

Signed:

_____

Print Name:

_____

Date:

_____

Acknowledgements

First of all, I would like to thank Prof. Arthur Lowery for giving me this opportunity to do the research of optical communication in Electro-photonics Lab in Monash University. The research under his supervision over the past four years was challenging and exciting. I still remember those disappointed moments that hard work came to nothing in the first year. Thanks for his valuable suggestions and kind help, my research was finally on the right track. Furthermore, I also want to thank him for giving me so many chances to present my work on several conferences. These experiences help me grow rapidly in academia. Besides, I also would like to thank Prof. Emanuele Viterbo for his timely revision of my thesis.

I also cordially thank to the research fellows in Electro-photonics Lab - Dr. Chen Zhu, Dr. Bill Corcoran, Dr. Leimeng Zhuang, Dr. Valery Rozental and Dr. Deming Kong for their help. They were always willing to give me a hand whenever I was at a loss for my research. I really learned a lot from the discussions we had. Special thanks to Dr. Damien Browne and Dr. David Boland. Without their kind help, I cannot open the door of FPGA in a very short time.

I am also grateful to my colleagues and friends - Binhuang Song, Benjamin Sze-Ming Foo, Yiwei Xie, Jignesh Jokhakar, Zihan Geng, Tianyu Wang, Yanming Pei, Qianyu Jin, Yeqing Hu, Taiyang Wu, Xiaoqin Wang and Xuepeng Xiao. Thanks for your help and suggestions during my PHD candidature. The friendship we built will be the invaluable wealth in my life.

I also want to thank Prof. Xin Yin from Ghent University to give me an opportunity to have an intern in IMEC in Belgium. During this internship, I learned a lot of knowledge in the circuit design, which broadened my horizon in optical communication.

Besides, I want to thank the support from scholarship of Australian Research Council's Laureate Fellowship (FL130100041), which helps me fully concentrate on my research over the past four years.

Finally, great thanks to my family. Your care and encouragement is always inspiring me to move forward. I wish you a good health and the very best luck in everything.

Contents

List of Figures

xviii

List of Tables

Chapter 1

Introduction

1.1 Optical Communication - A Historical Perspective

As shown in Fig. 1.1, Cisco estimates that the total global Internet traffic will rapidly increase up to 278 Extrabytes by the year of 2021 [1]. At present, except for optical fibers, no other known transmission medium can support such a huge demand for higher and higher data rates. The birth of optical fibers can be dated back to 1960s [2]. However, at that time, these optical fibers were not considered for optical communications due to their huge loss. In 1966, Charles Kao suggested that the loss of optical fibers could be reduced drastically by improving the impurity of silica glass [3]. In 1970s, researchers from Corning reported a fiber with a loss of only 4 dB/km in the wavalength region around 630 nm [4], but it was exceeded soon by a record low loss of 0.2 dB/km in the wavelength region around 1.55 μm [5]. Besides low-loss optical fibers, the invention of GaAs semiconductor lasers, which were very compact and able to couple efficiently into single-mode optical fibers [6], enabled the rapid development of fiber-optic communication systems [7].
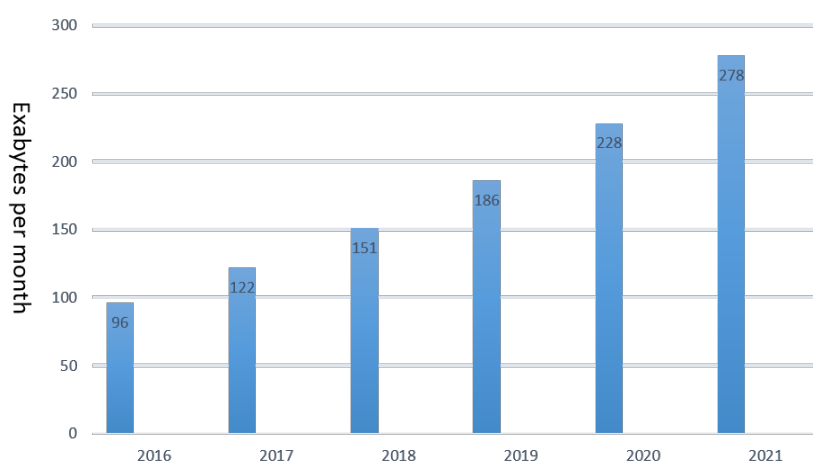
FIGURE 1.1: The growth trend of total global Internet traffic [1].

Intensity modulation with on-off keying (OOK) combined with direct detection dominates the optical communications in the early years. The first research peak of coherent receivers occurred in the late 1980s motivated by the fact that the higher receiver sensitivity of coherent receiver could enhance the unrepeated transmission distance [8]. However, the invention of erbium-doped fiber amplifier (EDFA) interrupted this research effort into coherent receivers, because the signal to noise ratio (SNR) in the total transmission link was mainly determined by the accumulated amplified spontaneous emission from the EDFAs [9]. Besides, EDFAs can amplify a large wavelength range across the C-band simultaneously, supporting wavelength division multiplexing (WDM). WDM allows multiple data streams to be transmitted simultaneously over a single fiber by using multiple lasers with different wavelengths, with the help of optical multiplexers and demultiplexers. Therefore, WDM technique was widely exploited to increase the system capacity in 1990s due to its simplicity and relatively low cost, compared with coherent receiver [10].

From the 2000s, the coherent receiver was revived owing to the motivation to improve the spectral efficiency by using higher-spectral efficient modulation formats such as QPSK, 16-QAM and so on. Coherent receivers are able to operate at lower optical signal-to-noise ratios (OSNRs) than direct detection or equivalently, provide higher electrical SNRs for a given OSNR [11]–[13]. A 40-Gb/s differential quadrature phase-shift keying (DQPSK) transmission experiment was demonstrated in 2002 by using optical IQ modulation and optical delay detection [14]. Research on coherent receivers then reached another peak with the adoption of the high-speed digital signal processing (DSP) to compensate for chromatic dispersion (CD) and polarization-mode dispersion (PMD). Due to the fast improvement of microelectronic technology according to the Moore's Law, an application specific integrated circuit (ASIC) was developed and successfully demonstrated in a transmission system at a bit rate of 40 Gb/s [15]. The combination of coherent detection and DSP lay the foundation for current long-haul optical communication systems. Now, 100 Gb/s transmission systems, employing DSP assisted QPSK polarization-division multiplexing coherent transceivers, have been deployed [16], [17].

In the meantime, optical orthogonal frequency division multiplexing (OFDM) also gained attention due to its huge success in the wireless communication community. In 2006, Lowery *et al.* reported a dispersion-compensation technique in a direct-detection optical OFDM (DDO-OFDM) system [18]. Almost simultaneously, coherent optical OFDM (CO-OFDM) was proposed by Shieh *et al.* to compensate for the accumulated dispersion in the transmission over the fiber [19].

DDO-OFDM has a simple receiver but lower spectral efficiency and sensitivity. Correspondingly, CO-OFDM shows a higher spectral efficiency but a more complex receiver. Over 100 Gb/s optical transmission experiments has been successfully demonstrated in DDO-OFDM [20]–[22] and CO-OFDM systems [23]–[25].

In Fig. 1.2, the Ethernet speeds have been increased up to 400 GbE, a factor of 40 above 10 GbE used in the early 2000s. However, in contrast to widely employed coherent receivers for long-haul optical communication system, intensity modulation and direct detection is still preferred in short-haul fiber-optic links due to its compact size and relatively lower cost. Actually, even for now, it is doubtful that coherent receivers will be used in short-haul fiber-optic links in the near future [26].
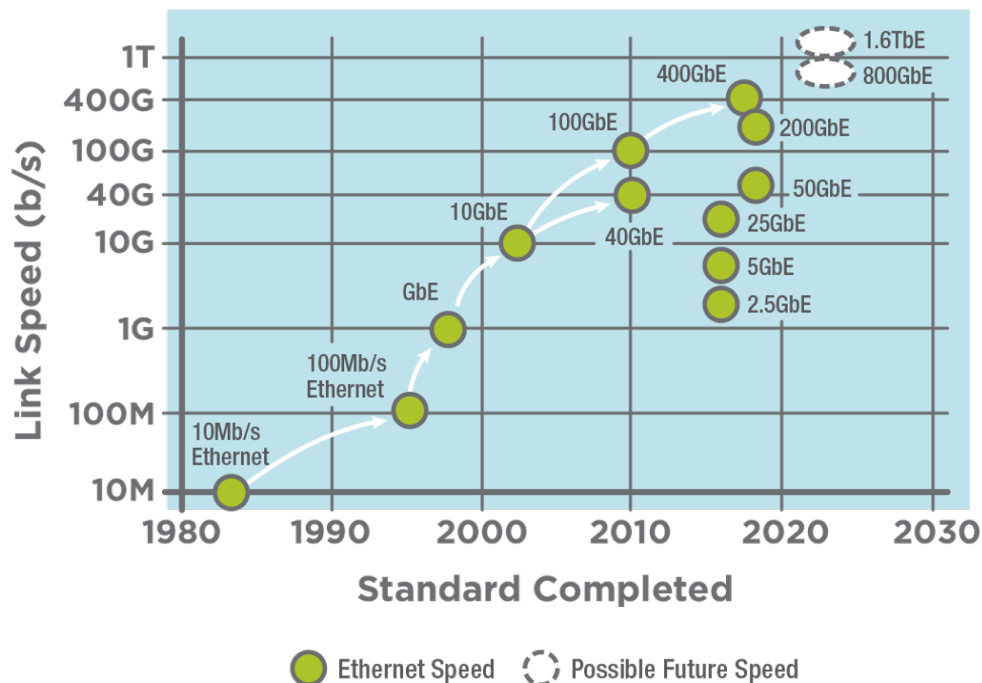
FIGURE 1.2: The Ethernet link speed roadmap [27] (Permission granted from Ethernetalliance).

1.2 Power Consumption in Optical Communication Systems

It has been estimated that up to 50 billion devices will be connected to the internet by 2020. Driven by the Internet of Things, datacenters will be one of the biggest energy consumers on the planet, accounting for 33% of the overall power consumption of information and communication technology [28], as shown in Fig. 1.3. Therefore, the power consumption in optical communication

system becomes a great concern and requires more consideration in the initial design. Tucker has analysed the energy consumption in the optically amplified fiber transmission links [29]. In this paper, he shows that the energy efficiency in the transmission system is being continuously reduced by around 20% per year, in terms of energy consumption per bit, as shown in Fig. 1.4 .
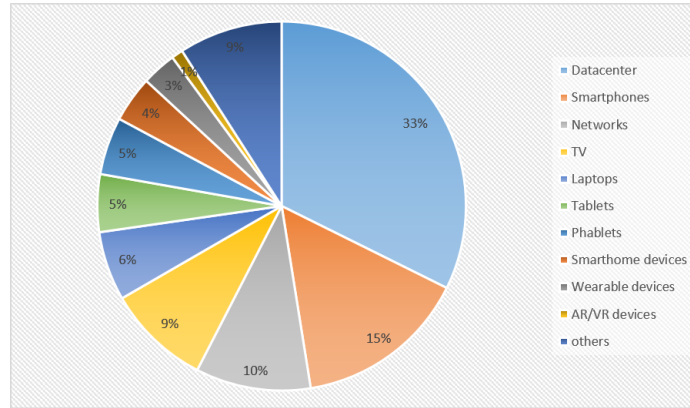
FIGURE 1.3: Energy consumption for datacenters in 2025 [28].
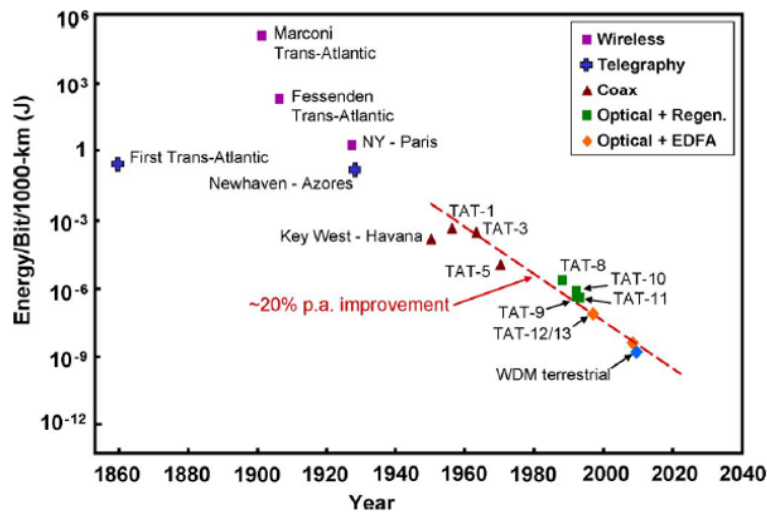
FIGURE 1.4: Energy per bit per 1000 km of transmission distance for various transmission systems [29] © 2010 IEEE.

Advanced modulation formats, such as M-ary quadrature amplitude modulation (M-QAM), promise enhanced spectral efficiency to increase the capacity for a fixed bandwidth [30]. Future photonic technology not only needs to continue to increase the data rates for a given amount of bandwidth, but also to reduce its energy consumption per bit. However, the generation of higher-order modulation formats, such as M-QAM, currently relies either on high-speed digital-to-analog converters (DAC) and linear electrical amplifiers or other dedicated electronic circuitry to generate drive signals. These electrical devices, such as DACs and

modulator drivers, which are required in the generation of M-QAM and OFDM optical modulation signals, are quite power hungry [29], [31]. Green optical transmitters can be achieved by using attenuators and power combiners as DACs [32], [33], multiple IQ modulators [34]–[36], or segmented modulators [37]–[40].

DSP is also playing an important role in current optical communication system. Traditionally, the power consumption of ASICs is being reduced by the reduction of the feature size of transistors, which is more and more difficult to approach nm-gate lengths. Therefore, its power consumption also requires attention in the initial design [41]–[46]. In the conventional hardware design, functional blocks are often reused serially to reduce the logic resource utilization [47]–[50]. However, this technique is hard to find its application in the DSP for optical communication systems, because the time delay resulting from the logic resource reusage will lead to a significantly reduction of the total data throughput. Put another way, parallelism is essential for achieving high throughput [51]. An end-to-end energy analysis in long-haul coherent transmission systems provided a very detailed model that not only includes all the significant functional blocks such as timing and carrier recovery, chromatic and polarization mode dispersion compensation and Forward Error Correction (FEC), but also took into account the impact of the number of samples processed every clock cycle and of operations other than multiplications [31]. Pfau *et al.* proposed a hardware-efficient implementation method for a novel carrier recovery algorithm for arbitrary M-QAM constellations in an intradyne coherent optical receiver [52]. A more complete and detailed analysis of power consumption for DSP-ASICs was shown by Kuschnerov *et al.* [53]. In this paper, several possible methods to reduce the power consumption in high-level algorithm design, register-transfer level (RTL) and physical design were discussed.

For optical OFDM systems, Lowery and Armstrong proposed the asymmetrical clipped optical OFDM (ACO-OFDM) to improve the power efficiency by avoiding the DC bias [54], [55]. Using the similar asymmetrical clipping method, pulse-amplitude-modulated discrete multitone modulation (PAM-DMT) was proposed later with only the imaginary parts of OFDM subcarriers to encode data [56]. Flip OFDM is another power-efficient optical OFDM algorithm, which can avoid using DC bias by transmitting both the positive values and inverted negative values of one OFDM frame in two OFDM symbol slots [57], [58]. By combining these techniques, many power efficient optical OFDM systems were developed later [59]–[62]. However, all these algorithms have to sacrifice some spectral efficiency in exchange for the increase of power efficiency. Recently, layered ACO-OFDM (LACO-OFDM) and augmented-spectral-efficiency DMT (ASE-DMT) were

proposed, which theoretically can achieve the same spectral efficiency as DC-biased optical OFDM (DCO-OFDM) while maintaining their power advantage without requirement of DC bias [63]–[68].

1.3   Resarch Motivation

The thesis explores and develops several efficient optical OFDM transceivers for short-haul fiber-optic links. Both the logic resource utilization and optical power consumption due to the DC bias required in the optical OFDM system are discussed and optimized.

The key components in OFDM system are inverse fast Fourier transforms (IFFTs) and fast Fourier transforms (FFTs). However, many papers suggest that the Hermitian symmetrical inputs are required for the IFFT to obtain a real-valued outputs, which wastes logic resources. Therefore, the first part of my research focused on the efficient implementation of IFFT and FFT in the transceiver. By using non-Hermitian symmetrical inputs, I experimentally demonstrated a real-time ACO-OFDM transmitter, only requiring a half-size IFFT. Besides, A further optimization was also proposed, which eliminated the constant zero-valued logic resources.

Although LACO-OFDM has been simulated to show that it is more power-efficient than DC-biased optical OFDM (DCO-OFDM) in terms of power consumption per bit, the experiments have not been demonstrated to verify this conclusion. Therefore, the second part of my research investigated the power efficiency of LACO-OFDM in an experimental optical transmission link. Besides, the increased number of IFFT/FFTs in the LACO-OFDM brought serious challenge in the implementation because one IFFT/FFT itself occupied most of the logic resources of the DCO-OFDM transceiver. I firstly proposed to generate LACO-OFDM signal by using only one *middle-out* IFFT, simplifying the implementation of LACO-OFDM transmitter. Besides, the transmission performance of LACO-OFDM was measured and analysed in a real-time transmission link using FPGA.

As the ASE-DMT also uses the layered concept to increase the spectral efficiency, it also needs several IFFTs in the transmitter. Therefore, its efficient implementation method and transmission performance are also required to be exploited. A similar *middle-out* IFFT was proposed to optimize the implementation of ASE-DMT transmitter, followed by a real-time signal generation using FPGA. Then the transmission performance over fiber was measured. The results gave us some idea about its feasibility to be commercialized by using all the off-the-shelf

components and techniques, which could not be indicated by using offline signal processing.

1.4 Thesis Contributions

The original contributions of this thesis are as follows:

- Chapter 3: The first real-time demonstration for an efficient ACO-OFDM transmitter without Hermitian symmetrical constrained inputs. By discarding the Hermitian symmetrical inputs for the IFFT, the size of IFFT is reduced by half. Furthermore, by taking advantage of the zero-inputs in the ACO-OFDM transmitter, the overall implementation cost is reduced by 68%. (From Publication 6)

- Chapter 4: The first real-time computationally efficient LACO-OFDM transmitter is experimentally demonstrated using an FPGA and DAC. A method is proposed that only needs one *middle-out* IFFT to generate the waveforms for all the layers. The transmission performance over fiber is measured and analyzed. (From Publications 1, 3, 5, 8)

- Chapter 5: The first real-time experimental demonstration for a computationally efficient ASE-DMT transmitter using only one *middle-out* IFFT. Compared with LACO-OFDM, a different mapping method for the *middle-out* IFFT is proposed. Besides, I also evaluate the power budget and analyse the limiting factor on the Q-factor performance in this experiment. (From Publications 2, 7)

1.5 Publications

1.5.1 Journal Papers

1. **Q. Wang**, B. Song, B. Corcoran, D. Boland, C. Zhu, L. Zhuang, and A. J. Lowery, "Hardware-efficient signal generation of layered/enhanced ACO-OFDM for short-haul fiber-optic link," Opt. Express, vol. 25, no. 12, pp. 13359-13371, 2017.

2. **Q. Wang**, B. Song, B. Corcoran, L. Zhuang, and A. J. Lowery, "Real-Time Demonstration of Augmented-Spectral-Efficiency DMT Transmitter using a Single IFFT," Journal of Lightwave Technology, vol. 35, no. 21, pp. 4796-4803, 2017.

3. B. Song, C. Zhu, B. Corcoran, **Q. Wang**, L. Zhuang, and A. J. Lowery, "Experimental layered/enhanced ACO-OFDM short haul optical fiber link," IEEE Photon. Technol. Lett., vol. 28, no. 24, pp. 2815-2818, 2016.

4. B. Song, B. Corcoran, **Q. Wang**, L. Zhuang, and A. J. Lowery, "Subcarrier pairwise coding for short-haul L/E-ACO-OFDM," IEEE Photon. Technol. Lett., vol. 29, no. 18, pp. 1584-1587, 2017.

1.5.2   Conference Papers

5. **Q. Wang**, B. Song, B. Corcoran, D. Boland, L. Zhuang, Y. Xie, and A. J. Lowery, "FPGA-based layered/ehanced ACO-OFDM transmitter," in *Optical Fiber Communications Conference and Exhibition (OFC)*, 2017, pp. Tu3D.6. Optical Society of America, 2017.

6. **Q. Wang**, B. Song, B. Corcoran, L. Zhuang, A. Lowery, "Efficient IFFT implementation in an ACO-OFDM transmitter," in *Opto-Electronics and Communications Conference (OECC) and Photonics Global Conference (PGC)*, 2017, pp. 3-3K-4. IEEE, 2017.

7. **Q. Wang**, B. Song, B. Corcoran, L. Zhuang, and A. J. Lowery, "Single IFFT Augmented Spectral Efficiency DMT transmitter," in *Proc. Eur. Conf. Opt. Commun.*, 2017.

8. **Q. Wang**, B. Song, B. Corcoran, and A. J. Lowery, "Single-IFFT Real-Time Layered/Enhanced ACO-OFDM Transmitter," in *Optical Fiber Communications Conference and Exhibition (OFC)*, pp. W2A-50, Optical Society of America, 2018.

9. B. Song, B. Corcoran, **Q. Wang**, and A. J. Lowery, "Field-Trial of Layered / Enhanced ACO-OFDM," in *Proc. Eur. Conf. Opt. Commun.*, 2017.

10. Y. Xie, L. Zhuang, R. Broeke, **Q. Wang**, B. Song, Z. Geng and A. J. Lowery, "Compact 4×10 Gb/s Silicon-on-Insulator OFDM Transmitter," in *Optical Fiber Communications Conference and Exhibition (OFC)*, pp. W2A-9. Optical Society of America, 2017.

Chapter 2

Review of DSP in short-haul fiber-optic links

2.1 Introduction

Internet traffic is growing exponentially, driven by applications such as high-definition TV, videos and cloud computing. A report from Cisco, which has been shown in Fig. 1.1 in Chapter 1, forecasts that the global IP traffic per month will be 278 Exabytes in 2021, nearly tripled from 2016 to 2021 [1]. Therefore, many new datacenters with flexible scalability will be required in the near future. The fastest 100 Gb/s Ethernet data rate was standardized around 2010 and will fail to meet the heavily increased internet traffic soon. The 400G standard does not only increase the transmission speed, but also requires to reduce the cost and power consumption per bit. According to the trend of 4 and 10 times bit rate scaling per generation, the 400 Gigabit Ethernet (GbE) Study Group was launched in March 2013 [69], [70]. The latest 2018 roadmap was released in OFC 2018 [27]. The 400 GbE Task Force has agreed that the new short-haul fiber-optical link standards could cover the reaches of 100 m over multi-mode optical fiber (MMF), and 2 km, 10 km and 80 km over single-mode optical fiber (SMF). A large amount research on improving the data rate of optical transmission system has been performed [71]–[75], but the exploitation on optimal trade-offs between spectral efficiency, power consumption and transmission distance is still on-going.

For optical Ethernet, the current commercially available fastest lane rate is 25 Gb/s, beyond which is limited by the performance of low-cost optoelectronics [76]. Wavelength division multiplexing (WDM) is a natural choice for further data rate upgrades. That is to say, 400 GbE can be achieved by implementing 16 lanes (wavelengths or fibers), each operating at the existing 25 Gb/s rate. Apparently, this method requires four duplex fiber pairs, each connected to a 100GBASE-LR4 module with four WDM lanes per fiber. This solution seems very

straightforward, but it quadruples the cost and power dissipation of 100GBASE-LR4. In order to address the cost and power issues of 400 GbE, the first generation of 400GbE has a large possibility of using 8 lanes with 50 Gb/s per lane or 4 lanes with 100 Gb/s per lane. Therefore, NRZ and PAM4 at 50 Gb/s and OFDM at 100 Gb/s per wavelength will be promising candidates [77]. In contrast to long-haul optical fiber links using external modulation and coherent detection, IM/DD using directly modulated lasers (DML) is preferred in short-haul optical systems due to its low cost and compact size [78]–[80]. DMT technology is one of the OFDM based modulation formats. It transmits data using only the intensity and does not encode data on the optical phase, so it is very suitable for short-haul optical communication systems. Besides, carrierless amplitude and phase modulation (CAP) are also demonstrated as a potential candidate [81], [82].

This Chapter begins with the review on the suitable modulation formats for short-haul fiber-optic links. Then the optical OFDM systems, especially those power-efficiency optical OFDM algorithms, will be presented. Finally, the real-time experimental demonstrations for optical OFDM transmission systems are generally described.

2.2   Optical Communication Systems

Fiber optic communication links can be grouped into coherent detection and direct-detection systems.

Coherent optical communication systems have been widely used in the long-haul optical transmission link due to its higher spectral efficiency and tolerance to linear transmission impairments such as CD and PMD [83]–[86]. At OFC 2018, AT&T labs reported the first end-to-end 400G field trials in a commercial coherent optical transmission link [75]. The basic coherent optical transceiver is depicted in Fig. 2.1. The DSP in the transmitter potentially includes Nyquist spectral shaping, signal pre-distortion, FEC coding and IFFT. Two DACs convert the digital data into multi-level analog signals to drive the IQ modulator. In the receiver, a local optical oscillator (LO) is required as a reference for the phase information of the complex optical signal. Balanced photodiodes mix the incoming signal with the LO. A pair is used for I and another for Q. The balanced detection technique reduces the beat noise between the signal and the LO. DSP is performed in the electrical domain and can fully compensate the CD because all the information on the complex amplitude of the transmitted optical signal is preserved. Furthermore, polarization-division-multiplexing (PDM) can be used to double the data

rate and the corresponding PMD can also be eliminated by using the DSP in the receiver [87]–[89].
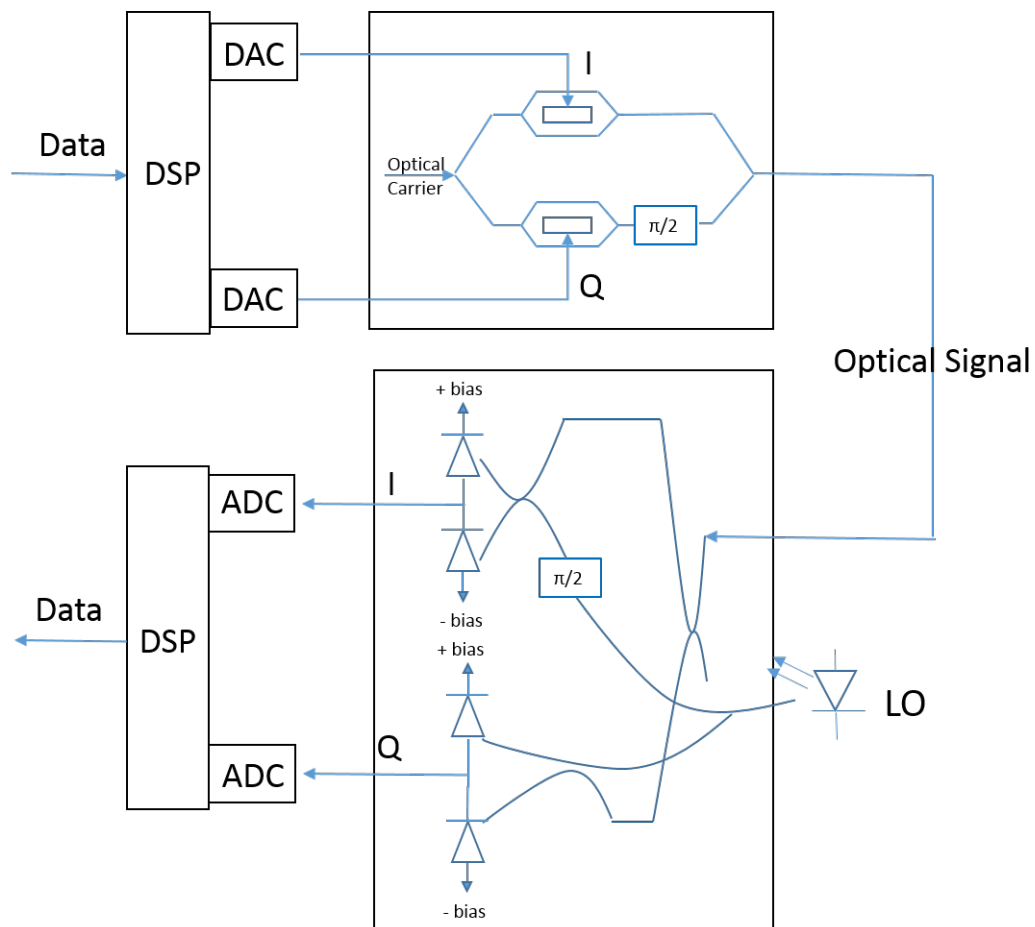
FIGURE 2.1: Configuration of a single-polarization coherent optical transceiver. In the transmitter, the signal is processed by DSP before driving the IQ modulator. In the receiver, the outputs from the phase-diversity homodyne receiver are processed by DSP.

In the OFC 2018, the workshop named that 'DSP for Short Reach and Client Optics - What Makes Sense?' was organized to provide a platform for discussion on the right balance of cost- and power-efficient optical interface and channel equipment [26]. The required electronics-based transmitter- and receiver-side DSP techniques were also discussed as we headed towards 400Gb/s and 1Tb/s interfaces in the short-haul transmission system. Most researchers agreed that coherent techniques would finally dominate the short-haul in the future, but intensity modulation combined with direct detection, is still the first choice due to its cost and compact size at present [90]. A simple IMDD based optical transmission link is shown in Fig. 2.2. The main difference to coherent transceiver is that only the intensity of the laser is used to carry data by modulating the light source drive current to generate a varying optical output power. Its main drawback is

the phase information of the optical signal is discarded at the receiver, so the CD cannot be equalized. However, owing to the requirement of only one photodiode (PD) and no local oscillator, a compact and cheap transceiver can be achieved. Therefore, it still dominates the short-haul fiber-optic transmission links [91].
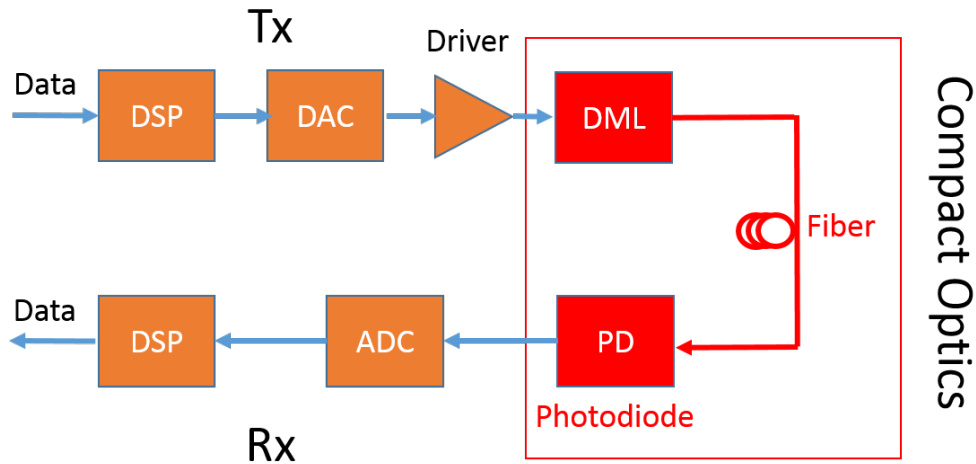
FIGURE 2.2: Configuration of IMDD based optical OFDM transmission link. The analog drive signal from DAC is used directly to drive the intensity of the laser. Only one PD is required in the receiver. DML: directly modulated lasers.

2.3 Modulation Techniques

This section reviews the modulation techniques being used or considered for short-haul optical transmission links.

2.3.1 OOK

On–Off Keying (OOK), where the 1 is represented by the presence of the light while the 0 by the absence of the light, is a traditional modulation format and traditionally used in the 10 GbE [7], [30]. As is shown in Fig. 2.3, the transmitted signal is a two-level binary data stream consisting of either a 0 or 1 in a time slot of duration of T_b, which is named as a bit period. A PD in the receiver can only detect the power of optical signal, which is all OOK requires. In 2016, Bae *et al.* demonstrated a 51.56-Gb/s OOK transmission experiment over 15-km standard single-mode fiber (SSMF) by using a directly modulated laser (DML), which achieved the longest transmission distance in C-band at a data rate of >50-Gb/s

for OOK [92]. However, as only a single bit of information is carried in each symbol, its electrical spectral efficiency is never better than 2 bit/s/Hz. Given that the commercial available lasers have bandwidths < 15 GHz, this limits the data rate of 30 Gbps. Therefore, OOK is not practical for the further speed upgrade of Ethernet, but it can be used as a comparison with other modulation formats.
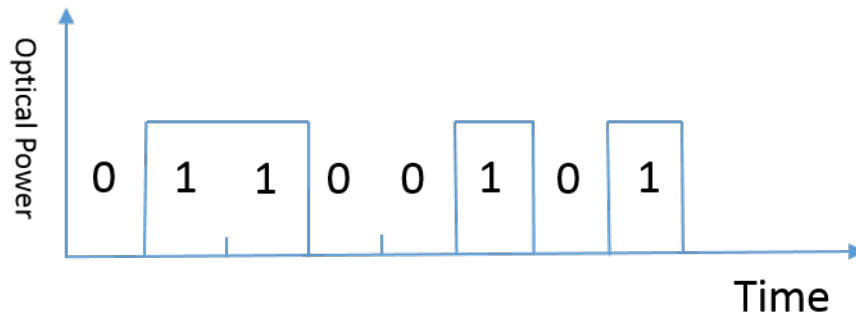
FIGURE 2.3: Ideal OOK modulation using non-return-to-zero (NRZ) signal. The 1 is represented by the presence of a light while the 0 by the absence of a light.

2.3.2 PAM4

Pulse-amplitude-modulation with four amplitude levels (PAM-4) has been proposed to double the spectral efficiency of OOK by carrying 2 bits of information in one symbol period, as shown in Fig. 2.4. Amplitude levels 0, 1, 2, and 3 represent two bits 00, 01, 11, and 10, respectively [93]. When one of the four amplitudes is transmitted in a symbol period, there are two bits transmitted in parallel, so the data rate is doubled in the same bandwidth. In other words, PAM-4 modulation is twice as spectrally efficient as OOK modulation. However, PAM4 incurs near to 5-dB sensitivity penalty over OOK transmission at the same symbol rate, so it calls for FEC and higher launch powers to achieve the necessary link budget [94]. This is because the additional voltage levels with PAM-4 increase the average power by a factor of 3, and therefore for a fixed receiver power, PAM-4 is more susceptible to noise than a binary digital signal. Despite the fact that there are many other modulation techniques that can also double or triple the transmission capacity for a fixed bandwidth, PAM-4 modulation has been a leading solution, mainly due to its simplicity. PAM4 has been regarded as one of the most promising modulation techniques for 100G and beyond optical pluggable transceivers in both intra- and inter-datacenter optical links by the IEEE P802.3bs standard [27], [90], [95]. Many PAM4 transmission experiments have been demonstrated using off-line DSP in both transceivers [96]–[100]. In 2016, Zhang *et al.* experimentally

demonstrated the generation and transmission of a single-lane 180 Gbit/s PAM-4 over a 2-km SSMF with a record-high net data rate of 150 Gbit/s in C-band [101].
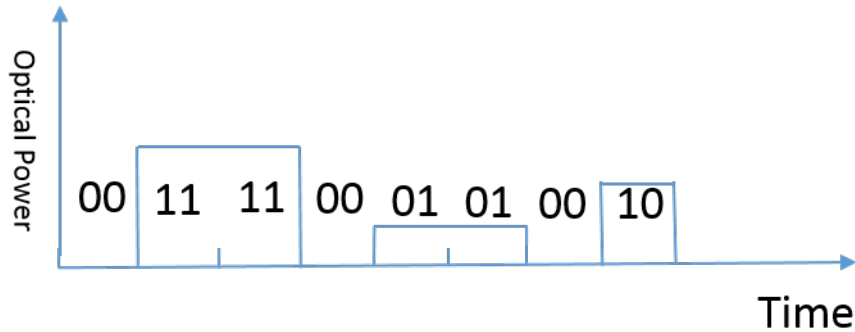
FIGURE 2.4: PAM-4 modulation. The 4 different amplitudes of the light represent 00, 01, 10 and 11 separately.

2.3.3 CAP
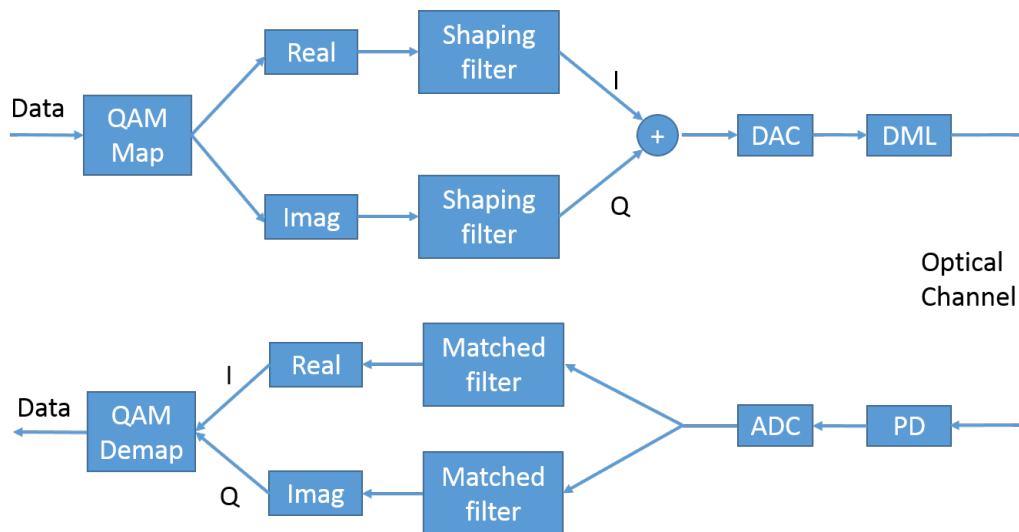
FIGURE 2.5: DSP configuration for CAP transmission system. The shaped filter consists of a square-root raised cosine shaping filter multiplied by a sine and a cosine respectively.

Carrierless amplitude and phase (CAP) modulation is another modulation format that is suitable for IMDD based optical transmission link [77], [81], [82], [102], [103]. It provides improved spectral efficiency by transmitting two orthogonal channel signals (I and Q) simultaneously. In contrast to coherent QAM modulation, CAP does not rely on a carrier, but uses filters with orthogonal waveforms to differentiate between I & Q data streams. As shown in Fig. 2.5, the QAM

modulated signal is separated into I and Q channel, which then are filtered with orthogonal waveforms before adding them together to get a real signal streams. In the receiver, two matched filters are used to separate the I and Q channels before demodulation. The main advantage of CAP modulation is its possibility of an analog implementation. Besides, CAP is more robust in terms of SNR and multipath interference compared with DMT. In 2014, Olmedo *et al.* experimentally demonstrated a total data rate of 102 Gb/s in a single wavelength using multiband CAP modulation [104]. In 2018, Shi *et al.* experimentally demonstrated a record-high 112 Gbit/s per lane CAP transmission over 480-km SSMF [105].

2.3.4 DMT

Instead of employing a single subcarrier at a very high symbol rate, several subcarriers at a low symbol rate can be combined to generate a single signal with a high bit rate. As the symbol rate is quite low for each channel, the signal has a high tolerance to ISI resulted from the channel dispersion. This multicarrier modulation technique is called OFDM. A lot of research related to optical OFDM has been done in long-haul optical fiber communication systems, which can be simply categorized as direct-detection optical OFDM [20], [105]–[111] and coherent optical OFDM [19], [112]–[115]. In contrast to long-haul optical fiber links using external modulation and coherent detection, direct detection using only one PD is preferred in short-haul optical systems [116]–[118].
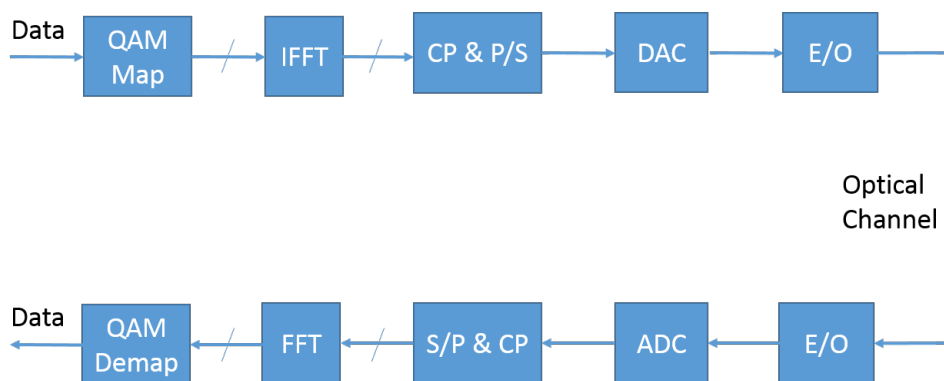
FIGURE 2.6: DSP configuration for DMT transmission system. IFFT and FFT is the core DSP, which can achieve modulation/multiplex and demodulation/demultiplex digitally.

Optical OFDM is often called DMT in short-distance optical links [119]–[123]. Compared with the previous modulation formats, optical OFDM can be transmitted over a longer fiber due to its resilience to intersymbol interference (ISI) and intercarrier interference (ICI) by prepending cyclic prefix (CP) in front of

every OFDM symbol. Besides, DMT can adapt its modulation formats of different subcarriers through bit-loading and power-loading to avoid dispersion-induced nulls in the link's baseband frequency response. This thesis does not distinguish DMT and OFDM, though DMT is often used to imply OFDM with bit- and power-loading [121], [124]. They are used interchangeable throughout the thesis.

As shown in Fig. 2.6, the DMT signal is firstly generated in electrical domain and then up-converted to the optical domain. The inputs on the IFFT are Hermitian symmetrical, in order to make the IFFT outputs to be real-valued. In the receiver, the signal is firstly down converted to the electrical domain, followed by an FFT before demapping. Because DMT is an ITU standard for ADSL and currently the dominant modulation format for digital subscriber lines, a lot of research has been done to explore its possibility to be used in IMDD based optical transmission links [125]–[133].

2.4   Power-Efficient Optical OFDM

As shown in previous sections, in order to modulate the intensity of optical signal, DC bias is required to convert bipolar OFDM signal to a unipolar one with no negative values. However, the DC bias is not necessary because it is only used for converting a negative signal value to a positive one, and thus carries no data. Therefore, much research has been carried out to improve the power efficiency of DC-biased optical OFDM (DCO-OFDM) [54]–[56], [58]. These schemes are called power-efficient optical OFDM in this thesis. By saving the DC power, the optical SNR (OSNR) in an optical power limited system will be improved. In this section, the recent development of power-efficient optical OFDM/DMT transmission system is discussed.

2.4.1   ACO-OFDM

One straightforward way to improve the optical power efficiency of DC-biased optical OFDM is to clip all the negative values to be zero-valued. However, the clipping distortion is unable to be removed in the receiver, leading to a significantly reduced SNR. Actually, in most cases, the data cannot be recovered. Using the same idea that clipping all the negative values to be zero-valued, ACO-OFDM has been proposed [55], but with control of the clipping distortion's frequency distribution.

Lowery and Armstrong proposed to add a gap between the OFDM subcarrier band and DC component to accommodate the majority of clipping distortion [54]. This technique is called gapped ACO-OFDM. The gapped ACO-OFDM simulation system is shown in Fig. 2.7. A limiter (x >= 0) imitated the clipping process. All the negative waveform became zero-valued in the clipped drive waveform. The frequency gap was generated by packing zero inputs on the OFDM subcarriers. From the drive spectrum inset, the brick-wall OFDM spectrum and intermodulation distortion caused by the clipping procedure were clearly shown. It can be concluded that the clipping distortion have limited impact on the OFDM spectrum. This paper proved that zero bias gave gapped ACO-OFDM transmission system a better performance in a power-limited optical system because more optical power was allocated to carry the modulated optical signal, which translated to a stronger electrical signal in the receiver, resulting in a better SNR.
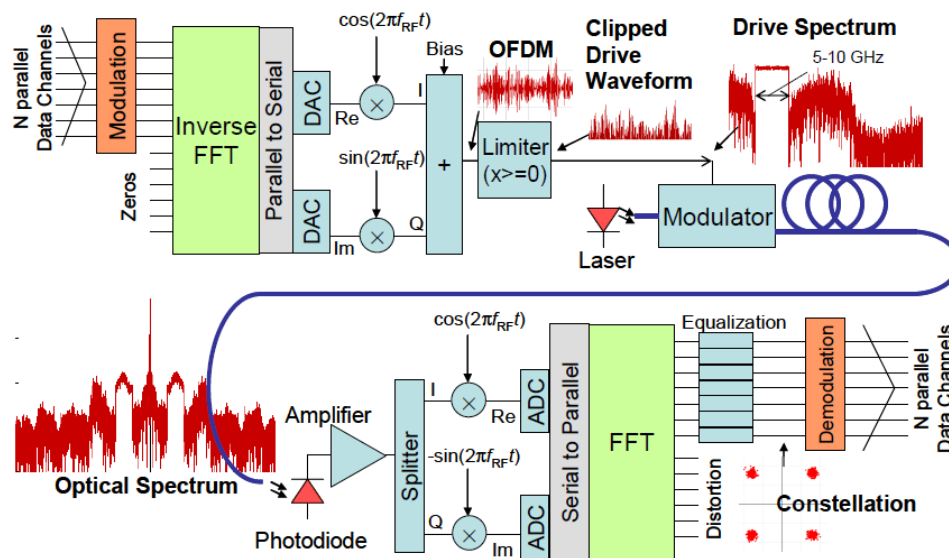
FIGURE 2.7: Gapped ACO-OFDM system block diagram including waveforms and spectra. Reprinted with permission from ref [54], [OSA].

Armstrong and Lowery proposed to use only the odd subcarriers to carry data. This technique is called odd-subcarrier ACO-OFDM [55]. The trick here is that all the clipping distortion only falls on the even subcarriers by clipping all the negative waveforms to be zero-valued, so the data in the odd subcarriers are not influenced by the clipping process. The odd-subcarrier ACO-OFDM algorithm will be detailed with a real-time experimental demonstration in Chapter 3.

2.4.2   PAM-DMT

Inspired by ACO-OFDM, Lee *et al.* proposed PAM-DMT by using only the quadrature components of all the subcarriers to carry data [56]. By clipping all the negative waveforms to be zero-valued, the clipping distortion in this scheme all falls on the inphase components. Now the waveform can be used to drive the intensity of the laser without requirement of DC bias. A simulation was carried out in this paper to prove that PAM-DMT has a similar receiver sensitivity as ACO-OFDM. Nevertheless, the PAM-DMT is more suitable for frequency-selective channels by using bit- and power-loading in all subcarriers. A detailed analysis of PAM-DMT will be presented in Chapter 5.

2.4.3   Flip Optical OFDM

In 2007, Yong firstly proposed Flip-OFDM for unipolar communication system by inverting the polarity of negative waveforms [57]. In 2012, Fernando *et al.* carried out a comprehensive analysis of Flip-OFDM in the general setting of a unipolar communication system and proposed a new detection enhancement scheme [58]. The block diagrams of flip-OFDM are shown in Fig. 2.8. After the parallel to serial conversion, a polarity separator was required for flip-OFDM. The negative parts were selected, inverted and then delayed by one OFDM symbol to be transmitted after the positive signal. Therefore, all the transmitted signal was positive, avoiding the requirement of DC bias. In the receiver, a time domain demultiplex was performed to separate two consecutive OFDM symbols, which were then combined with each other to recover the original OFDM symbols before serial to parallel conversion. Flip-OFDM achieves the same spectral efficiency as the ACO-OFDM because two OFDM symbol slots are required to transmit one actual OFDM symbol. However, their spectra are subtly different.

2.4.4   Multi-Format Optical OFDM Schemes

In all the above optical OFDM systems, including DCO-OFDM, ACO-OFDM, PAM-DMT and Flip-OFDM, the improvement of optical power efficiency is at the cost of reduction of spectral efficiency, which leads to a doubled bandwidth requirement of the electrical and optoelectronic components for a certain modulation format. Another alternative is to use a higher spectral efficiency modulation format, which needs a higher SNR, making it unattractive in the practical deployment. Therefore, by superimposing them, many researchers try to improve the

(a) Flip-OFDM transmitter

(b) Flip-OFDM receiver
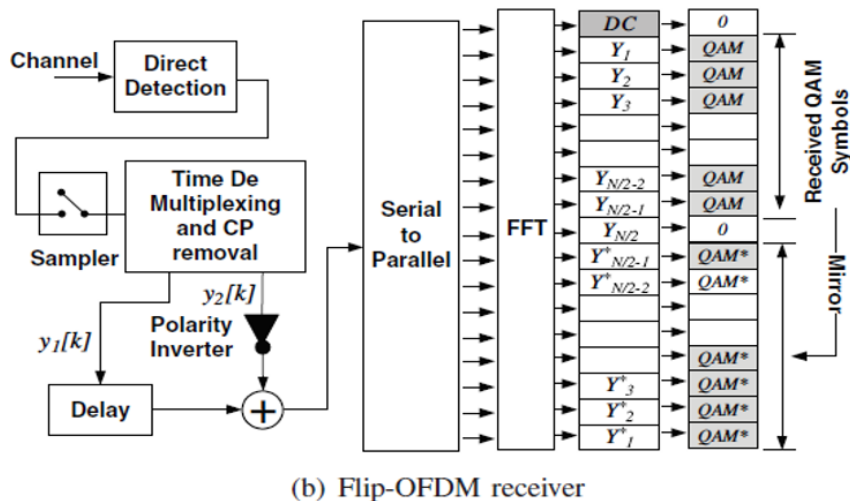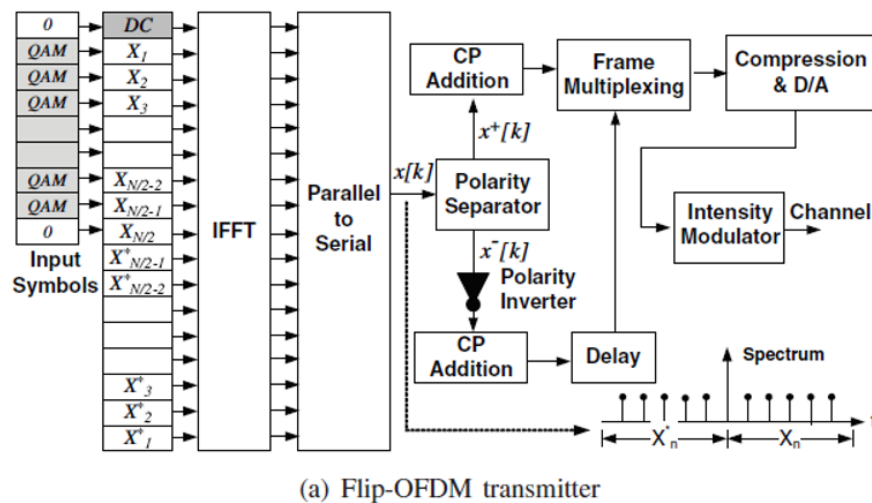
FIGURE 2.8: Flip Optical OFDM system block diagram [58] © 2012 IEEE.

spectral efficiency of these OFDM algorithms while still maintaining their power advantage as much as possible.

Dissanayake *et al.* proposed asymmetrically clipped DC biased optical OFDM (ADO-OFDM) by transmitting ACO-OFDM on the odd subcarriers and DCO-OFDM on the even subcarriers [59]. Two IFFTs were used to generate the ADO-OFDM signal, with one IFFT for ACO-OFDM and another one for DCO-OFDM. Then the two generated waveforms were added to generate ADO-OFDM waveform. As the DCO-OFDM on the even subcarriers required DC bias, so overall the ADO-OFDM system cannot avoid DC bias. The DC bias must be selected carefully to achieve a tradeoff between optical power efficiency and SNR. Although the clipping distortion generated by quantization of DCO-OFDM degraded its own signal quality, it had no influence on the odd subcarriers carrying data for

ACO-OFDM. Therefore, the ACO-OFDM could be demodulated firstly by using an FFT in the receiver. Then the recovered data were used to regenerate the clipping distortion of ACO-OFDM, to be removed from the received waveform. Now the DCO-OFDM signal was not influenced by the clipping distortion from ACO-OFDM anymore; thus, it could be decoded as normal DCO-OFDM. Finally, all the data could be recovered. As all the subcarriers were used to carry information, ADO-OFDM had the same spectral efficiency as standard DCO-OFDM. At the same time, the ACO-OFDM used in the odd subcarriers brought a certain level of power advantage over standard DCO-OFDM. The simulation results showed that ADO-OFDM required less optical power than DCO-OFDM depending on the fact that the power allocation to the ACO-OFDM and DCO-OFDM, the constellation size employed and DC bias used.
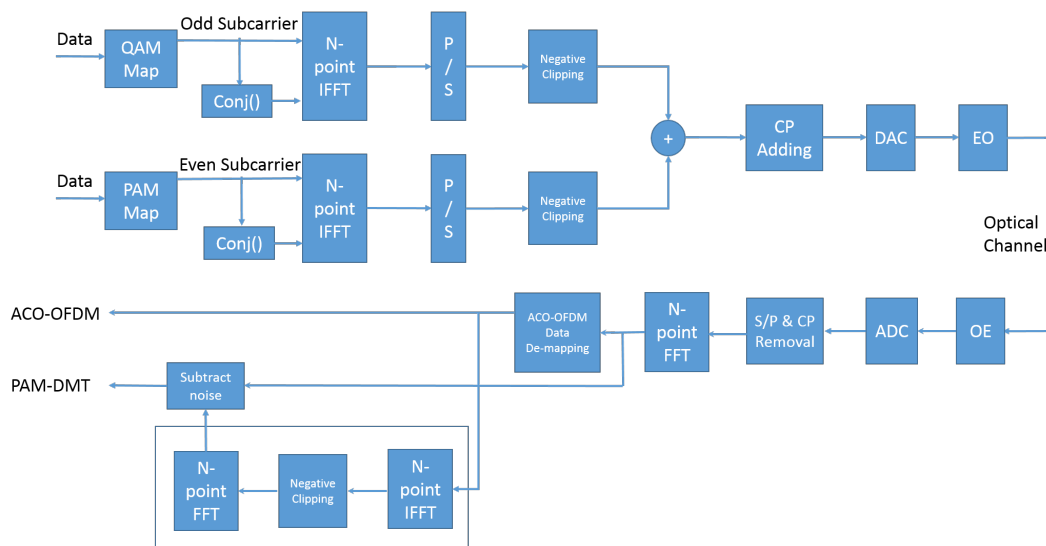
FIGURE 2.9: Block diagram of baseband HACO-OFDM systems [61].

Ranjha *et al.* proposed hybrid asymmetrically clipped OFDM (HACO-OFDM) by transmitting ACO-OFDM on the odd subcarriers and PAM-DMT on the even subcarriers simultaneously [61]. The block diagram of HACO-OFDM is shown in Fig. 2.9. It can be seen that in HACO-OFDM algorithm, ACO-OFDM and PAM-DMT were separately applied to odd and even subcarriers and then added together to modulate the intensity of optical carrier, so it maintained the power efficiency of ACO-OFDM and PAM-DMT without requirement of DC bias. Compared with ACO-OFDM, its even subcarriers were pulse-amplitude-modulated, leading to an increase of spectral efficiency. Similar to ADO-OFDM, in the receiver, the data on the odd subcarriers was recovered firstly because it was not influenced by clipping distortion from both ACO-OFDM and PAM-DMT. Then they were used to estimate the clipping distortion of ACO-OFDM, followed by

its removal from the received waveform before demodulating the data on the even subcarriers (PAM-DMT). It completely removed the DC bias with a moderate spectral efficiency increase in it. The simulation results showed that HACO-OFDM performed better than ACO-OFDM and ADO-OFDM.
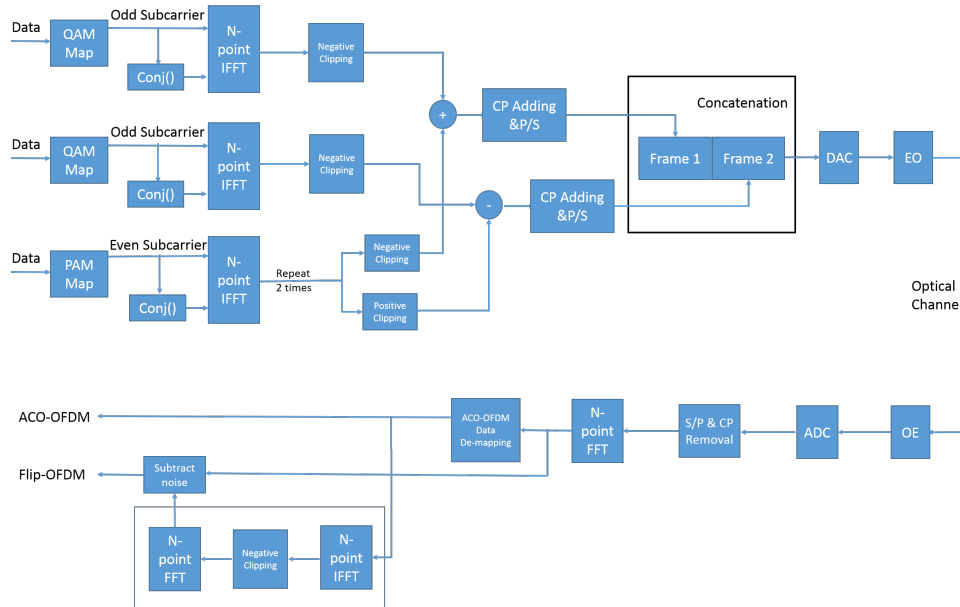
FIGURE 2.10:   Block   diagram   of   baseband   ASCO-OFDM   systems [60].

Instead of using PAM-DMT on the even subcarriers, Wu *et al.* proposed modulating flip-OFDM onto these unused even subcarriers to increase the spectral efficiency of ACO-OFDM [60]. This scheme was called asymmetrically and symmetrically clipping optical OFDM (ASCO-OFDM) and its block diagram is shown in Fig. 2.10. ASCO-OFDM did not need the DC bias because it was superimposed by ACO-OFDM and flip-OFDM. In the receiver, a decoding of ACO-OFDM and its noise estimation was still required before decoding the data on the even subcarriers. Eventually, it could increase the spectral efficiency of ACO-OFDM but could not reach to the spectral efficiency of DCO-OFDM, because flip-OFDM halved the spectral efficiency of even subcarriers.

Tsonev *et al.* proposed enhanced U-OFDM (eU-OFDM) to increase the spectral efficiency of U-OFDM [62], which was also known as Flip-OFDM. In this scheme, no DC-bias was required and its spectral efficiency could approach that of DCO-OFDM if the number of depths was enough. The modulated signal in each depth was an independent U-OFDM signal. By transmitting repeats of the U-OFDM symbol more times per frame in deeper depths, it allowed the recovery of data from lower depth to the higher depth in an iterative way. However, the generation procedure of eU-OFDM was quite complex. Besides, its equalization

in the receiver was difficult, because many signals in different depths shared the same frequencies.

Layered OFDM was developed recently [63]–[68], using more layers to carry data in the unused subcarriers in the first layer. The data carrying subcarriers must be carefully selected to ensure that the clipping distortion in the higher layers did not fall on the data-carrying subcarriers in the lower layers. According to its modulation format in the first layer, the layered OFDM algorithms were called Layered ACO-OFDM [65] and augmented-spectral-efficiency DMT (ASE-DMT) [68], which will be discussed in more detail in Chapters 4 and 5 separately.

2.5   Real-Time Optical Communication Experiments

When an algorithm is developed, it is usually firstly demonstrated by simulation, for example, using MATLAB or VPIphotonics simulations. This is very useful to verify the correctness of the algorithm and explore its advantage over other algorithms in a very timely manner. However, as the simulation depends on the system model, which always deviates from the real system somewhat, so experiments are required to perform afterwards. In an experimental demonstration, the DSP can be processed in offline using oscilloscope and MATLAB or real-time using Field-Programmable Gate Array (FPGA) and Application-Specific Integrated Circuit (ASIC). As real-time experimental demonstration can reflect the limitation from hardware resources, in this thesis, most of the research focus on real-time experimental demonstrations using FPGAs.

2.5.1   Real-Time Single-Carrier Optical systems

In the 2000s, high speed electronic digital signal processing gained great interests to combat the transmission impairments such as chromatic dispersion in long-haul optical systems. Offline digital signal processing using MATLAB is a popular choice to demonstrate DSP for the transmission experiments [134]–[139]. Although in these years, great improvements have been made in processors, there are still doubts that these DSP algorithms can be implemented in hardware due to the significant higher data throughput of optical system. Therefore, many real-time experiments have been performed, whose transmission performance are inspiring. The highest data rates achieved by research groups for single-carrier optical system are shown in Fig. 2.11.

In 2008, Watts *et al.* demonstrated an FPGA-based optical transmitter using real-time DSP for electronic predistortion to combat the CD [140]. Using offline
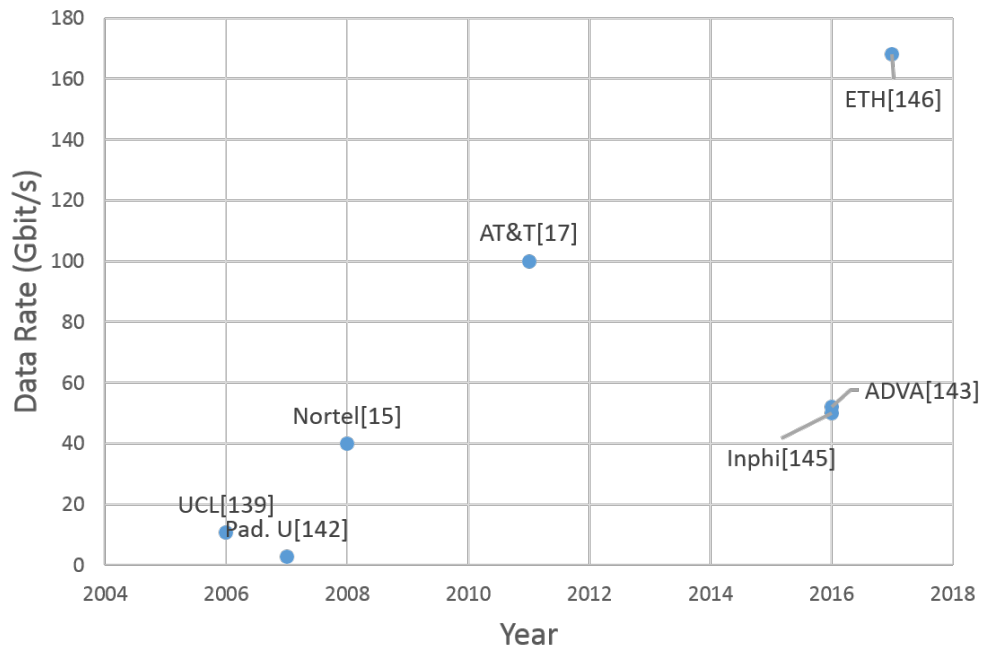
FIGURE 2.11: The highest data rates achieved by research groups
for single-carrier optical system.

signal processing in the receiver, a data rate of 10.7 Gb/s was achieved and the transmission distance was up to 1200 km. Waegemans *et al.* showed that it was possible to compensate both the CD and self-phase modulation (SPM) by using real-time DSP for electronic predistortion in an FPGA-based transmitter [141].

In 2006, Pfau *et al.* first demonstrated a real-time data recovery experiment for a QSPK modulated DFB laser [142]. The signal was successfully transmitted over 63 km of SSMF with a data rate of 800 Mb/s. Although real-time digital clock recovery was not available in this experiment, it showed great potential for a fully real-time coherent QPSK receiver. In 2007, Pfau *et al.* took his own research a step forward by demonstrating a coherent digital polarization diversity QPSK receiver at a data rate of 2.8 Gb/s using FPGA [143]. A real-time clock recovery was performed in this experiment. In 2008, Sun *et al.* demonstrated the transmission performance of a real-time 40 Gb/s DP-QPSK coherent transceiver over 900-km non dispersion-shifted fiber (NDSF) [15]. The coherent transceiver card is shown in Fig. 2.12. All the signal processing modules such as clock recovery, carrier recovery, polarization and PMD tracking, and dispersion compensation were all done digitally and implemented in an ASIC using 90-nm CMOS technology. This was a very important moment for the development of optical communication, meaning that these DSP algorithms are totally implementable and could become more and more powerful with the advances in digital technology. It is followed by a real-time 100 Gb/s DP-QPSK experimental demonstration in 2011 [17]. After

this field trial experiment, a commercial 100 Gb/s optical transmission system was deployed all over the world.
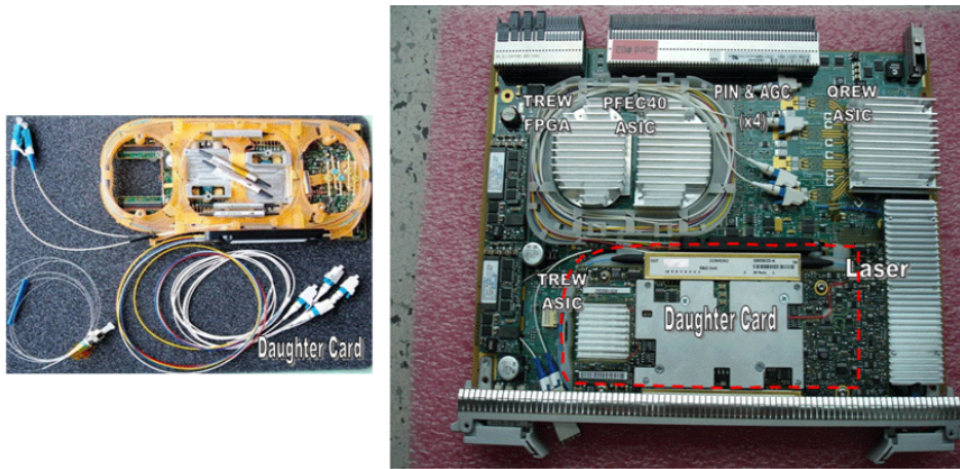
FIGURE 2.12: The 40G coherent transceiver card. Reprinted with permission from ref [15], [OSA].

At 100 Gb/s or above, for short-haul fiber-optic links, PAM4 is considered to be one of the most promising candidates. In 2016, Eiselt *et al.* demonstrated a real-time 26-Gbaud PAM4 transmission system in C band [144]. Its data rate was 52 Gb/s. When a dispersion equivalent to 10-km of SSMF was added on the transmission link, a 1-dB OSNR penalty was seen. By using eight channels, they further successfully demonstrated a real-time transmission of 400G PAM4 over 100-km SSMF in C band in 2016 [145]. It only required a simple receiver equalization and a low-complexity FEC with only 2.7% overhead, promising a low-cost and high-speed solution for inter-datacenter connection. In the meantime, Chang *et al.* also demonstrated a real-time 25-Gbaud PAM4 optical transmission system. By using two lanes, a data rate of 100 Gb/s was achieved over 40-km SSMF at a 1310-nm wavelength [146]. In 2017, Josten *et al.* proposed an efficient timing recovery in the frequency domain, which allowing for a record low non-integer receiver oversampling of 8/7 [147]. By using this technique, a real-time receiver for dual channel PAM signal detection with a data rate beyond 100 Gb/s was achieved.

2.5.2   Real-Time Optical OFDM Systems

After electronic precompensation and postcompensation are proposed to compensate for the optical dispersion in single carrier optical communication system, Lowery *et al.* showed by simulations that a combination of OFDM and optical single sideband (OSSB) can be used to compensate for fiber dispersion in

2006 [18]. Almost at the same time, a coherent OFDM solution was proposed by Shieh *et al.* [19]. Then huge range of OFDM experiments using offline DSP were performed with higher data rate and longer transmission distance [20], [148]–[150]. But doubts still exists whether OFDM transceiver can be implemented in the FPGA or ASIC, because both IFFT and FFT are very resource-hungry DSP. The highest data rates achieved by research groups for optical OFDM system are shown in Fig. 2.13.
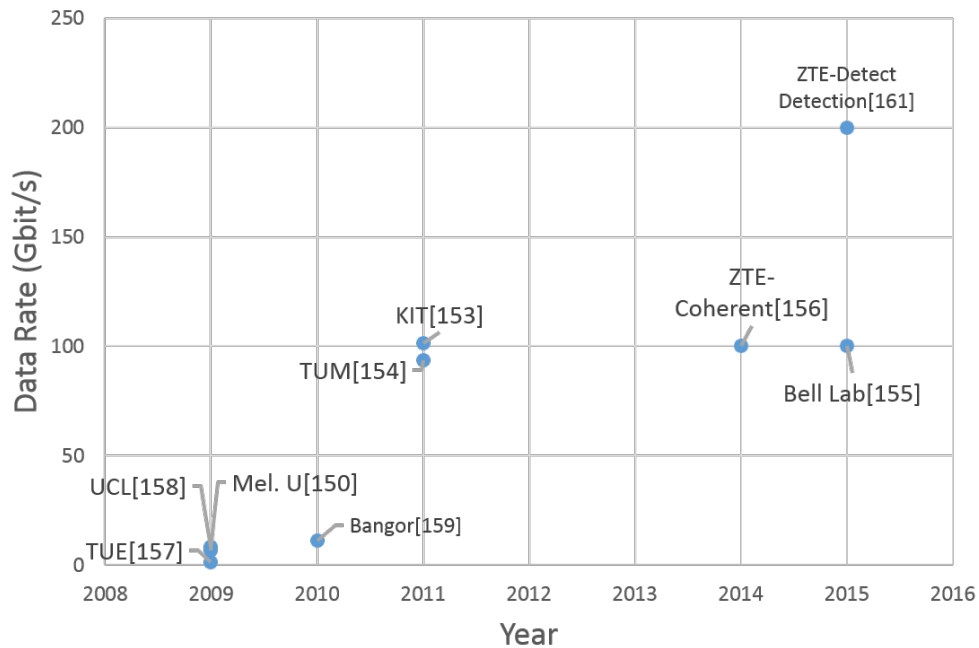
FIGURE 2.13: The highest data rates achieved by research groups
for optical OFDM system.

In 2009, the first real-time reception of multi-gigabit coherent optical OFDM was shown by Yang *et al.* using a FPGA [151]. Then, by using dual-polarization, another coherent optical OFDM receiver was demonstrated by Chen *et al.* [152]. Successful back-to-back transmission was achieved with a data rate of 6.67 Gb/s by using 16-QAM. Just several months later, the reported real-time data rate of coherent optical OFDM receiver was increased to 53.3 Gb/s by using three sub-bands [153]. In 2011, Schmogrow *et al.* reported a real-time coherent OFDM transmitter beyond 100 Gbit/s [154]. Then Inan *et al.* demonstrated a real-time polarization-multiplexed OFDM transmitter with a slightly lower data rate of 93.8 Gb/s but a higher IFFT size of 1024 [155]. In 2015, the first real-time 100 Gb/s coherent optical OFDM receiver was demonstrated with successful transmission over 495.2-km mixed types of field-installed fiber [156]. However, all the above real-time demonstrations are only in transmitter or receiver. A real-time 100-Gb/s coherent OFDM transceiver was not available until OFC 2014, when

Xiao *et al.* reported the first single-band DP-16-QAM coherent OFDM transmission and reception over 200-km SSMF [157].

For direct detection OFDM, the first real-time gigabit transmitter was shown by Lee *et al.* with a data rate of 1.25 Gbit/s in 2009 [158]. Then Benlachtar *et al.* reported a real-time SSB-OFDM with a data rate of 8.36 Gb/s in 2009 [159]. Its experiment setup is shown in Fig. 2.14. The DAC was constructed from discrete components such as splitters and attenuators and had a resolution of 4 bits. Sixteen high-speed transmitters of the FPGA were used to convert lower speed parallel data to high speed serial data to drive the DAC. The transmission distance was up to 200 km, because the fiber dispersion could be compensated in a SSB OFDM direct detection transmission system.
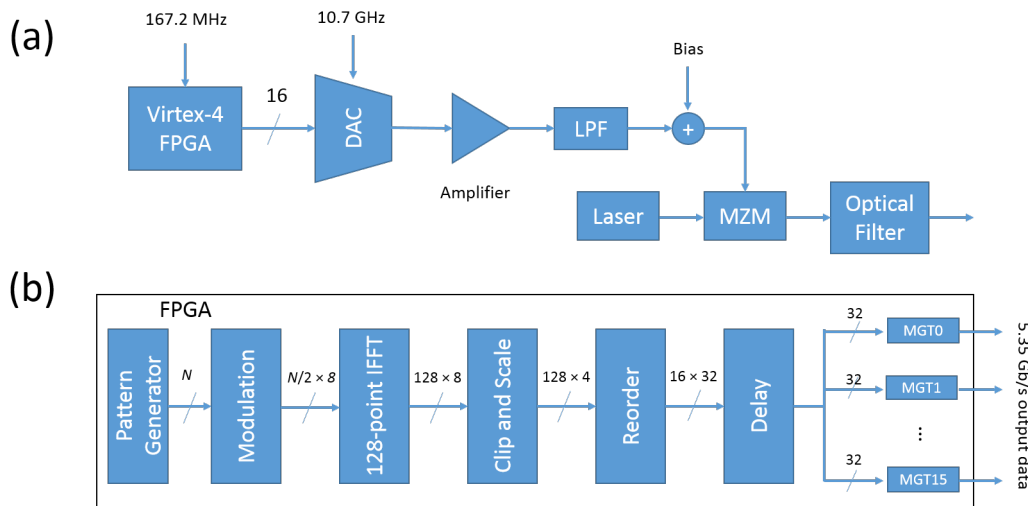
FIGURE 2.14: Block diagram of real-time transmitter design (a) transmitter setup (b) DSP implemented in the FPGA [159].

Almost at the same time, a real-time OFDM transceiver in IMDD communication system was reported by Jin *et al.*, as shown in Fig. 2.15 [160]. A directly modulated laser was used in this experiment. As no OSSB was used in the transmission, its transmission distance was limited to 75 km due to the fiber dispersion and laser chirp. By using bit- and power-loading and higher spectral efficiency modulation format, the data rate was finally increased to 11.25 Gb/s in 2010 with almost the same experiment setup [161].

Li *et al.* firstly upgraded the data rate of a real-time single-lane optical OFDM transceiver to 50 Gb/s in IMDD based short-haul fiber-optic link [162]. The block diagrams of this system is shown in Fig. 2.16. The signal was successfully transmitted over 20-km SSMF. By using more carriers, the total data rate was easily increased to 100 Gb/s for two carriers [163] and 200 Gb/s for quad-carriers [164].
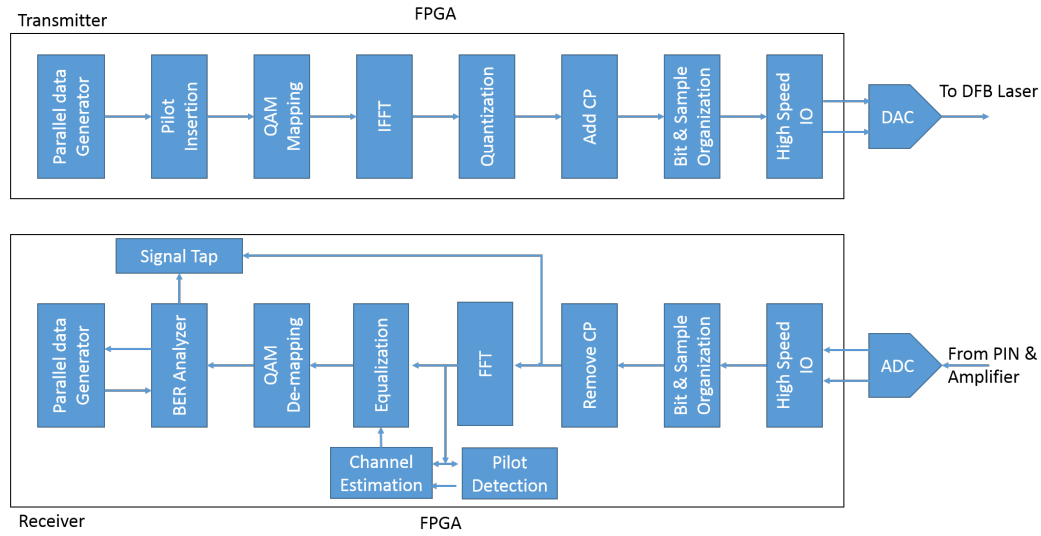
FIGURE 2.15: Real-time OOFDM transceiver architecture [160].
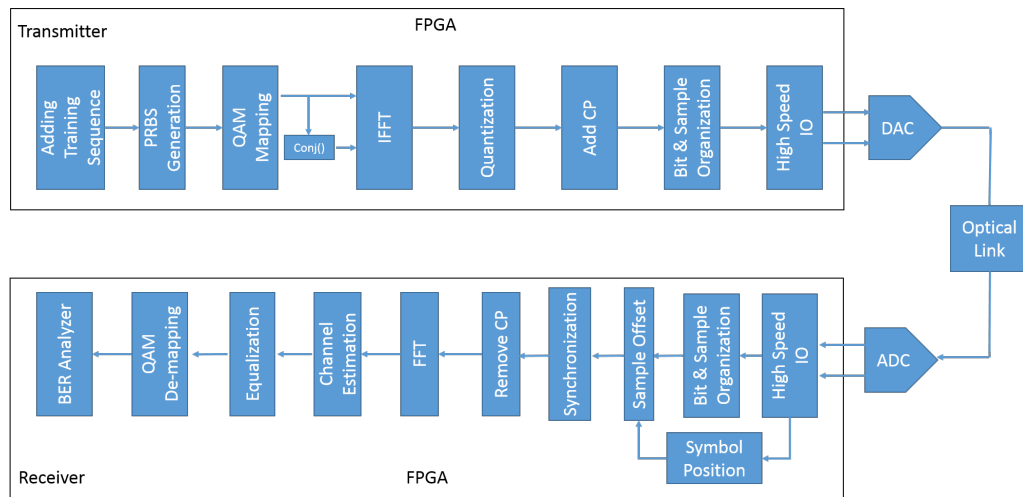
FIGURE 2.16: Real-time OOFDM transceiver architecture [162].

2.5.3 Key Devices for Real-Time Signal Generation

2.5.3.1 FPGA or ASIC

The discussion of ASIC versus FPGA can be very complex because both of them have their own advantages and disadvantages. Generally, an ASIC designer is limited by the manufacturing process from the foundry such as feature size, switching time and so on. An FPGA designer is limited by the available FP-GAs. They have to balance the cost and performance when selecting one FPGA chip due to the fact that a FPGA chip does not aim at one specific application. With the same feature size, ASIC can achieve higher performance, at a less power consumption and higher output signal speed, because an ASIC designer can optimize the design at the physical level to fully exploit the available resources.

However, the major issues for an ASIC chip are the exorbitant initial cost due to the masks, more consumed time and fixed functionality. Being cheap and reprogrammable, FPGA chips are the most suitable choice for our project.

FPGA are configurable digital circuits [165]. By using corresponding software, they can be programmed to achieve many kinds of DSP functions according to the need from the customer. The programming language can be Verilog and VHDL. An FPGA chip consists of a large number of small logic circuit elements, which can be connected together by using programmable switches in the FPGA chip to support the implementation of complex digital logic circuits such as DSP. The hardware resources in the FPGA can be highly parallel processed to generate a significant large throughput. Combined with powerful Serializers/Deserializers (SerDes) integrated in the FPGA chip, a high serial data rate can be easily generated to drive the DAC. Besides, the latest FPGA provides dedicated DSP slices to perform arithmetic operation in a fast and energy-efficient way [166]. Xilinx and Altera companies are the top two FPGA product providers. In this thesis, all real-time experiments are demonstrated using Virtex-6 FPGA from Xilinx.

Fig. 2.17 shows the standard FPGA design flow. Firstly, the designer writes a description of the digital circuits for certain DSP, usually in the form of a hardware description language such as Verilog HDL or VHDL. The synthesis process will check the code's syntax and analyse the hierarchy of the design, which ensures that it is optimized for the design architecture. After synthesis, a functional simulation is required to perform to see the behavior of the circuit in terms of input signals. Then place and route can translate the design into the real circuit in the FPGA. In the placement phase, it will choose a location on the target device for each logic block. The routing phase connects the blocks together by using the rooting matrixes that exit in the chip. Although the connection wire between different logic units are very short, in high-speed digital design, the transmission time can become large, compare with the cycle of the clock. Therefore, static timing analysis is performed to extract the circuit parameters and estimate the overall transmission delay between different logic units to make sure that all the timing constraints are met correctly. Finally, the digital circuits are downloaded into the FPGA chip, where debug is carried out until all the expected functions are achieved.

2.5.3.2   DAC

The DAC used in all the experiments is VEGA DAC II from MICRAM. This DAC has a resolution of 6 bits with a sampling rate of > 25 GSample/s. As a multiplexer is integrated into the DAC, four serial lines are multiplexed to generate
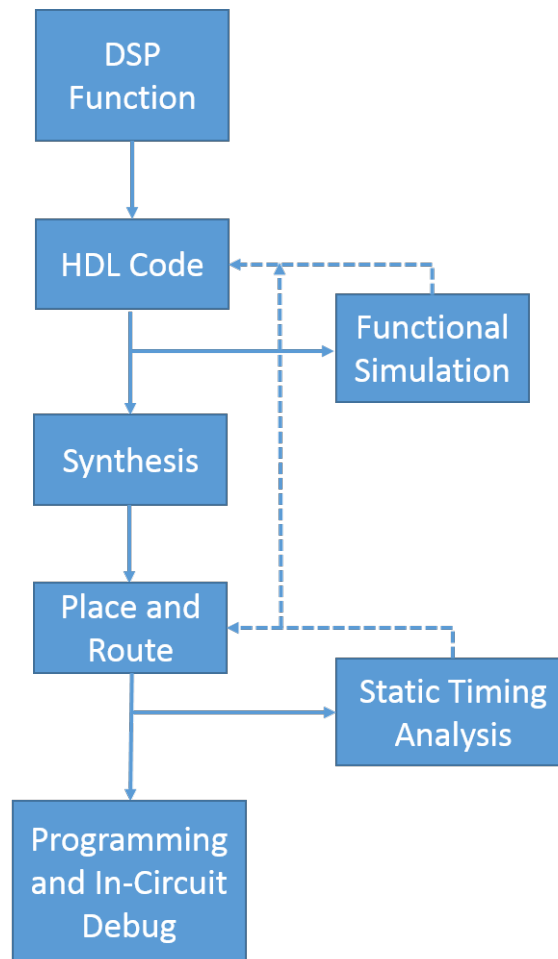
FIGURE 2.17: FPGA design flow.

1-bit drive input for DAC. Therefore, 24 data transmission serial lines are required between the FPGA and DAC. In the experiments, only 5-bit resolution are available due to the limited number of high-speed transceivers (20) in the FPGA. The interface between FPGA and DAC is shown in Fig. 2.18. The sampling rate of DAC is twice as the DAC clock frequency. FPGA can access the register in the DAC via the register bus. By changing the parameter of the register, the input clock frequency of the FPGA can be changed, which is provided by the DAC. Besides, these registers are also used to achieve the synchronization between the FPGA and DAC because synchronization status must be read from them. The data into the DAC first pass a SerDes input buffer, which enables individual sampling clock alignment and synchronization by comparing a training sequence to the built-in pseudorandom binary sequence (PRBS) or to the adjacent channel.
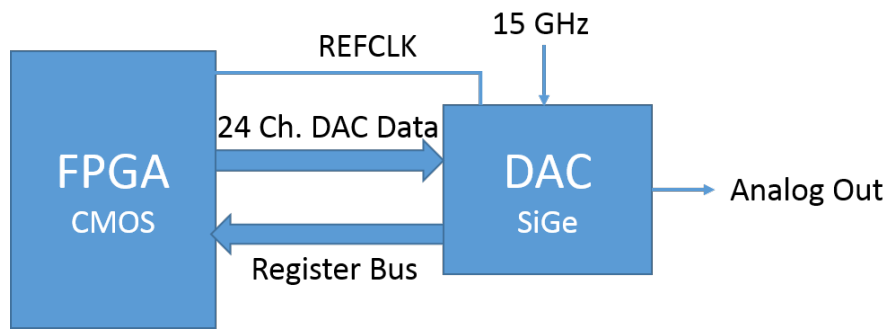
FIGURE 2.18: Interfacing between FPGA and MICRAM DAC [167].

2.6 Conclusion

In this chapter, the development of DSP algorithms in short-haul optic-fiber links is reviewed. In short distance optical communication, intensity modulation, combined with direct-detection is still preferred. Among all modulation formats, CAP, OFDM (DMT) and PAM4 are the most promising candidates. Then the power-efficient optical OFDM algorithms are introduced, followed by many real-time experimental demonstrations in both single-carrier and OFDM optical communication systems. The real-time power-efficient optical OFDM system is a very interesting research topic, which has not been addressed before.

Chapter 3

Efficient ACO-OFDM Signal Generation

3.1 Introduction

Optical OFDM, combined with intensity modulation and direct detection (IMDD) has emerged as a promising candidate for next-generation short-haul (>10km) optic-fiber links, due to its ability to reduce the influence of fiber dispersion by using only simple one-tap equalizers in the receiver and achieving high spectral efficiency by carrying higher-order modulation formats on its subcarriers [79], [168]. Although many real-time short-haul OFDM experiments have been presented that use off-the-shelf devices [158]–[160], [162], [164], proving its practicality in short-haul fiber-optic links, most of these experiments have focused on the analysis of the optical signal quality after transmission over fiber. In the real-time demonstration, as the IFFT/FFT consumes a majority of the logic resource in the OFDM transceiver, efficient implementation of IFFT/FFT has to be optimized to reduce its overall computational complexity.

Commonly, Hermitian symmetrical inputs for the positive and negative frequencies of the IFFT are usually adopted in the OFDM transmitter to achieve a real-valued output waveform [169]. This will double the required IFFT size for a given number of subcarriers because only half of the IFFT inputs are independent. Although it is well known that its complexity can be reduced by using a complex-valued OFDM, which requires a separate low-RF subcarrier [170]. In 2013, Barrami *et al.* developed another method of OFDM transmission, where the inphase and quadrature components are transmitted in successive blocks [171], followed by many experimental demonstrations using offline digital signal processing (DSP) [172]–[175]. This method is non-Hermitian-symmetrical (NHS) IFFT/FFT. They showed that the same transmission performance, such as peak-to-average power ratio (PAPR) and bit-error-ratio (BER), is achieved, as the Hermitian symmetrical (HS) IFFT/FFT. However, a practical implementation of an

OFDM transmitter based on NHS-IFFT has yet to be demonstrated, to identify its transmission performance in the optical transmission link and how the logic resource requirements can be reduced.

Besides, all the previous real-time OFDM experimental demonstrations in IMDD based optical communication system were DC-biased optical OFDM (DCO-OFDM) [158]–[160], [162], [164], where a significant DC bias was required to prevent negative-valued samples being clipped. As a solution to the bias issue, asymmetrically clipped optical OFDM (ACO-OFDM) generates unipolar OFDM signals to give a higher optical power efficiency compared with DCO-OFDM, by clipping all negative peaks at the mean level, and only loading one-half of the subcarriers [55].

In this chapter, the NHS-IFFT/FFT implementation method will be a briefly introduced firstly. Then I will show the efficient implementation method for an ACO-OFDM transmitter using NHS-IFFT/FFT implementation. All the DSP in the ACO-OFDM transmitter is implemented in a Virtex-6 (XC6VLX240T) FPGA. The results show that our implementation can reduce the resource utilization by two thirds for ACO-OFDM. Please note that the benchmark of computational complexity is HS-IFFT/FFT. Finally, its Q-factors for optical back-to-back and 15-km standard single-mode fiber (SSMF) transmission are evaluated using offline DSP in the receiver and compared with HS-IFFT/FFT ACO-OFDM transmitter.

3.2 NHS-IFFT/FFT Implementation

The FFT and IFFT are the key components in the OFDM communication system. In a HS IFFT/FFT based optical OFDM system, Hermitian symmetry is imposed on the OFDM subcarriers to force the quadrature components of IFFT outputs to be zero-valued and only the inphase components of IFFT outputs are used to drive the laser or LED. However, only half of the OFDM subcarriers are independent leading to a doubled size of FFT/IFFT. That is to say, to generate the OFDM signal with N subcarriers, $2N$-point FFT/IFFT is required in the transceiver. Besides, as the computational complexity of FFT/IFFT is increased in according to $N/2 \log_2 N$, a large FFT/IFFT size also requires higher bit precision, so the doubled size of FFT/IFFT will occupy larger chip area and consume more power [176].

Fig. 3.1 shows the widely used block diagram of optical OFDM in IMDD communication system using HS IFFT/FFT. In the transmitter, The data is mapped to form the N-complex QAM signals. Along with their complex conjugates, $2N$ complex QAM symbols, ($X(2N - k) = X^*(k), k = 1, 2, ..., 2N - 1$) with ($X(0) =

$X(N) = 0$), are imposed on the frequency inputs of a $2N$-point IFFT. The time domain OFDM signals ($x(n) = x_r(n) + x_i(n)$) over one symbol is expressed as Equation 3.1. The quadrature components ($x_i(n)$) of the IFFT outputs are zero-valued, so only the inphase components ($x_r(n)$) of the IFFT outputs form the time-domain signal $x(n)$ ($2N$-point) in one OFDM symbol. After parallel-to-serial (P/S) conversion and cyclic prefix (CP) adding, a digital to analog converter (DAC) is used to generate the continuous driving signal to modulate the intensity (power) of the laser or LED. In the receiver, a photodetector converts the optical signal to electrical signal, followed by an analog to digital converter (ADC) to generate discrete time domain OFDM signals, which will be processed in the digital domain afterwards. After the serial-to-parallel (S/P) conversion and CP removal, a $2N$-point FFT is used to transform the OFDM signals into the frequency domain and then decoded.
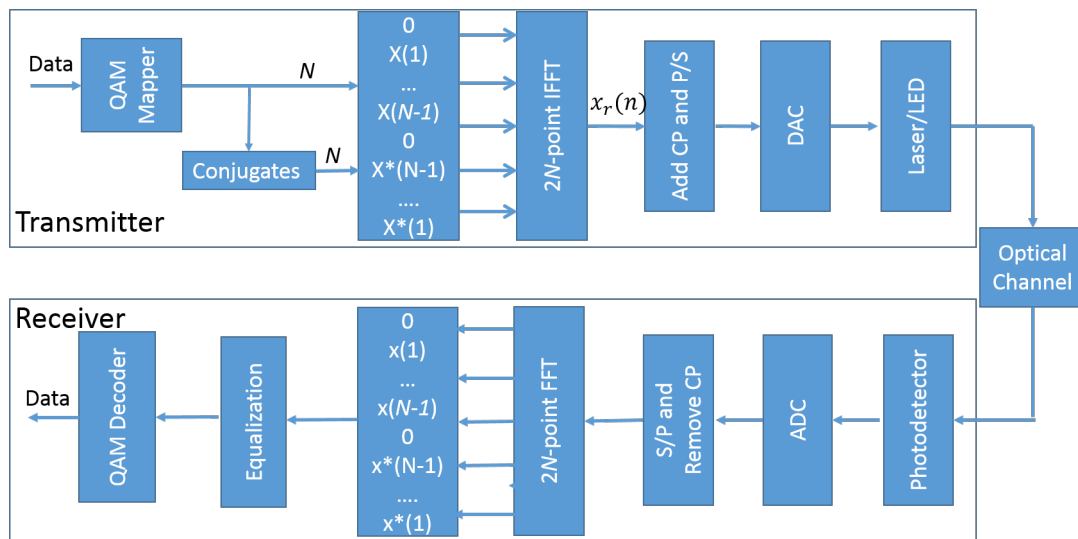
FIGURE 3.1: Optical OFDM in IMDD optical transmission link using HS IFFT / FFT.

$$x(n) = \frac{1}{2N} \sum_{k=0}^{2N-1} X(k) \exp(\frac{-j2\pi kn}{2N})$$
$$= x_r(n) + x_i(n)$$
(3.1)

Next, the optical OFDM transmission system using NHS IFFT / FFT will be introduced. Fig. 3.2 shows the block diagram of optical OFDM in IMDD communication system using NHS IFFT/FFT. Compared with HS IFFT/FFT, NHS IFFT/FFT does not use the Hermitian symmetrical inputs. Therefore, the IFFT

output signal is complex ($x_i(n)$ is not zero-valued in this case). In order to generate a $2N$-point OFDM signals, the N-point inphase ($x_r(n)$) and quadrature components ($x_i(n)$) can be concatenated in the time domain, as shown in the Equation 3.2. At the receiver, the $2N$-point signal are separated to generate the N-point complex inputs of FFT, as shown in Equation 3.3. The resulting complex signal can be demodulated as in conventional complex OFDM signal. As only N-point IFFT/FFT is required to generate the $2N$-point outputs, while $2N$-point IFFT/FFT is required in the HS IFFT/FFT, so its computational complexity can be reduced significantly. The other blocks are the same as the optical OFDM system using NHS IFFT/FFT.
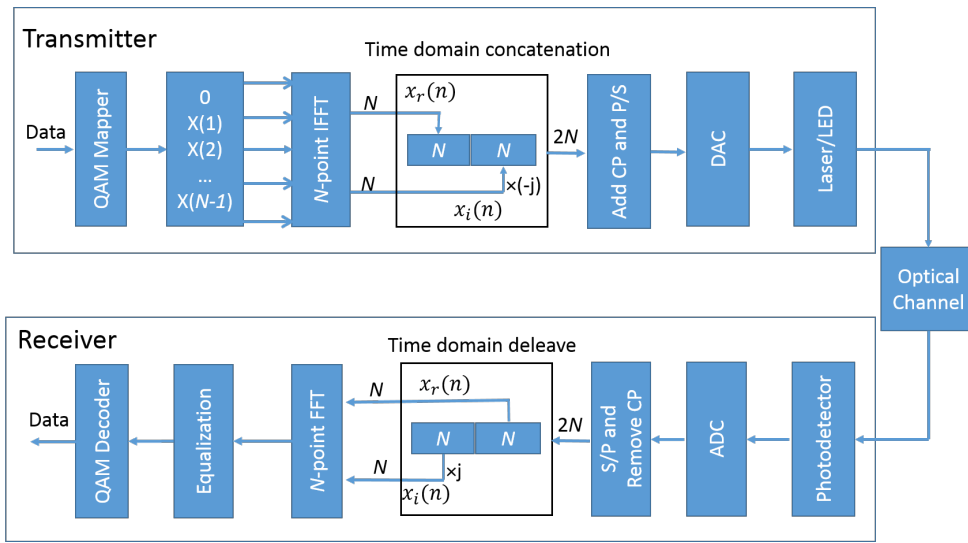
FIGURE 3.2: Optical OFDM in IMDD optical transmission link using NHS IFFT / FFT.

$$x(n) = \begin{cases} x_r(n) & n = 0, ..., N-1 \\ x_i(n-N) & n = N, ..., 2N-1 \end{cases} \tag{3.2}$$

$$\begin{cases} x_r(n) = x(n) & n = 0, ..., N-1 \\ x_i(n-N) = x(n) & n = N, ..., 2N-1 \end{cases} \tag{3.3}$$

3.3 Real-Time ACO-OFDM Transmitter

3.3.1 ACO-OFDM Algorithm

In Chapter 2, a brief introduction of odd-subcarrier ACO-OFDM algorithms has been made. In this section, a more detailed analysis of odd-subcarrier ACO-OFDM algorithms, which were developed by Armstrong and Lowery [54], [55],
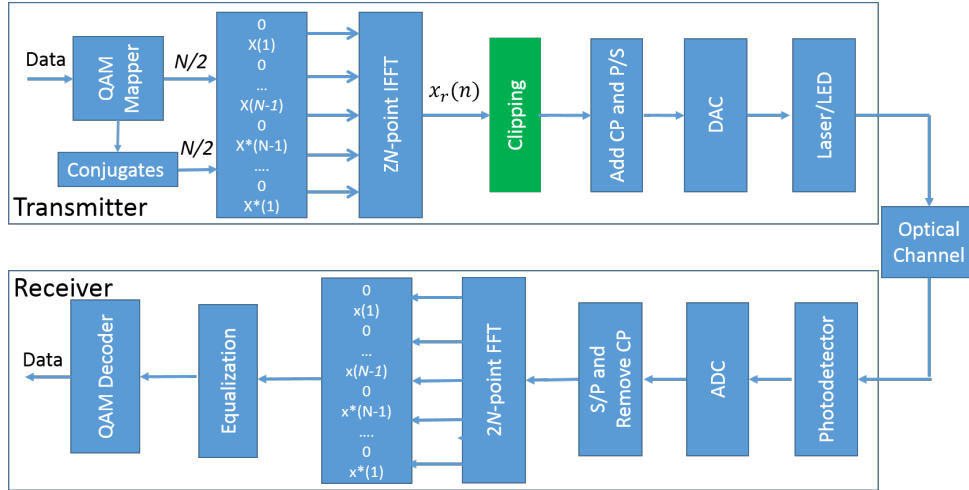
FIGURE 3.3: ACO-OFDM transceiver block diagram using HS IFFT/FFT. The clipping procedure for ACO-OFDM is blue highlighted.

will be introduced. By simply setting all the negative values to be zero, ACO-OFDM can improve the power efficiency of DCO-OFDM for a given data rate. In this chapter, hereafter, ACO-OFDM means odd-subcarrier ACO-OFDM by default.

In this section, a typical ACO-OFDM transmission system using HS IFFT/FFT, as shown in Fig. 3.3, is used to illustrate why the ACO-OFDM signal can avoid the use of DC bias. The ACO-OFDM transmission system using NHS IFFT/FFT works in a similar way, using only the odd subcarriers to carry information, but its inphase and quadrature components need to be separately clipped to be non-zero-valued before concatenation.

In Fig. 3.3, the binary data is mapped to form the complex QAM signals, which are then imposed on the OFDM subcarriers using a $2N$-point IFFT module. As the same as DCO-OFDM using HS IFFT/FFT, only half (N-point) of the QAM signals on the OFDM subcarriers are independent while the remaining half are occupied by their conjugate signals to force the quadrature components of IFFT to have zero-valued outputs. Compared with DCO-OFDM, the main algorithm alteration for ACO-OFDM is that only the odd subcarriers are used to carry QAM data. Here, we use $X(k), k = 0, 1, ..., 2N - 1$, representing the frequency domain OFDM input signals. Therefore, the ACO-OFDM subcarriers are written as $X = [0, X(1), 0, X(3), ..., X(N-1), 0, X^*(N-1), ..., X^*(1)]$. The time-domain signal $x(n)$ is obtained after the IFFT, which is shown in Equation 3.4

$$x(n) = \frac{1}{2N} \sum_{k=0}^{2N-1} X(k) \exp(\frac{-j2\pi kn}{2N}), n = 0, 1, ..., 2N - 1 \qquad (3.4)$$

As the even subcarriers are zero-valued, Equation 3.4 can be simplified to

$$x(n) = \frac{1}{2N} \sum_{k=0}^{N-1} X(2k+1) \exp(\frac{-j2\pi(2k+1)n}{2N}), \tag{3.5}$$

Furthermore,

$$\begin{aligned} x(n+N) &= \frac{1}{2N} \sum_{k=0}^{N-1} X(2k+1) \exp(\frac{-j2\pi(2k+1)(n+N)}{2N}) \\ &= x(n) \exp(-j\pi(2k+1)) \\ &= -x(n), \end{aligned} \tag{3.6}$$

where n, k = 0, 1, ..., N-1. Therefore, $x(n)$ is antisymmetric in time domain as shown in Fig. 3.4(a), so we can clip all the negative signals to be zero-valued without loss of data, as shown in Fig. 3.4(b), because these data information is preserved in the positive signals. It can be seen more clearly in the frequency domain, as all the clipping distortion falls only on the even subcarriers, as shown in Fig. 3.4(c). It should be mentioned here that a majority of clipping distortion falls on the DC and even subcarriers. This clipping distortion on the DC will reduce the power efficiency of ACO-OFDM, which should be also considered in the calculation of the optical energy per bit. The clipping distortion on the even subcarriers comes from the intermodulation distortion generated by the clipping procedure. There is also some clipping distortion falling outside the OFDM signal band, as shown in 3.4(c), which can be removed by the filter in electrical or optical domain. All the data on the odd subcarries can be decoded as normal OFDM signals because they are not polluted by clipping distortion. Afterwards, cyclic prefix (CP) is added at the beginning of each OFDM symbol to eliminate the intersymbol interference (ISI) and intercarrier interference (ICI) if the CP is longer than the time-spreading of the channel. The clipping module is usually located before the CP-adding block. Afterwards, the signal is parallel-to-serial (P/S) converted to form the serial stream of OFDM symbols. Through the digital to analog converter, the anolog signals are used to drive laser or LED, then to be transmitted along the optical channel, which can be fiber for optic-fiber communication system or free space for optical wireless communication system. In the procedure of electrical to optical (EO) signal conversion, the signal voltage is mapped on the optical intensity directly. In the receiver, a photodiode (PD) converts the optical intensity to photocurrent to achieve optical to electrical (OE) signal conversion. A transimpedance amplifier (TIA) will convert the current into voltage

followed by an analog-to-digital converter (ADC). All the data recovery procedures are performed in the electrical domain using DSP. After serial-to-parallel (S/P) conversion and CP removal, an FFT transforms time domain OFDM signal into frequency domain. Then the channel response is estimated using training symbols. By using a simple one-tap equalizer, the channel can be equalized. Finally, the data carried on the odd subcarriers, which is free of clipping distortion, is sent to the QAM decoder to recover the data. The even subcarriers are always discarded in this thesis, although they contain useful information, which can assist the decoding of the data in odd subcarriers [177]–[179].
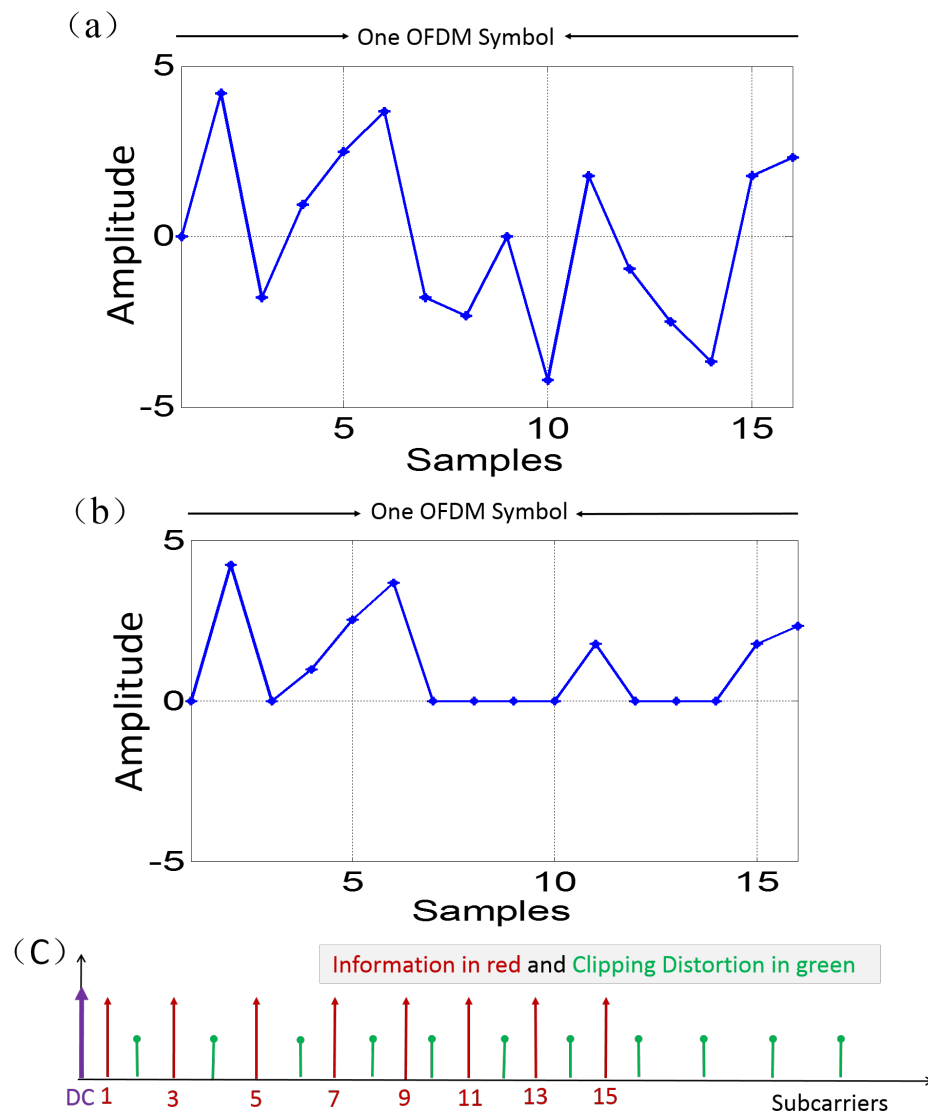
FIGURE 3.4: ACO-OFDM signals with 16 subcarriers (a) Time domain: half-wave symmetry (b) Time domain clipping process (c) Frequency domain: clipping distortion only falls on the even subcarriers; some falls outside the bandwidth of signal.

3.3.2   Implementation Cost for HS and NHS IFFT/FFT

The Spiral FFT/IFFT IP core [180], developed by Milder *et al.*, was used to generate one 128-point IFFT and one 64-point IFFT, both of which will be used in the following real-time demonstrations of ACO-OFDM transmitter. All the even subcarriers in the ACO-OFDM transmitter are not used to carry data. In the perspective of implementation, half of the IFFT's inputs are always zero, so an optimization method can be conducted to simplify the IFFT's implementation for ACO-OFDM transmitter. An 8-point 2-radix decimation-in-time (DIT) IFFT butterfly chart is shown in Fig. 3.5 to illustrate this optimization method for NHS IFFT/FFT. It should be mentioned here that this optimization method is also suitable for the HS IFFT/FFT. All of the results in the top half (grayed) corresponding to even-frequency subcarriers are always zero-valued for both inphase and quadrature components. Therefore, only the numbers in the bottom-half are required to be calculated. The output signals $x(0\text{-}3)$ in the top-half can be obtained directly from $x(4\text{-}7)$ because they just differ in sign. For NHS IFFT/FFT, the outputs $x(0\text{-}7)$ are all complex values, whose inphase and quadrature components will be concatenated in the time domain.
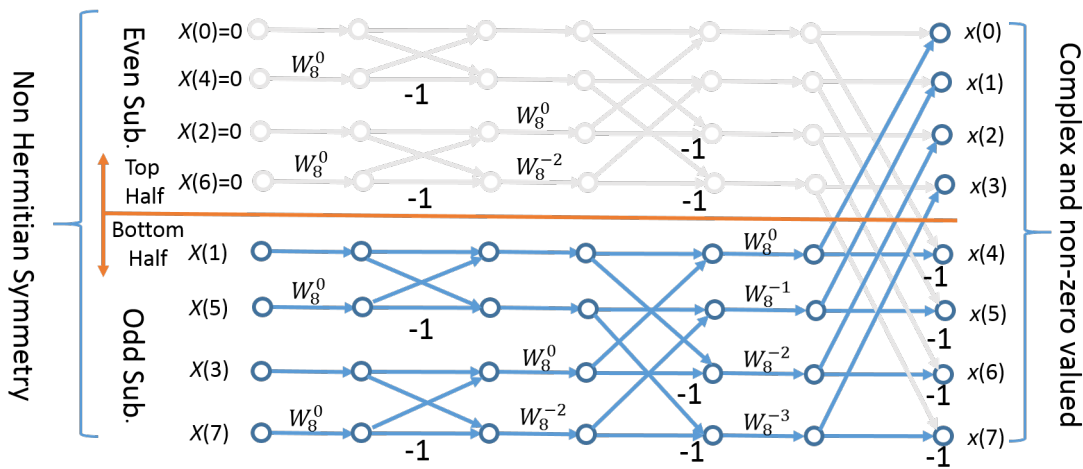
FIGURE 3.5: An 8-point radix-2 DIT NHS IFFT butterfly chart. All the zero-valued points are grayed-out.

In order to see the implementation cost for different methods, we optimized the 128-point IFFT and 64-point IFFT and implemented them in a Virtex-6 FPGA (XC6VLX240T) separately. The DSP48E1s resource (each DSP48E1s contains one multiplier) are used for multiplier's implementation for different methods, whose number are shown in Table 3.1, which can be used as an estimation of overall resource utilization because multipliers dominate the hardware implementation cost. By reducing the IFFT size to be a half, the NHS IFFT technique only needs

332 multipliers, saving approximately 52.6% of the FPGA's logic resources, compared with 700 multipliers used by the HS IFFT implementation. By eliminating the computational complexity in the top-half of IFFT butterfly, another 108 multipliers are not required. Therefore, overall, 68% of the logic resources can be saved by using the optimized HS IFFT, which is a significant amount reduction of computational complexity.

TABLE 3.1: Multiplier utilization in different sized IFFT.

IFFT Size	Number of Multipliers
64	332
128	700
optimized 64	224

3.3.3   DSP Implementation in the Transmitter

In this section, real-time ACO-OFDM transmitter using HS and NHS IFFT/FFT techniques were carried out to see their performance in the optical transmission link. The 128-point IFFT was used in the HS IFFT/FFT based ACO-OFDM transmitter, while the 64-point IFFT was used in the NHS IFFT/FFT based ACO-OFDM transmitter. Their DSP functions were implemented in a Virtex-6 FPGA, as shown in Fig. 3.6 and Fig. 3.7, which is called Scheme 1 and Scheme 2 in this section.
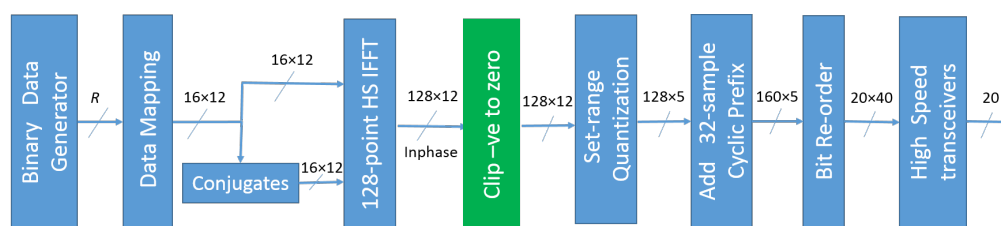
FIGURE 3.6: DSP functions implemented in the FPGA using HS IFFT.

The test data was stored in the FPGA and R binary data were mapped to 16 complex symbols in each clock. R is 32 for QPSK modulation format. The same modulation format was imposed on OFDM subcarriers for both schemes. After the data mapping, another 16 conjugate symbols were generated in Scheme 1 and distributed to a 128-point IFFT with a resolution of 12 bits. Only the real parts of its outputs, in total, 128 12-bit words, were processed in the set-range quantization module. In Scheme 2, these 16 complex symbols were distributed to the
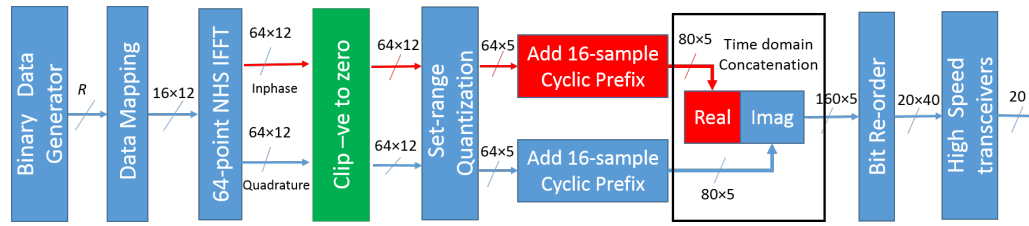
FIGURE 3.7: DSP functions implemented in the FPGA using optimized NHS IFFT.

inputs of 64-point IFFT without the requirement of their conjugate symbols. The first 8 data are allocated on the odd subcarriers (1, 3, ... , 15) and the second 8 data are allocated to the odd subcarriers (49, 51, ..., 63). Both of the two schemes used $2 \times$ oversampling rate. Then, 64-point complex outputs were generated from the IFFT and then sorted into their inphase and quadrature components to be quantized separately to meet the DAC 5-bit resolution requirement. Although both schemes generated 160 5-bit words to be rearranged and parallel-to-serial converted through the SerDes in the FPGA, their generation methods were different. Scheme 1 was quite straightforward: a 32-sample's CP were added in front of each OFDM symbol. Scheme 2 used a 64-point IFFT of which the inphase (64 12-bit words) and quadrature components (64 12-bit words) were processed individually and then concatenated in the time domain after appending a 16-sample CP individually. Both the IFFT modules had a resolution of 12 bits, which is a compromise between computational accuracy and hardware resource occupation. Totally, 20 FPGA's low-voltage differential signalling (LVDS) channels were used. All the data was sent to the DAC to generate analog OFDM output signals.

3.3.4   Experimental Setup

In this section, the real-time ACO-OFDM experiments were carried out to see their performance in the transmission system. The experimental setup of both ACO-OFDM transmitters are the same and shown in Fig. 3.8. A 156.25-MHz clock generated by the DAC provided a clock to the FPGA, which was not only used to control all the DSP modules in the FPGA but also synchronize the FPGA and DAC. The synchronization method used in this experiment was generally introduced, as shown in Fig. 3.9. More details can be found in the Appendix A. It is very important to achieve successful synchronization between FPGA and DAC for a proper real-time experiment [181], [182]. All the synchronization procedures were under control by an integrated microprocessor in a system-on-chip

approach. The DAC could generate pseudorandom bit sequences (PRBS) by itself, which served as synchronization patterns. Individually adjustable bit delay blocks were implemented in the 20 LVDS outputs of the FPGA, following by asynchronous first-in-first-out (FIFO) buffers, which were used to guarantee data consistency among all the 20 high-speed channels of the FPGA. All the 20 high-speed transmitters in the FPGA were programmed to be 6.25 Gbaud, which were then 4-to-1 multiplexed in a MICRAM DAC. The DAC has a sample rate of 25 GS/s when clocked at 12.5 GHz. As 16 subcarriers were used to carry QPSK data, the overall net data rate is 5 Gb/s for both the implementation schemes.
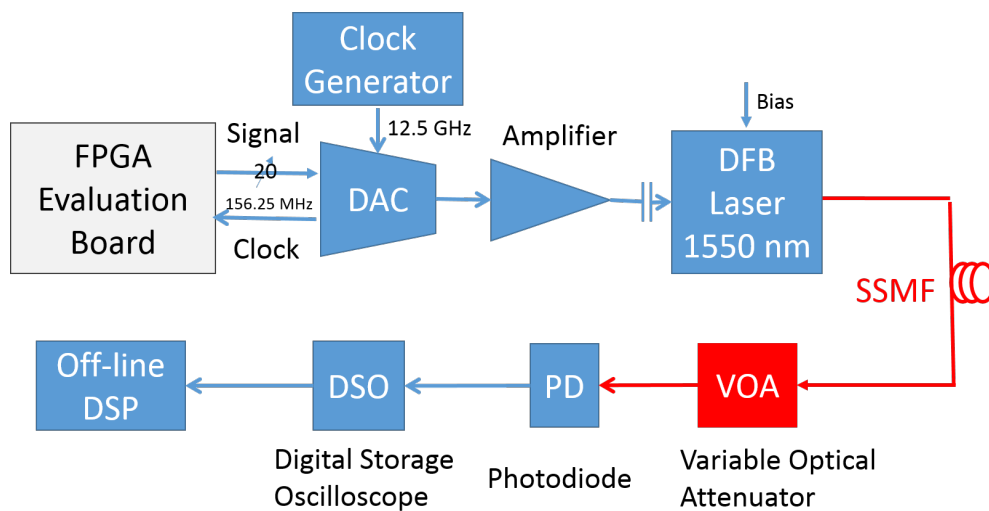
FIGURE 3.8: Experimental setup for both ACO-OFDM transmitters.
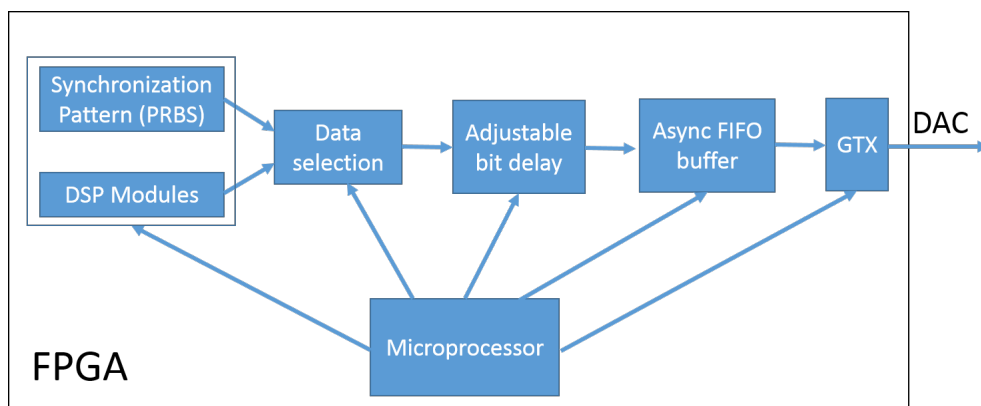
FIGURE 3.9: Design of the on-chip FPGA architecture. All high-speed modules are controlled via a microprocessor. Data selection module can switch the inputs between synchronization pattern and DSP data.

（a）

Data → Resample | Frame Sync. | Remove 32-sample CP | S/P | 128-point FFT | One-tap Equalization | QAM Decoder → Data

（b）

Data → Resample | Frame Sync. → Real → Remove 16-sample CP / Imag → Remove 16-sample CP → S/P | 64-point FFT | One-tap Equalization | QAM Decoder → Data
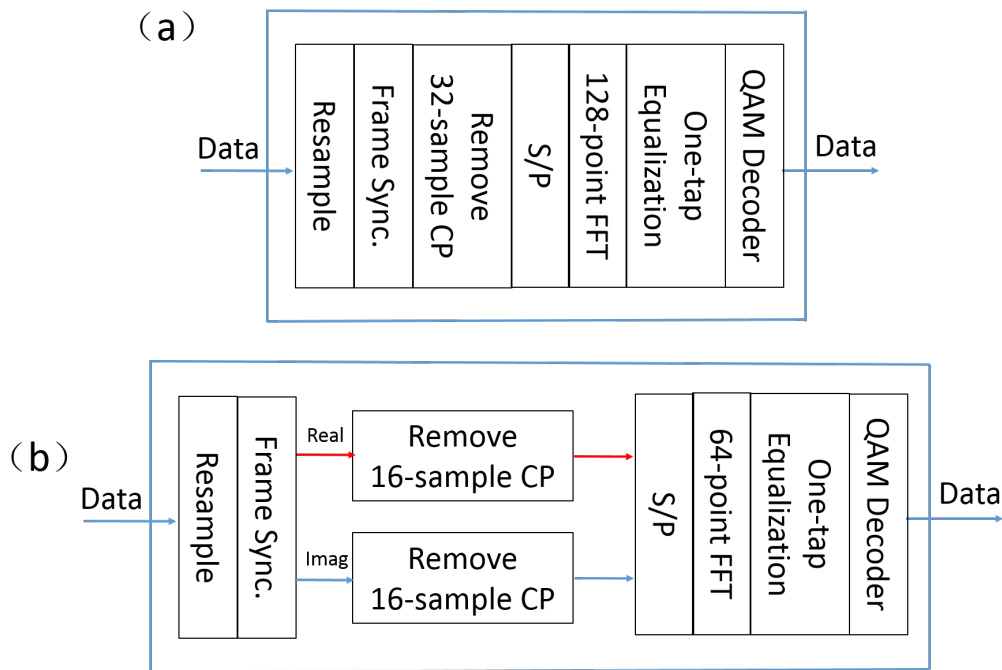
FIGURE 3.10: Offline DSP Algorithm in the ACO-OFDM receiver (a) HS IFFT (B) NHS IFFT.

The peak-to-peak voltage of DAC analog output signal was 500 mV. The signal was fed through 18-dB attenuators and a DC block, followed by a 24-dB gain 40-GHz linear electrical amplifier (SHF-807). The resulting 1-volt (p-p) output signal was connected to a distributed feedback laser, which was biased at 33 mA in this experiment. After transmission over a 15-km SSMF, a variable optical attenuator (VOA) was used to adjust the output optical power, followed by a 16-GHz pho-todetector (DSC-40S) to convert optical signals to electrical signals, which were then sampled by a real-time Digital Storage Oscilloscope (DSO-X92804A) with an 80-GS/s sampling rate. Finally, the captured samples were analysed by offline DSP in MATLAB, which is shown in the Fig. 3.10. All these parameters in the transmission link were the same for both ACO-OFDM transmitters.

3.3.5   Experimental Results

In this section, the transmission performance for both HS and NHS ACO-OFDM transmitter is measured. Firstly, by directly connecting the laser output to the VOA, the Q-factors for a back-to-back optical link were measured and shown in Fig. 3.11 and 3.12. The Q-factor for combined layers throughout this thesis is calculated from the weighted-average BER of all the layers. No optical attenuation was added by the VOA. In Fig. 3.11(b), it is very clear that the Q-factor for

high-frequency subcarriers are 3-dB lower than that for the low-frequency sub-
carriers due to the laser bandwidth limitation. In Fig. 3.12(b), because all the 16
data channels are independent, the first 8 data channels and the second 8 data
channels occupy the same bandwidth. The Q-factors in high-frequency subcar-
riers are still 3-dB lower than that in low-frequency subcarriers. However, the
average Q-factor for both the two schemes are very similar (22.01 dB for HS IFFT
and 22.35 dB for NHS IFFT).
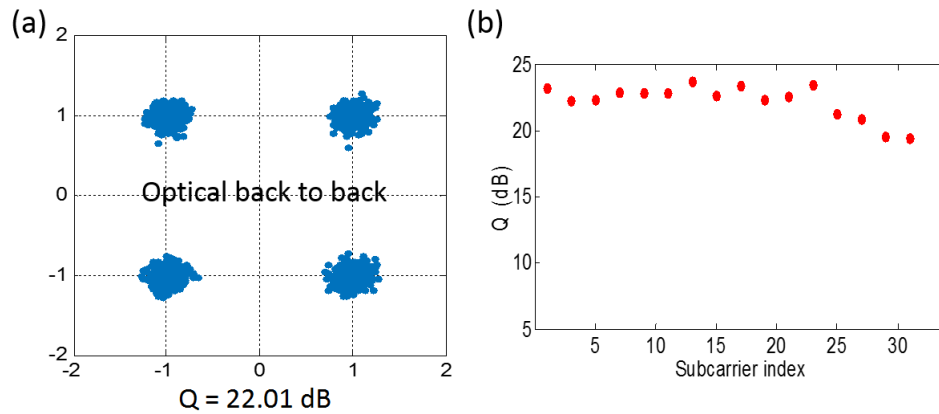
FIGURE 3.11: Q-factors for optical back-to-back using HS IFFT. The
higher-frequency subcarriers have a higher subcarrier index.
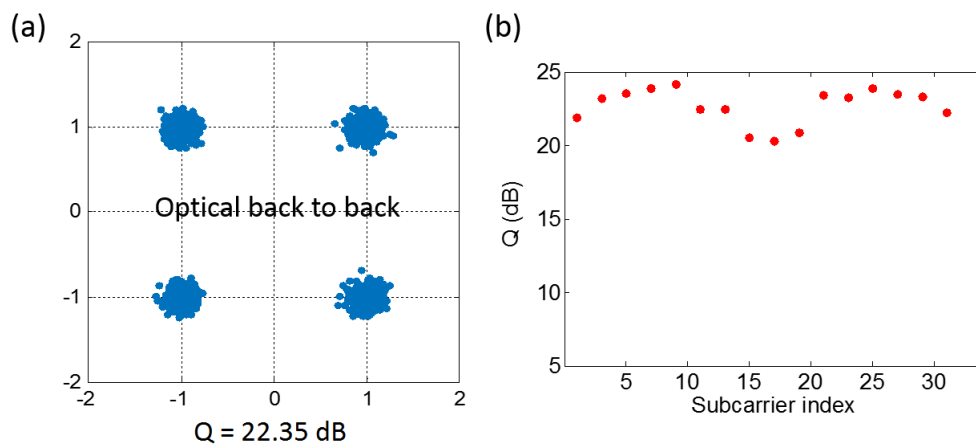
FIGURE 3.12: Q-factors for optical back-to-back using NHS IFFT.
The higher-frequency subcarriers fall on the middle of the subcarrier
index.

The Q-factors after transmission over 15-km SSMF were measured and shown
in Fig. 3.13 and 3.14. The average Q-factors for both the two schemes are still
very similar. Although the Q-factors in high-frequency subcarriers have a larger
penalty, compared with that in the low-frequency subcarriers, probably due to

the interaction of laser chirp and fiber dispersion, the Q-factors of subcarriers in the same frequency range for both the schemes show similar signal quality.
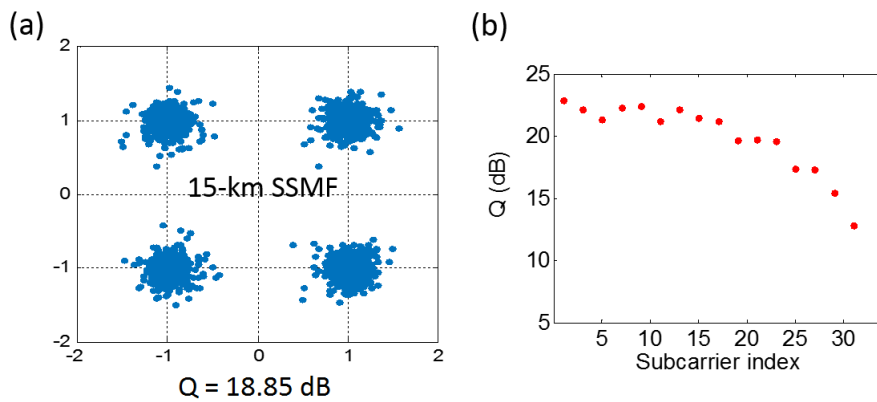
FIGURE 3.13: Q-factors for 15-km SSMF transmission using HS IFFT. The higher-frequency subcarriers have a higher subcarrier index.
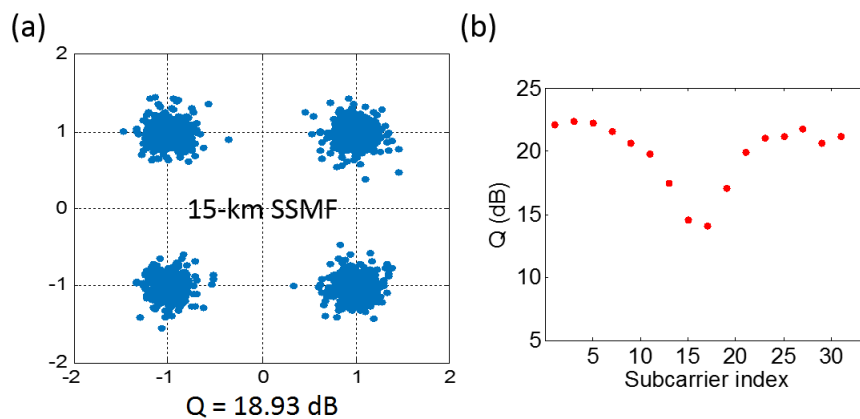
FIGURE 3.14: Q-factors for 15-km SSMF transmission using NHS IFFT. The higher-frequency subcarriers fall on the middle of the subcarrier index.

The Q-factors for both optical back-to-back and 15-km SSMF transmission are not affected by using HS or NHS IFFT implementation, which means that the NHS IFFT implementation can be used to replace the HS IFFT implementation in the real-time ACO-OFDM transmission links.

3.4 Conclusion

A computationally efficient IFFT implementation method for ACO-OFDM transmitter is proposed and implemented in a FPGA. The implementation results show that the overall computational complexity is reduced by 68%. The measured Q-factors for optical back-to-back and transmission over 15-km SSMF are

almost the same for both the HS and NHS IFFT implementation, proving that the NHS IFFT implementation can be used in the real transmission system, with a significantly reduced logic resource utilization, compared with HS IFFT implementation.

Chapter 4

Layered/Enhanced ACO-OFDM

4.1 Introduction

In Chapter 3, we have learned that odd-subcarrier ACO-OFDM [55] is more op-
tically energy efficient compared with DCO-OFDM because the DC bias is elim-
inated in the ACO-OFDM. However, by clipping the negative waveform sam-
ples to be zero-valued, ACO-OFDM introduces distortion terms that fall on the
even subcarriers. This requires the sacrifice of half of the subcarriers without
carrying any information, and therefore halves spectral efficiencies compared to
DCO-OFDM. Consequently, to achieve the same capacity as DCO-OFDM, ACO-
OFDM requires either the bandwidths of the electrical and optical devices to be
doubled, or the use of higher-order constellations, which then requires higher
signal to noise ratios. Layered/enhanced asymmetrically clipped OFDM (L/E-
ACO-OFDM) was proposed recently [63]–[67], with results showing that this
technique could improve the spectral efficiency of ACO-OFDM towards that of
DCO-OFDM, while still maintaining a power advantage. However, the power
advantage of LACO-OFDM over DCO-OFDM has not been verified in the trans-
mission experiments.

In this chapter, in the first part, L/E-ACO-OFDM (LACO-OFDM hereafter)
system is simulated to show its power advantage over DCO-OFDM up to 1024-
QAM. These simulations were done by Prof. Arthur Lowery and has been pub-
lished in Optics Express [66]. I would like to thank him for letting me show some
results in my thesis.

Then an LACO-OFDM experiment is conducted to explore its power advan-
tage over DCO-OFDM. All the DSP in the transceiver is performed offline using
MATLAB. In the transmitter, the driving signal is generated by arbitrary wave-
form generator (AWG) and in the receiver, the signal is captured by an oscillo-
scope. The experimental results show that LACO-OFDM can have a 3.8-dB and
2-dB Q-factor advantage over DCO-OFDM in optical back-to-back transmission

and over 19.8-km of optical fiber respectively. This part is from one of my contributed paper [183]. I took part in the experimental setup and results analysis. I would like to thank Mr. Binhuang Song for letting me show some results in my thesis.

As offline DSP does not take any practical hardware implementation issues into account, the overall system performance needs to be evaluated in a real-time transmission experiment. For DCO-OFDM, there have been many real-time demonstrations using field-programmable gate arrays (FPGA) [158]–[160], [162], [164]. In contrast to DCO-OFDM, a more complicated DSP algorithm is used in the transceiver for LACO-OFDM; its logic resource occupation is a big concern in the implementation because it will increase the power consumption and reduce data throughput. Therefore, the LACO-OFDM algorithm needs to be evaluated and optimized in a real-time optical communication system, in order to see the practicality of using this OFDM variant in real optical links. A real-time LACO-OFDM transmitter is demonstrated using a Virtex-6 FPGA in this chapter. By using radix-2 IFFT module, I firstly experimentally show that the required number of multipliers for the LACO transmitter is as the same as DCO-OFDM when they achieve the same spectral efficiency via optimization of all the IFFT modules individually. Even taking the adders into account, the LACO-OFDM transmitter just occupies slightly larger logic resource, compared with a DCO-OFDM transmitter. Finally, the implementation of LACO-OFDM transmitter is further simplified by using only one IFFT. Besides, I also evaluate the power budget and analyze the limiting factor on the Q-factor performance in a transmission experiment. In the transmission experiment, a 25 GSa/s MICRAM DAC with 5-bit resolution is used to generate the laser drive signal. A net data rate of 9.375 Gb/s is achieved when QPSK is encoded on the subcarriers. This LACO-OFDM optical signals are successfully transmitted over 20-km standard single mode fiber (SSMF) in a DML-based IMDD optical communication system. By encoding 16-QAM in the OFDM subcarriers, the data rate is doubled to be 18.75 Gb/s and it is successfully transmitted over 10-km SSMF with a Q-factor of 19.08 dB.

4.2 LACO-OFDM Algorithm

LACO-OFDM is developed from odd-subcarrier ACO-OFDM. The time domain signal generated by the IFFT in ACO-OFDM transmitter is antisymmetrical, so no information is lost by clipping all the negative parts to be zero [5]. In the frequency domain, only the odd subcarriers are used; the distortion generated by clipping the signals below their mean level falls only on where even subcarriers should be, so all the data encoded in the odd subcarriers can be decoded as the normal optical OFDM signal.
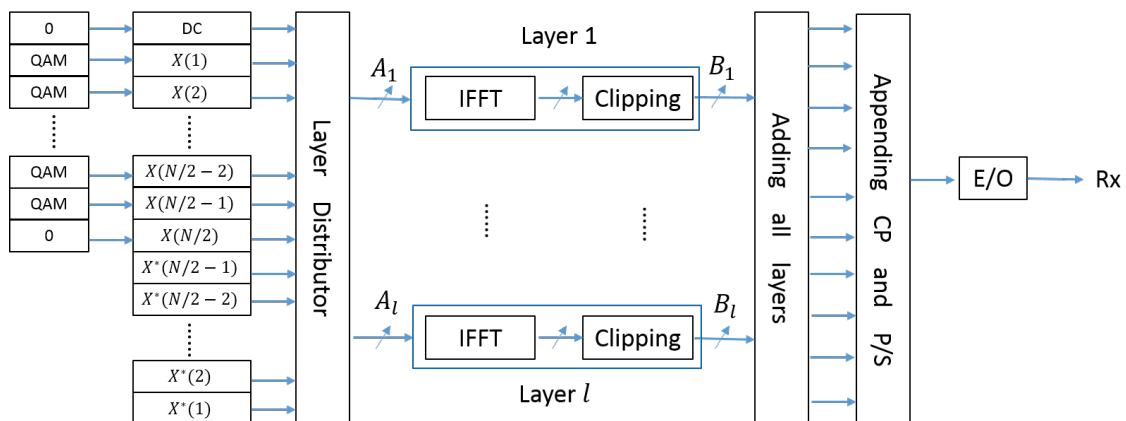
FIGURE 4.1: Block diagram of LACO-OFDM transmitter. The inputs of each IFFT are Hermitian symmetrical. The data-carrying subcarrier allocation in $A_1 - A_l$, the time-domian waveforms after IFFT and clipping are shown in Fig. 4.2 and Fig. 4.3.

The spectral efficiency of ACO-OFDM is reduced by half, in comparison with DCO-OFDM. LACO-OFDM allows the even-frequency subcarriers to be used, by adding a clipping distortion cancellation algorithm in the receiver, which removes the odd subcarriers (denoted as Layer 1) and their clipping distortion from the even frequencies. Thus, the even subcarrier frequencies can be allocated for data transmission by using more layers. However, not all of the even frequencies are available in the Layer 2. Layer 2 uses only the $2 \times$ odd subcarriers (i.e. subcarriers 2, 6, 10, etc.), because their clipping distortion will fall on $2 \times$ multiple subcarriers (i.e. subcarriers 4, 12, 20, etc). Further layers are required to occupy some of the remaining even frequencies. For example, Layer 3 uses only the $4 \times$ odd subcarriers if required.

The LACO-OFDM transmitter algorithm is illustrated in Fig. 4.1. In the common optical OFDM algorithm, the data is mapped to generated complex QAM signal. Combined with their Hermitian symmetrical signals, these QAM signals are distributed to different subcarriers in each layer. Each layer, L (1, 2, 3, 4, ...), uses a unique set of subcarriers, which have frequency indices $2^{(l-1)}(2l + 1)$,
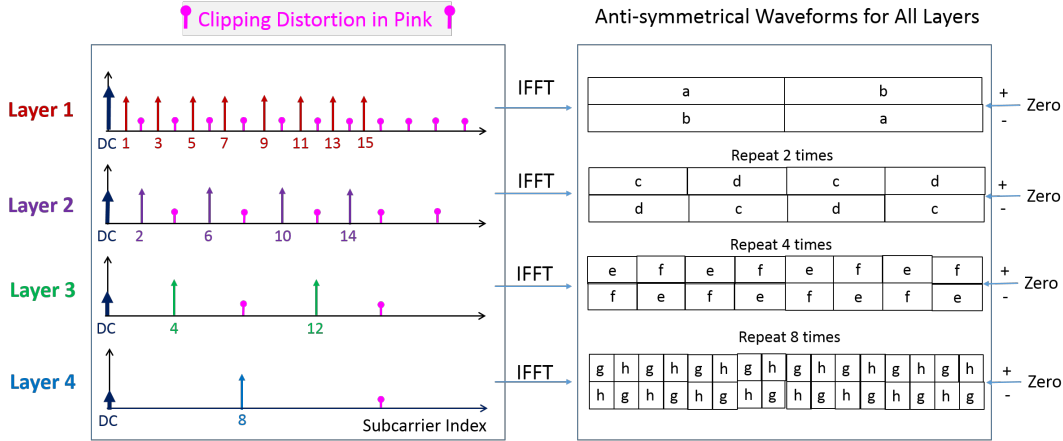
FIGURE 4.2: Data-carrying subcarrier allocation and waveforms after the IFFT in the LACO-OFDM transmitter if 4 layers are used. The portion marked 'a' means the portion in the first half and will be repeated in the negative portion in the second half. The portion marked 'b', 'c', 'd', 'e', 'f', 'g', 'h' has the similar meaning to show the antisymmetrical and cyclic waveforms in each layer.

where $l = (0, 1, 2, 3, \ldots)$. The spectral utilization of LACO-OFDM is $1/2 + 1/4 + 1/8 + \ldots$, compared with $1/2$ for ACO-OFDM. Because $X(0)$ and $X(N/2)$ are usully set to be zero to avoid any DC shift in OFDM communication systems, so LACO-OFDM can theoretically achieve the same spectral efficiency as DCO-OFDM. When four layers are used, the allocation of data-carrying subcarriers of each layer at Point A of Fig. 4.1 is shown in Fig. 4.2. The data-carrying subcarrier is seleted to make sure that the clipping distortion from higher layers does not fall upon the data-carrying subcarriers in the lower layers. For example, all the odd subcarriers are not polluted by clipping distortion and all the data-carrying subcarriers from Layer 2 are only influenced by the clipping distortion from Layer 1. Each layer generates a superposition of its subcarriers using an IFFT. The waveform of each layer after IFFT is shown in the Fig. 4.2. The time domain signal in each layer is antisymmetrical, so the negative values of this layer's waveform can be clipped to become zero-valued without losing the data. After clipping, the waveform of each layer at Point B of Fig. 4.1 is all non-negative values, as shown in Fig. 4.3. Finally, the already-clipped waveforms of all layers are combined to achieve a unipolar signal output. After appending CP in front of every OFDM symbol and parallel to serial conversion, the LACO-OFDM signals are used to drive the laser or LED directly without requirement of an added DC bias.

The LACO-OFDM receiver algorithm is shown in Fig. 4.4 and the spectral analysis in the decoding is shown in Fig. 4.5. In the receiver, a PD is usually used

All the waveforms are non-negative values
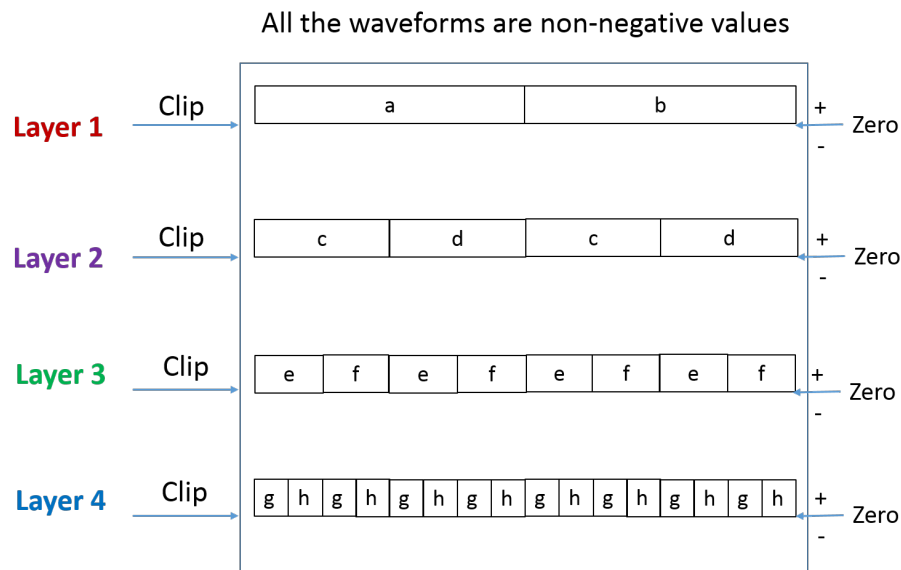
FIGURE 4.3: Waveforms after clipping in the LACO-OFDM transmitter if 4 layers are used. 'a', 'b', 'c', 'd', 'e', 'f', 'g', 'h' are all positive values. The waveforms are periodical in higher layers.

to convert optical signals to electrical signals. After CP removal and serial-to-parallel conversion, an iterative decoding algorithm is used to recover the data layer by layer. As the clipping distortion from all the layers does not fall on the odd subcarriers, which are the data-carrying subcarriers in Layer 1. Thus Layer 1 can be decoded first, using a FFT and a slicer. After obtaining the data carried in Layer 1, a facsimile of Layer 1's transmitted waveform can be regenerated with the same IFFT and clipper used in the transmitter, and then subtracted from the received waveform, to reveal the subcarriers (and clipping distortion) of the higher layers. Layer 2 is next decoded as Layer 1 using a FFT and a slicer, because Layer 2 is only polluted by the clipping distortion from Layer 1, which has been removed in the previous step. The spectrum within the LACO-OFDM after the clipping distortion removal is also shown in the Fig. 4.5. After decoding the data in the Layer 2, its clipping distortion is regenerated and then subtracted from W2, to reveal Layer 3 in the procedure of W3. Now the data-carrying subcarriers in Layer 3 is free of clipping distortion. Therefore, the data in all layers can be decoded correctly in this iterative way.

（a）

（b）
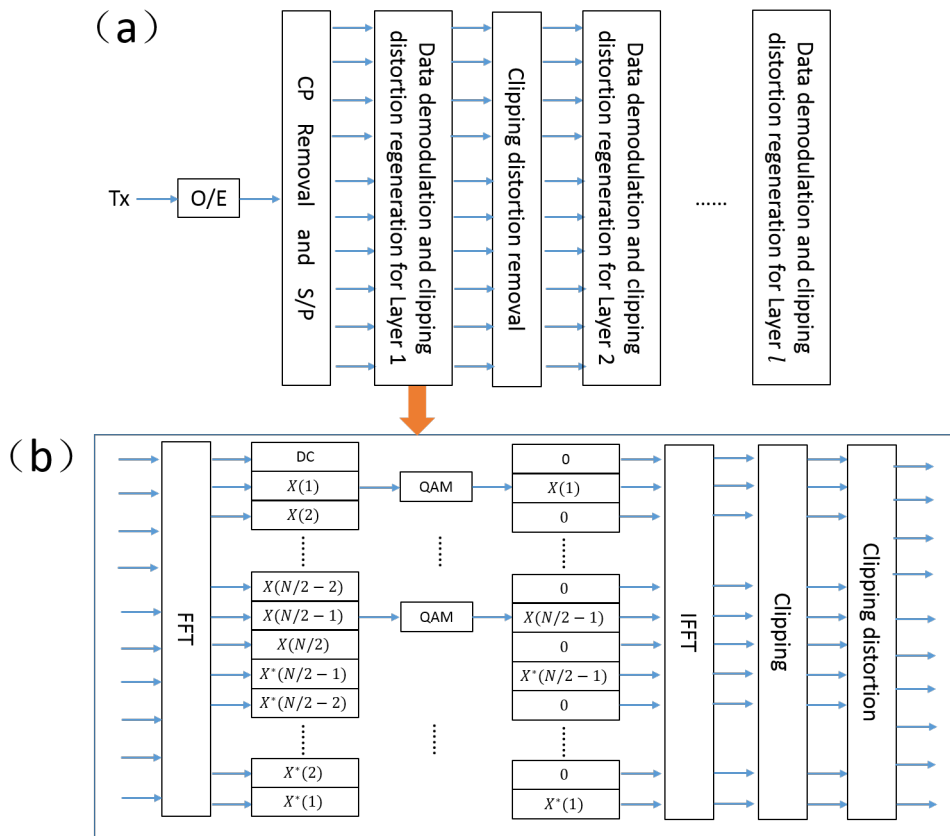
FIGURE 4.4: Block diagram of LACO-OFDM receiver. (a) Main functional blocks (b) Detailed DSP used for data demodulation and clipping distortion regeneration for Layer 1.
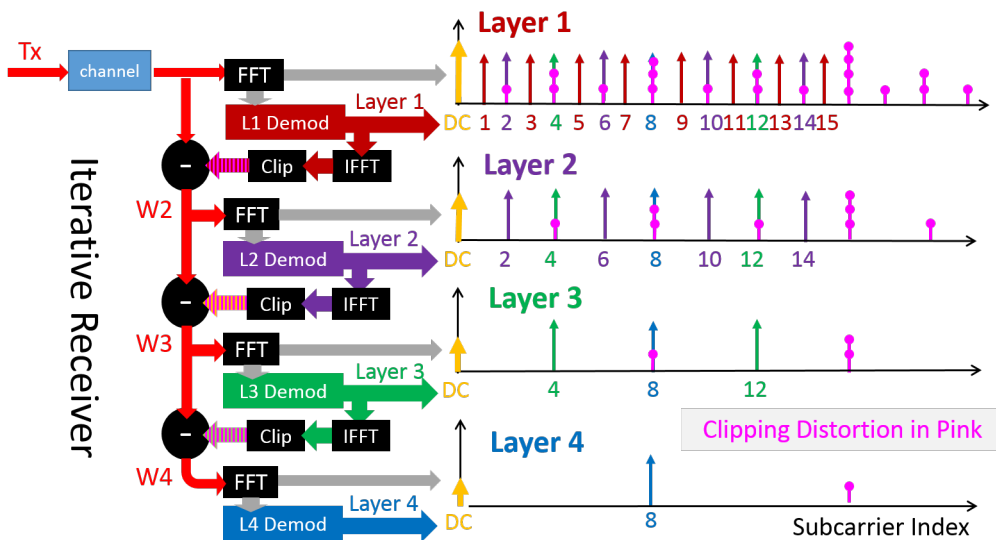
FIGURE 4.5: Iterative decoding and spectral analysis in the LACO-OFDM receiver if 4 layers are used. The clipping distortion is marked in pink. The data-carrying subcarriers in Layer 2, 3, 4, are revealed by removing these clipping distortion.

4.3 LACO-OFDM Algorithm Simulation

In 2015, by using VPItransmissionMaker, Lowery developed several simulations, proving that LACO-OFDM could achieve a better signal quality compared with DCO-OFDM and other schemes under the same SNR, while they were transmitted at the same data rate. In this section, only the comparison with DCO-OFDM is shown. A fully comparison can be found in this Optics Express paper [66].
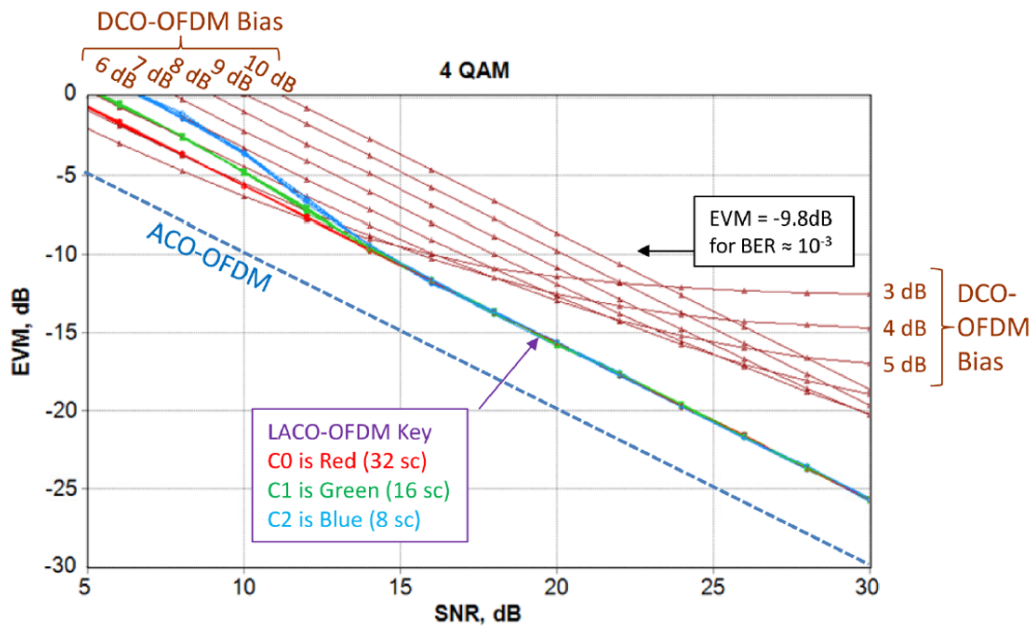
FIGURE 4.6: EVM versus SNR for 4-QAM LACO-OFDM and DCO-OFDM. The dashed line is the EVM that would be obtained with a 56-subcarrier ACO-OFDM system using approximately twice the spectral bandwidth. Reprinted with permission from ref [66], [OSA].

The simulation model is generally described here. An LACO-OFDM system with three layers and a DCO-OFDM system were simulated and compared. The Fourier transform lengths were 1024 points, with all layers occupying up to the first 64 subcarriers excluding DC. Therefore, the number of data-carrying subcarriers in the three layers were 32, 16 and 8. The same data-carrying subcarriers were used in the DCO-OFDM system. Therefore, the data rate of both systems were $2 \times 10G \times (32+16+8)/64 = 17.5$ Gb/s. The OFDM symbol rate and the simulation sampling rate was 10 Gsymbol/s and 160 Gsamples/s, giving the 16-times oversampling rate in the simulations. A total of 256 OFDM symbols were simulated. The transmitted signal for LACO-OFDM and DCO-OFDM operating at the same optical power. In the receiver, noise was added to the photocurrent after

the PD converted the optical signals to electrical signals. After the Fourier transforms, the Error Vector Magnitude (EVM) was estimated from the spreads of the constellation points and a knowledge of the transmitted data.

The EVM of the 4-QAM (QPSK) modulated LACO-OFDM and DCO-OFDM are plotted in the Fig. 4.6. The DC bias for DCO-OFDM is adjusted in a step of 1 dB. It can be concluded that the signal quality in all layers of LACO-OFDM is better than the optimum DCO-OFDM for SNRs above 13.5 dB by showing a comparative lower EVMs. As expected, the error propagation among the higher layers occurs at low SNR because a large amount of slicing errors cannot be avoided at this area. However, by further improving the SNRs, for example, at SNRs > 15 dB, the EVMs in all the three layers show similar performance. Furthuremore, at higher SNRs, the EVM of LACO-OFDM improves 1 dB per dB increase in SNR, while for DCO-OFDM, there is around 0.8 dB reduction in EVM per dB increase in SNR. Therefore, LACO-OFDM can achieve a better signal quality if a higher SNR is available.
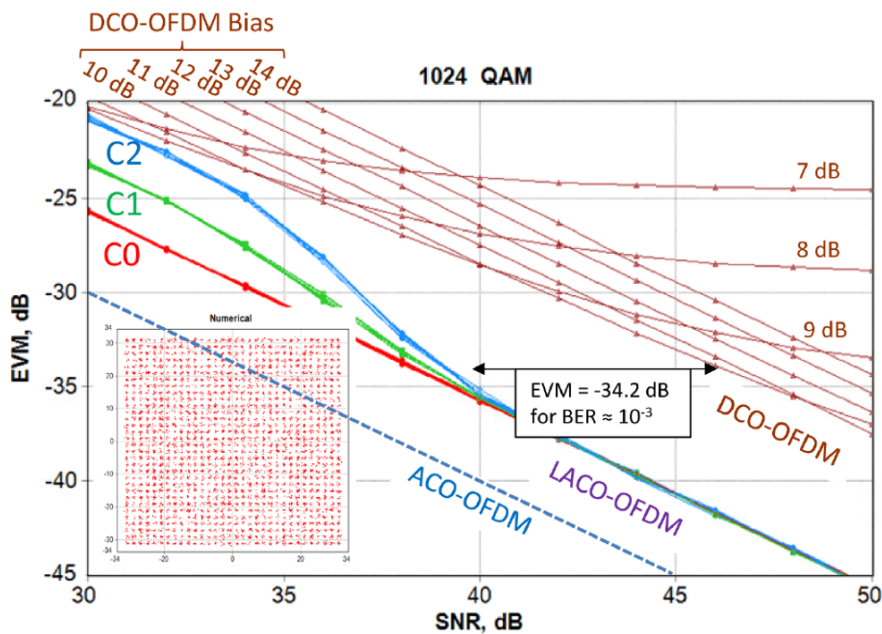
FIGURE 4.7: EVM versus SNR for 1024-QAM LACO-OFDM and DCO-OFDM. The slicers work effectively in higher SNR, but not quite as effectively as for 4-QAM. Reprinted with permission from ref [66], [OSA]

Higher spectral efficiency modulatin formats are preferred in the OFDM subcarriers because it can reduce the required bandwidth of electrical device which is very valuable in optical communication systems. Fig. 4.7 plots the EVM for the LACO-OFDM and DCO-OFDM using 1024-QAM modulation. Compared with 4-QAM, higher SNRs are required to support 1024-QAM. At the higher SNRs,

to achieve a lower BER $< 10^{-3}$, the reduction in EVM for 1024-QAM modulated LACO-OFDM is as larger as to be 7 dB. However, as the 1024-QAM requires relatively larger SNRs to achieve the same BER compared with 4-QAM, its penalties is also far higher at low SNRs due to the more severe slicing errors. For instance, there is a 5-dB difference in EVM's performance between Layer 1 and Layer 3 for 1024-QAM, compared with 1 dB for 4-QAM. This performance difference has reduced to < 0.8 dB at the EVM required for a BER of 10^{-3}.

4.4 Offline LACO-OFDM Transmission Experiment

Although many simulations on LACO-OFDM have demonstrated its power advantage over DCO-OFDM [63]–[67], an experimental proof that LACO-OFDM is more power efficient is required. Because a direct modulate laser must be biased above its threshold current in order to have a resonable frequency response and low transient distortion. This could reduce the power efficiency advantage of an LACO-OFDM signal, because the laser spends more times at low powers, which are close to the threshold, than when driven by DCO-OFDM signals, and hence is slow to turn on. In this section, the first experimental demonstration of LACO-OFDM will be provided and compared with DCO-OFDM in short-haul optical fiber link.

4.4.1 Truncated Second-Order Volterra Filter

As we have shown in previous chapters, a bank of one-tap frequency domain equalizers are used for OFDM signals conventionally, one for each subcarrier. In this experiment, a Volterra filter time-domain equalizer is used in the receiver to compensate nonlinear distortions in the transmission system, which has not been considered in the previous simulations. Therefore, the influence of the nonlinear distortion on the signal transmission of LACO-OFDM and DCO-OFDM can be concluded.

Volterra filters have been used to compensate chromatic dispersion-induced and chirp-induced distortions in optical communication systems [184], [185], and nonlinear distortion in high power amplifiers in wireless systems [186]. Because of the square-law detection in an IM/DD system, a second-order Volterra filter is most suitable. The output, $y(k)$, of a truncated Volterra filter is:

$$y(k) = \sum_{l_1=0}^{L-1} w_1(l_1)x(k - l_1) + \sum_{l_1=0}^{L-1}\sum_{l_2=0}^{L-1} w_2(l_1, l_2)x(k - l_1)x(k - l_2) \qquad (4.1)$$

where: x is the input signal; w_1 and w_2 are weights for linear and second-order terms. Equation 4.1 is a linear finite impulse response (FIR) filter with L taps plus a second-order FIR filter with $L(L+1)/2$ taps. The second term operates on the cross-products between different samples, x_k. By considering the memory length of the channel and computing complexity, $L = 10$ is chosen for this experiment. A training sequence with a least-mean-square algorithm is used to update the weights. This time domain equalizer can deal with arbitrary modulation formats, as it only performs waveform correction.

4.4.2 Experiments

Fig. 4.8 shows the experimental setup for QPSK modulated DCO-OFDM and LACO-OFDM. The DCO-OFDM signal was generated in MATLAB with 256-point IFFT. By using 2 × oversampling rate and Hermitian symmetrical inputs, only 63 subcarriers were used to carry data, with the 1st subcarrier left for DC bias. For LACO-OFDM, 3 layers were used. With the same IFFT size and oversampling rate, each layer carried 32, 16 and 8 subcarriers separately. Therefore, the LACO-OFDM's spectral efficiency was 87.5% ((32+16+8)/64) of DCO-OFDM. However, the data rate of both DCO-OFDM and LACO-OFDM was 4.375-Gb/s because the Tektronix 7102 arbitrary waveform generator (AWG) set to be 8.75 Gsample/s for DCO and 10 Gsample/s for LACO-OFDM; however, the bandwidth is expected to be very close to DCO-OFDM when more layers are used. The laser was a Gooch and Housego AA0701 DFB. The output of a 13-GHz photodiode was sampled by a 28-GHz real-time digital oscilloscope (Agilent DSO-X92804A) at 10 GSample/s. In the receiver, either frequency-domain one-tap equalization or time-domain Volterra equalization was used for both DCO-OFDM and LACO-OFDM.
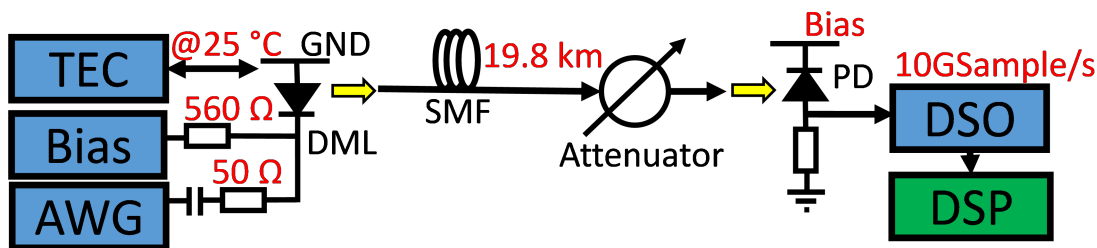
FIGURE 4.8: Experimental setup. DSP: offline digital signal processing. AWG: arbitrary waveform generator. DML:direct modulated laser. TEC: temperature controller. SMF: single mode fiber. PD: photodetector. DSO: digital oscilloscope.

The Q-factors for two OFDM formats were measured at different laser operating bias currents in a 19.8-km SSMF short-haul link, as shown in Fig. 4.9. Either TD Volterra equalization or FD equalization was used for both types of OFDMs. The results showed the Volterra equalizer improved the signal quality for both OFDM signals. At 16-mA bias, LACO-OFDM achieved a 2-dB Q-factor improvement over DCO-OFDM. At high biases, the signal quality for both OFDM signals was similar though DCO-OFDM was slightly better than LACO-OFDM at a bias of > 19 mA. However, it was apparently that LACO-OFDM could approach to the highest Q-factor at a lower bias by some simple calculations. The bias currents to maintain the Q-factors above 13 dB were 16.5 mA (LACO-OFDM) and 18 mA (DCO-OFDM), equivalent to 4.1 mA and 5.6 mA above threshold (12.4 mA). That said, LACO-OFDM saved (5.6-4.1)/5.6=27% of the bias current, compared with DCO-OFDM.
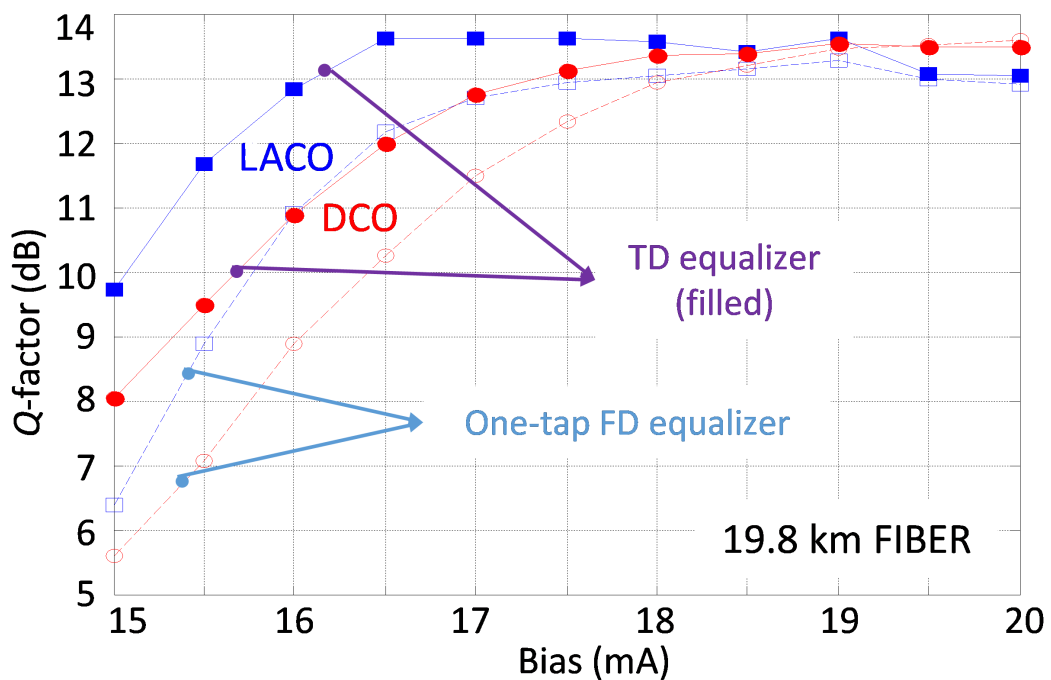
FIGURE 4.9: Q-factor versus different bias for LACO-OFDM (blue line with circles) and DCO-OFDM (red line with diamonds) after 19.8-km optical fiber transmission. Solid line with filled symbols: using time domain equalizer. Dashed line with clear symbols: using frequency domain one-tap equalizer.

4.5 Real-time LACO-OFDM Signal Generation

4.5.1 IFFT Implementation for LACO Transmitter

The spiral FFT/IFFT IP core generator can automatically generate customized FFT/IFFT soft IP cores in synthesizable register-transfer level Verilog [180]. These cores have previously been used in some experimental demonstrations [159], [187], in order to verify different DSP algorithms in a real-time optical transmission link. Therefore, for simplicity, this IP core was used to generate the IFFT modules in the LACO-OFDM and DCO-OFDM transmitter.

4.5.1.1 Four IFFT Method

This method is called Scheme 1. Section 4.2 shows that several layers are needed in an LACO-OFDM transmitter to increase the spectral efficiency of ACO-OFDM. The waveform of each layer must be generated and clipped independently at the transmitter to allow the receiver to decode the data layer-by-layer in the iterative way. The technique would not work if the entire bandwidth was occupied and then clipped as one before transmission. One IFFT module is used in every layer. Generally, larger FFT sizes are preferred to reduce the lower cyclic prefix (CP) overhead, which gives robustness to intersymbol interference (ISI). However, the limited logic resources of FPGAs put an upper bound on the FFT size. In this experimental demonstration, a 128-point IFFT core was implemented in the first layer. In LACO-OFDM, five layers will give 100% of the spectral efficiency of DCO-OFDM because the DC (0th) subcarrier is usually not used to carry information to avoid DC drift. However, the more layers used, a more complicated iterative receiver is required. Since the fifth layer only adds one data-carrying subcarrier, four layers were adopted in this demonstration. Therefore, the FFT sizes for the four layers were 128, 64, 32, 16, for Layers 1 to 4, respectively. The numbers of subcarriers occupied in Layers 1 to 4 were 16, 8, 4, 2, so there were 30 subcarriers in total giving 96.8% (30/31) of the spectral efficiency of DCO-OFDM-OFDM, with the DC subcarrier excluded.

TABLE 4.1: Multiplier utilization in different sized IFFT.

IFFT Size	Number of Multipliers
16	20
32	76
64	244
128	700

The FPGA was programmed as follows. It is well known that a larger-radix IFFT can be used to reduce the required number of multipliers. For simplicity, radix-2 IFFT modules are used in all the four layers in this implementation. Firstly, four fully-streaming radix-2 IFFT modules, whose size is 128, 64, 32 and 16, were generated using spiral FFT IP core generator. Because multipliers dominate the IFFT computation complexity, the required number of multipliers for the different size of IFFT are tabulated in Table 4.1. For the DCO-OFDM transmitter, only one 128-point IFFT is required, requiring 700 multipliers. Correspondingly, the total number of multipliers used by the four IFFT in LACO-OFDM transmitter is 1040 (700+244+76+20). More layers in the LACO-OFDM transmitter definitely cause a significant increase of the logic resource occupation compared with a DCO-OFDM transmitter. Because the increase of computational complexity will lead to the increase of power consumption, it will reduce the power efficiency of LACO-OFDM over DCO-OFDM. Therefore, the computation complexity of LACO-OFDM should be reduced, making it more competitive to replace DCO-OFDM in the real transmission link.

4.5.1.2   Optimized Implementation of Four-IFFT Method

In this section, the optimization of the logic resource utilization will be achieved by taking advantage of its zero-valued inputs of each IFFT in the LACO-OFDM transmitter. This method is called Scheme 2.

OFDM can be simply considered as a multicarrier modulation scheme, where its subcarrier frequencies are carefully selected to make sure that each subcarrier is orthogonal to the other subcarriers over one OFDM symbol period. Commonly, an IFFT module is used to achieve modulation and multiplexing digitally in the transmitter. If $x(n)$ represents the OFDM time domain signals over one symbol, we have

$$x(n) = \frac{1}{N} \sum_{k=0}^{N-1} X(k) \exp(\frac{-j2\pi kn}{N}), \tag{4.2}$$

where $n, k = 0, 1, \ldots, N-1$ and $X(k)$ is the input signal of IFFT module. In the first layer, only the odd subcarriers are used to carry data and all the even subcarriers are simply set to zero. Therefore, Equation 4.2 can be simplified to

$$x(n) = \frac{1}{N} \sum_{k=0}^{N/2-1} X(2k+1) \exp(\frac{-j2\pi(2k+1)n}{N}). \tag{4.3}$$

So,

$$
\begin{aligned}
x(n + N/2) &= \frac{1}{N} \sum_{k=0}^{N/2-1} X(2k+1) \exp(\frac{-j2\pi(2k+1)(n+N/2)}{N}) \\
&= x(n) \exp(-j\pi(2k+1)) \\
&= -x(n),
\end{aligned}
\tag{4.4}
$$

where $n, k = 0, 1, \ldots, N/2 - 1$ [65]. For illustration, a 16-point decimation-in-time radix-2 IFFT butterfly chart is shown in Fig. 4.10. Because only the odd subcarriers are used to carry data in the first layer of LACO-OFDM, all the data-carrying subcarriers fall on the bottom-half of the butterfly. Therefore, all the numbers in the top half (red) are zero-valued except for the numbers $x(0), x(1), ..., x(7)$ in the last butterfly. However, $x(0), x(1), ..., x(7)$ can be obtained from $x(8), x(9), ..., x(15)$ directly because they just differ in sign. This also explains why the time-domain signals in the LACO-OFDM's first layer are antisymmetrical as Equation 4.4. From the perspective of implementation, only the numbers in the bottom half are required to be calculated, so the computational complexity of IFFT module in the first layer is significantly reduced. Please note that the inputs of IFFT are Hermitian symmetrical pairs by default in this chapter. It does not influence the correctness of our results. The size-efficient implementation used in Chapter 3 can still be used to eliminate Hermitian symmetrical constraints if necessary.

In the second layer of LACO-OFDM, only even subcarriers are used to carry data. In this case, Equation 4.2 can be simplified to

$$
\begin{aligned}
x(N) &= \frac{1}{N} \sum_{k=0}^{N/2-1} X(2k) \exp(\frac{-j2\pi 2kn}{N}) \\
&= \frac{1}{N} \sum_{m=0}^{N/2-1} X(m) \exp(\frac{-j2\pi mn}{N/2}),
\end{aligned}
\tag{4.5}
$$

where $X(m) = X(2k), m = 0, 1, \ldots, N/2 - 1$. Apparently, $X(m)$ is composed of even subcarriers of $X(k), k = 0, 1, \ldots, N - 1$. And we can also get

$$
\begin{aligned}
x(n + N/2) &= \frac{1}{N} \sum_{m=0}^{N/2-1} X(m) \exp(\frac{-j2\pi m(n+N/2)}{N/2}) \\
&= x(n) \exp(-j2\pi m) \\
&= x(n),
\end{aligned}
\tag{4.6}
$$

where $n, m = 0, 1, \ldots, N/2 - 1$. In Fig. 4.11, which shows the processingof Layer
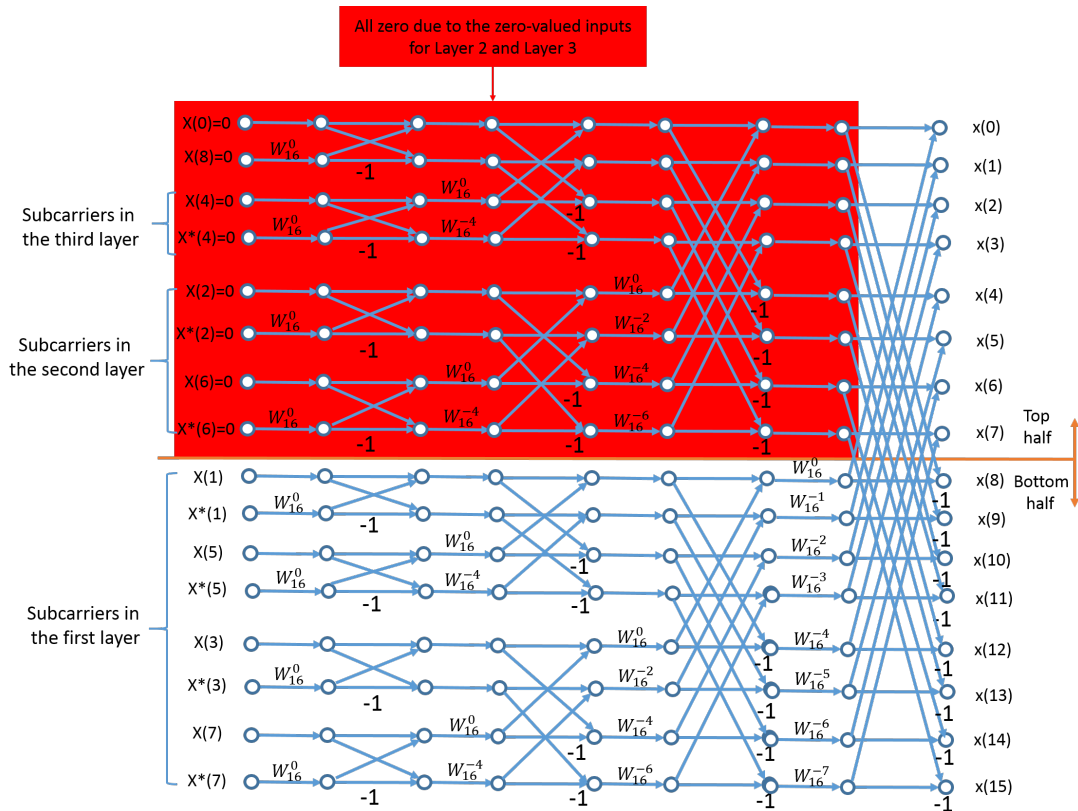
FIGURE 4.10: An 16-point radix-2 DIT IFFT butterfly flow chart.
The inputs are mapped with data-carrying subcarriers from the first
Layer.

2, all the numbers in the bottom half (red) are zero-valued, which is the reason why the time domain signals in the second layer repeat twice within one symbol, as per Equation 4.6. From the perspective of implementation, only an 8-point IFFT in the top half is required to be calculated and the 16-point outputs in the second layer can be generated by simply duplicating the 8-point IFFT outputs. Therefore, the IFFT size for the high layers can be reduced by $2^{(L-1)}$, with $L = 1$, 2, 3, 4 etc. and the waveforms in higher layers can be obtained by repeating the outputs of the smaller-sized IFFT. As we have discussed in Section 2, not all of the even frequencies are available in the second layer, only the $2 \times$ odd subcarriers ($x(2)$, $x(10) = x^*(2)$, $x(6)$, $x(14) = x^*(6)$ in Fig. 4.11) are used.

In Fig. 4.11, $x(0)$ (DC) and $x(8)$ (Nyquist) are all zero-valued required by the Hermitian symmetrical constraints. $x(4)$ and $x(12) = x^*(4)$ are the inputs from Layer 3. For the generation of waveform for Layer 3, the previous implementation method used in the first and second layer can be repeated again because the IFFT's inputs of Layer 1 and Layer 2 are zero-valued. Therefore, only a 4-point IFFT is required for the waveform generation of Layer 3. We can conclude
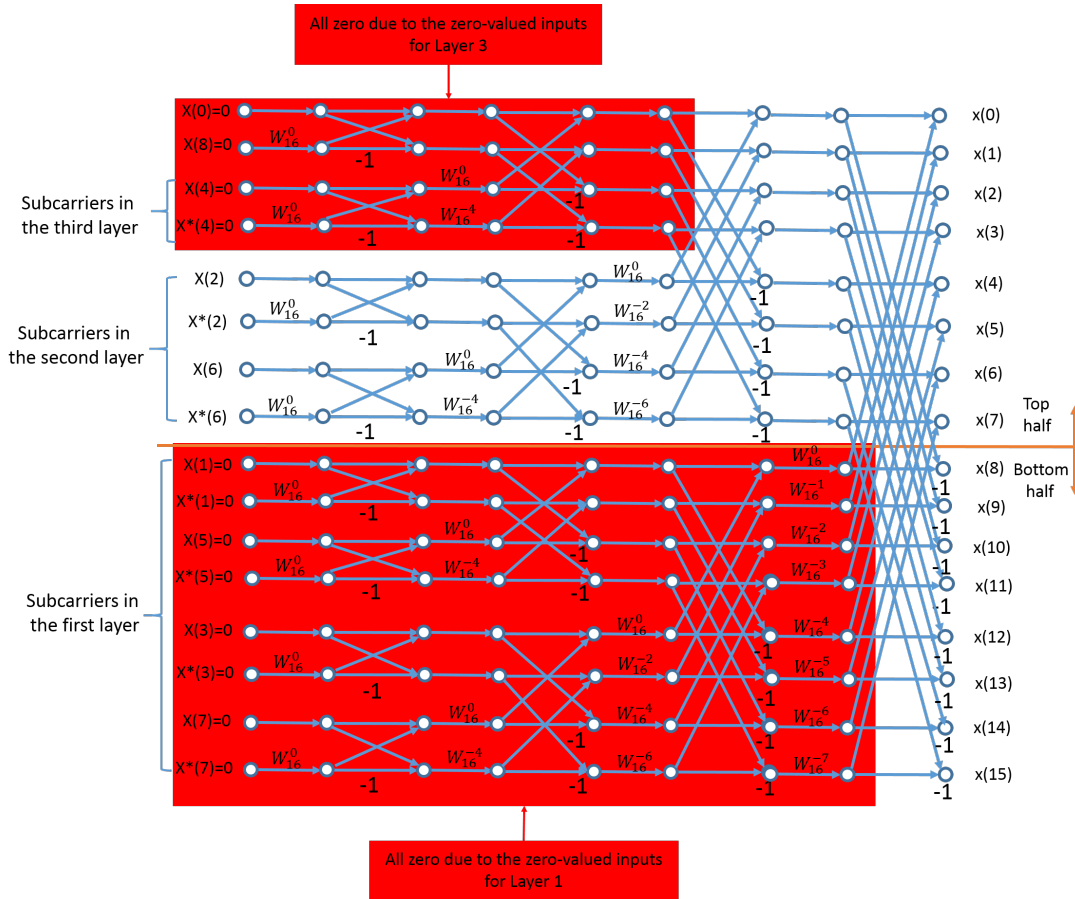
FIGURE 4.11: A 16-point radix-2 DIT IFFT butterfly flow chart. The
inputs are mapped with data-carrying subcarriers from the second
Layer.

that this implementation method also applies to the fourth and even higher lay-
ers for a larger-sized IFFT until the IFFT's implementations in all the layers are
optimized.

In short, for four-IFFT implementation, two methods can be used to simplify
the implementation of radix-2 IFFT modules in the LACO-OFDM transmitter: a
smaller IFFT size and waveform duplication can be used in the higher layers,
while at the same time only the calculations in the bottom half of butterfly chart
are required to be conducted in all the layers. As these two optimization methods
do not change the butterfly flow, almost all the pipeline and parallel implemen-
tation methods used for conventional radix-2 IFFT implementation can still be
used in our implementation without any large modification.

4.5.1.3   Single IFFT method - *middle-out* IFFT

Although it is possible to reduce the computational complexity of LACO-OFDM
transmitter using the previous method, the requirement of optimizing each IFFT's

implementation still remains complicated compared with DCO-OFDM that re-
quires only one IFFT. In this section, a standard IFFT will be modified to extract
the waveforms for each layer from within the core of the IFFT, so only one IFFT,
which is called *middle-out* IFFT hereafter, is used for the LACO-OFDM transmit-
ter. This method is called Scheme 3.
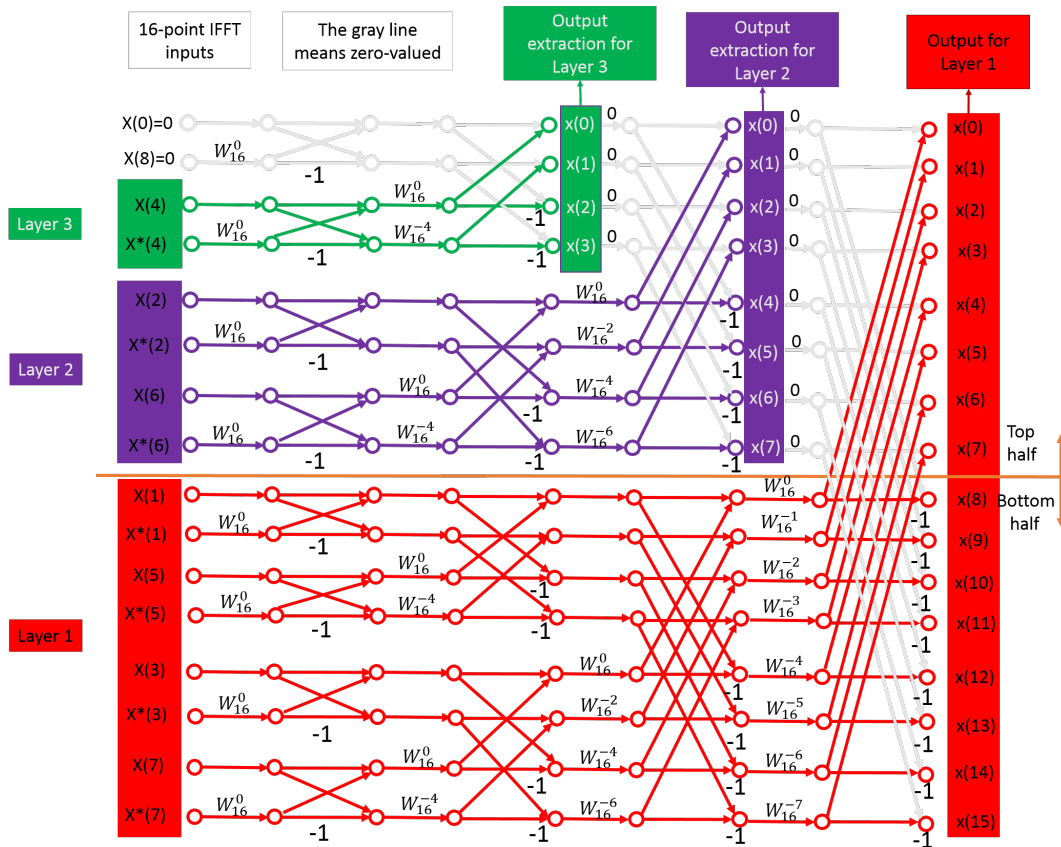
FIGURE 4.12: *middle-out* IFFT implementation illustrated by a 16-
point radix-2 DIT IFFT butterfly. The data stream in each layer is
marked with different colour. The data flow in higher layers works
in the same principle when a larger IFFT size is used.

The same 16-point radix-2 decimation-in-time IFFT butterfly is used to illus-
trate the *middle-out* IFFT implementation method, as shown in Fig. 4.12. Due to
the limited size of IFFT, only three layers are shown. It should be mentioned that
the Hermitian symmetrical inputs are used, but it is not necessary for this effi-
cient implementation. Firstly, all the data-carrying subcarriers are distributed to
the inputs of one IFFT. The data from Layer 1 all falls on the bottom-half butterfly
and the data from Layer 2 and Layer 3 all falls on the top-half butterfly. As the
data in the first layer flows only in the bottom-half butterfly except in the final
butterfly, we can extract the IFFT's outputs from Layer 2 and replaced them with
zero before they pollute the IFFT's output from Layer 1. After this point, the data

from bottom half and top half will influence each other. Besides, the the tempo-
rary calculation results (Green), which can be used to generate the waveform of
Layer 3, must be extracted before the extraction procedure of Layer 2. The extrac-
tion points for Layer 2 (purple) and Layer 3 (Green) are plotted in Fig. 4.12. These
extraction results can be repeated two times to form the waveform of Layer 2 and
repeated four times to form the waveform of Layer 3 [65].
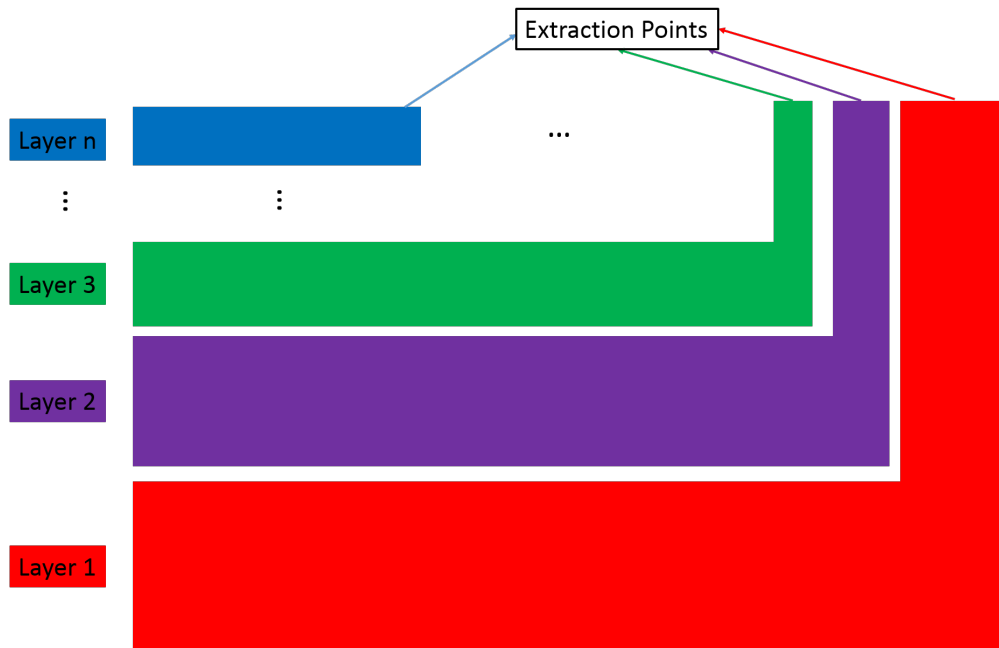
FIGURE 4.13: Layer distribution and waveform extraction in *middle-
out* IFFT implementation. The data stream in each layer is marked
with different colour. The data from higher layers will be extracted
and replaced by zero before it influences the data from lower layers.
These extracted results will be used to generate the waveform of its
own layer. Note that extraction implies that zeros are sent forward
to the next butterfly, i.e. zeros replace the extracted signals.

The same extraction method also applies to all the higher layers if a large
IFFT size is used. The general distribution and extraction method for a N-point
IFFT is shown in Fig. 4.13. By carefully distributing the data from different layers
into the inputs of one IFFT, slightly modifying the standard IFFT butterfly and
extracting temporary results from within the IFFT, only one IFFT is required in
the implementation of LACO-OFDM transmitter. It will difinitely simplify the
implementation of LACO-OFDM transmitter.

4.5.1.4 Logic Resource Utilization

From Table 4.1, we have shown that LACO-OFDM requires around 1.5 times logic resource, in contrast with DCO-OFDM. In this section, the implementation results of Scheme 2 and Scheme 3 (four layers are used) are shown. In Scheme 2, we modified the generated Verilog code to guarantee that only the bottom half in the IFFT butterfly would be calculated. This modification can still be used even if larger-radix IFFTs are used in different layers. After optimization, the required number of multiplier of each IFFT is tabulated in Table 4.2. In Scheme 2, LACO-OFDM transmitter require 696 multipliers, which is slightly lower than the 700 multipliers used by one 128-point IFFT module in the DCO-OFDM transmitter. The reason that LACO-OFDM uses fewer multipliers is that only 30 subcarriers are used to carry data, making LACO-OFDM slightly less spectrally efficient than DCO-OFDM. If a fifth layer is added to take all the subcarriers (except DC subcarrier) to carry data, another 8-point IFFT module requiring 4 multipliers needs to be implemented. In this situation, the total required number of multipliers for IFFT modules in LACO-OFDM transmitter is 700. That is to say, the required number of multipliers for the IFFT modules in the LACO-OFDM transmitter is the same as that in a DCO-OFDM transmitter when they achieve the same spectral efficiency.

The number of multipliers used in Scheme 3 (single IFFT method) is evaluated and also tabulated in Table 4.2. It shows that the same number of multipliers (696) is used as the Scheme 2. Because in Scheme 2, these zero-valued inputs in the four IFFTs has been optimized to reduce its implementation cost. In Scheme 3, I successfully merge all the four IFFTs into one large IFFT, by extracting waveforms within single IFFT. Compared with Scheme 2, although Scheme 3 does not reduce the computational complexity, but this single IFFT technique does not need to optimize the four IFFTs individually, simplifying the implementation process and data-flow within the FPGA, which makes the implementation of LACO-OFDM transmitter is almost as the same as DCO-OFDM transmitter.

TABLE 4.2: Multiplier utilization of IFFT's implementation Scheme 1, 2, 3 for LACO-OFDM transmitter with four layers.

Scheme	Implementation Method	Number of Multipliers
1	Four IFFT	1040
2	Optimized four IFFT	696
3	Single IFFT	696

4.5.2   Transmitter DSP Implementation

Among all the three shemes, we have learned that the *middle-out* IFFT is the most hardware-efficient and simplest implementation method for LACO-OFDM. Therefore, *middle-out* IFFT was used in this experiment and all the DSP functions of the LACO-OFDM transmitter were implemented in a Virtex-6 FPGA.
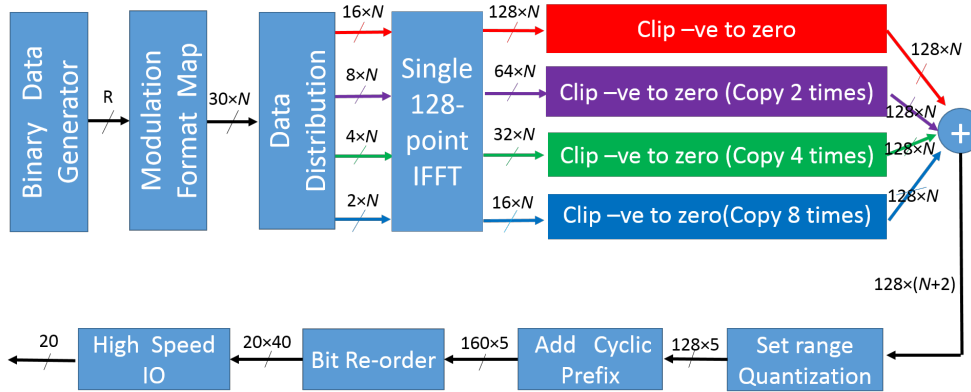
FIGURE 4.14: DSP functions with a *middle-out* 128-point IFFT. Four layers are used and the waveform of each layer is extracted within this 128-point IFFT. All the DSP functions are implemented in the FPGA.
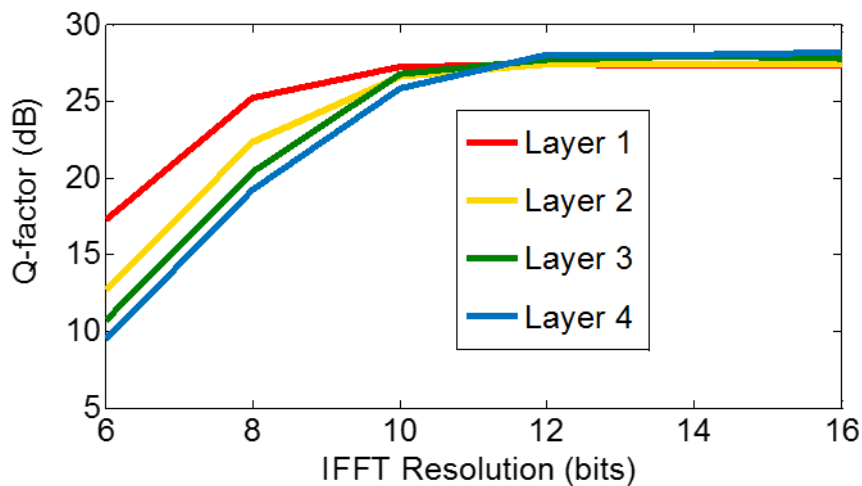
FIGURE 4.15: Simulated Q-factor versus IFFT resolution. The waveform of each layer is obtained in the ISE and transferred into MATLAB to be further processed.

The implemented DSP blocks are shown in Fig. 4.14. The test data and two training symbols were stored in the FPGA. Every clock cycle, R data bits were mapped to 30 symbols, each with N-bit resolution. R depends on the modulation format on all the subcarriers, with $R = 30 \times \log_2 M$ for M-QAM, so R=60 or

120 if QPSK or 16-QAM modulation is imposed on all the 30 data-carrying subcarriers. Afterwards, these 30 complex numbers, combined with their Hermitian counterparts, were distributed to four layers through a data distribution module.

The IFFT resolution N needs to be carefully considered as a compromise between computational accuracy and hardware resource utilization. The signals after the set-range and quantization modules were then used to analyze the Q-factor for different IFFT resolutions, and the results are shown in Fig. 4.15. This graph illustrates that a 12-bit IFFT resolution is sufficient to obtain the maximum Q-factor. A higher IFFT resolution cannot increase the Q-factor anymore because at this stage it was mainly limited by the DAC resolution. Therefore, N=12 bits was used in the FPGA implementation. Each layer generated its own outputs within a *middle-out* fully-streaming 128-point IFFT with 12-bit resolution. The outputs from each layer were then clipped to remove all negative values before they were duplicated to generate the 128 12-bit real outputs individually.
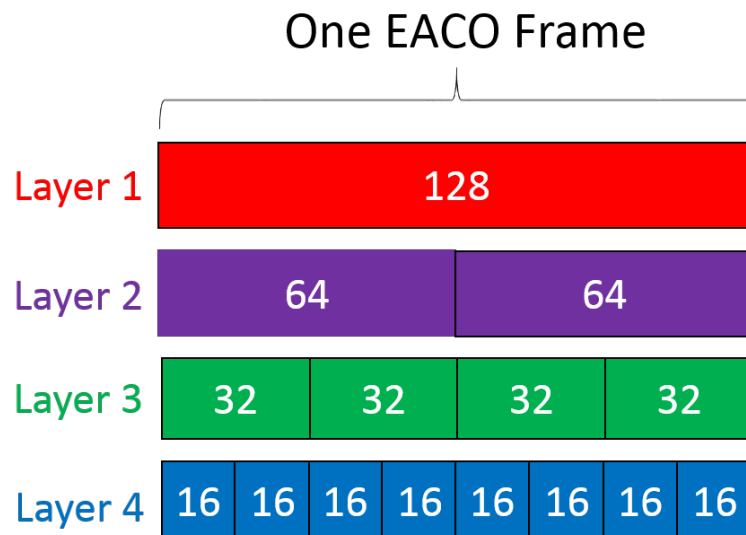
FIGURE 4.16: One LACO-OFDM frame if four layer and one 128-point IFFT is used. The waveforms in highers layers are periodic and can be generated using smaller IFFT sizes and then repeated.

In addition to multipliers, the addition operations also require large amounts of logic resouces in the implementation. Different to the the DCO-OFDM transmitter, four 128 12-bit words from four layers need to be added together, which will increase the number of adders by 384 (=128×3). However, we can reduce this number by taking advantage of the cyclic outputs in Layer 2, 3, and 4. One LACO-OFDM frame is illustrated in Fig. 4.16, showing that each layer outputs are streaming in parallel in the time domain. The waveforms in the higher layers are periodic and the cycle is shorter for higher layers. Therefore, the adding
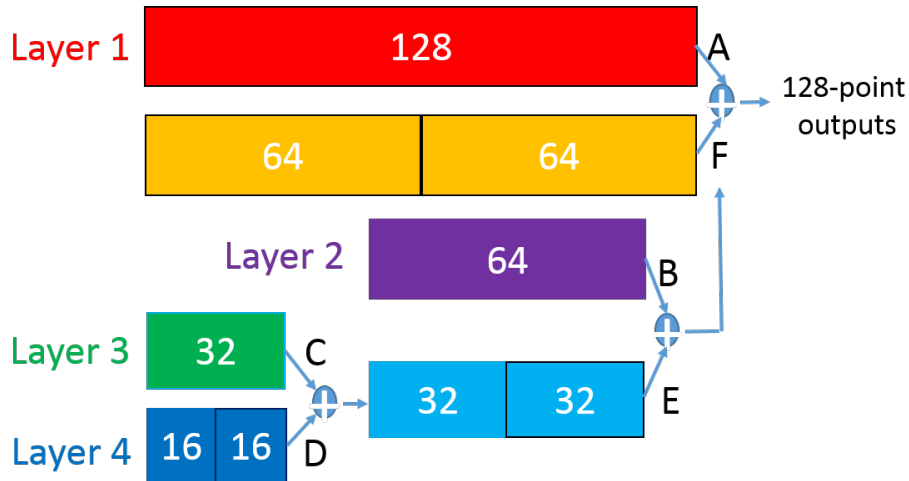
FIGURE 4.17: Four layers adding procedure by taking advantage of the waveform periodicity in higher layers to reduce the number of adders.

procedure of four layers can be simplified by reducing the computational redundancy as shown in Fig. 4.17. Firstly the 32-point output C and D from Layer 3 and 4 were combined and copied to form the 64-point output E. The length of 32 is selected according to the cycle of Layer 3. All the following addition procedure is performed similarly. After the addition of Layer 3 and 4, Then E was used to add a 64-point output B from Layer 2 and the results were repeated to give the 128-point output F. Finally, F and the 128-point output A from Layer 1 were added together to form one LACO-OFDM frame. The whole adding process consumed 224 (=32+64+128) adders. Furthermore, the adders that are used to get the top-half outputs in the last stage of IFFT butterfly, such as x(0-3) shown in Fig. 4.10, can be eliminated in all the four IFFT modules, saving 120 (=64+32+16+8) adders. Therefore, compared with DCO-OFDM transmitter, LACO-OFDM transmitter requires only 104 (=224-120) more adders in the implementation, which is a very small increase.

After being added together, 128 14-bit words were transformed into 128 5-bit words through the set-range and quantization module. Then a 32-sample cyclic prefix (CP) was pre-pended to every OFDM symbol, producing 160 5-bit words which were distributed to 20 high-speed transmitters of the FPGA, representing four 5-bit parallel data streams to feed the MICRAM DAC.

TABLE 4.3: Implementation cost for QPSK and 16-QAM.

Modulation Formats	Registers	LUTs	DSP48E1s
QPSK	11%	22%	79%
16-QAM	13%	25%	82%

As shown in Table. 4.3, of the available resources on the Vertix-6 (XC6VLX240T) FPGA , the design used 11% of the slice registers (35405), 22% of the slice LUTs (33479) and 79% of the DSP48E1s (612) when QPSK is modulated on the OFDM subcarriers. When 16-QAM is used on the OFDM subcarriers, the design used 13% of the slice registers (41830), 25% of the slice LUTs (38035) and 82% of the DSP48E1s (630). The slight increase of logic resource utilization comes from the 16-QAM modulation format. In the implementation, apart from the multipliers used by IFFT modules, another 128 multipliers were required by the set-range and quantization module. The output signal after set-range and quantization module has the form as

$$
y(n) = \begin{cases} \alpha x(n) & \alpha x(n) \leq B \\ B & \alpha x(n) > B, \end{cases} \tag{4.7}
$$

where $x(n)$ and $y(n)$ are the input and output signals of the set-range and quantization module. B was the clipping threshold value and was set to $2^q - 1$ for a q-bit DAC. In this experiment, B was 31 as a 5-bit DAC was used. A positive-valued scaling factor α achieved a trade-off between the set-range clipping distortion and quantization error. Theoretically 824 (=696+128) multipliers had to be implemented, but not the entire 768 (DSP48E1s) multipliers from Virtex-6 FPGA were used in the implementation. Because that the implementation process was compiled automatically by the Xilinx ISE software, parts of the LUT slices were allocated to do the multiplications instead of using DSP slices.

4.5.3   Experimental Setup

The experiment setup of LACO-OFDM transmitter is shown in Fig. 4.18 and 4.19. A 156.25-MHz clock generated by the DAC provided a clock to the FPGA, which was used to control all the DSP modules in the FPGA and synchronize the FPGA and DAC. The DAC and FPGA channels were connected via 20 pairs of coaxial cables for LVDS. The FPGA's high-speed transmitters were programmed to be 6.25 Gbaud and then these channels were multiplexed every four channels in the DAC, which has a sampling rate of 25 GSample/s when clocked at 12.5 GHz, to produce a 25 Gsample/s 5-bit resolution analog output. Actually, this MICRAM DAC had a resolution of 6 bits, so full operation requires 24 high-speed transmitter channels from the FPGA. However, as there were only 20 high-speed transmitters available on our FPGA evaluation board (ML623), the four inputs corresponding to the least significant bit of DAC were connected to logic zero. The picture of the transmitter setup (connection between FPGA and DAC) is shown in Fig. 4.19.
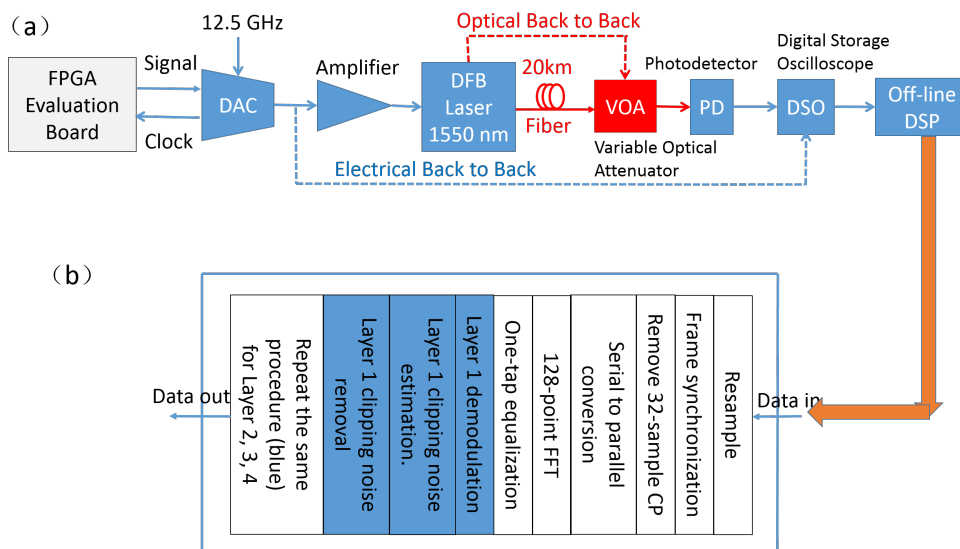
FIGURE 4.18: LACO-OFDM optical transmission link setup diagrams. The LACO-OFDM signal is generated in real-time using FPGA. The signal is processed offline in the receiver using MATLAB: (a) block diagrams (b) Offline DSP algorithms.

The peak-to-peak voltage (Vpp) of the DAC analog output signal was 500 mV. The signal was fed through 18-dB attenuators and a DC block, followed by a 24-dB gain 40-GHz linear electrical amplifier (SHF-807). The resulting 1-volt (p-p) output was connected to a distributed feedback (DFB) laser, which was biased at 33 mA. Its threshold current was 13 mA. After transmission over a 20-km span
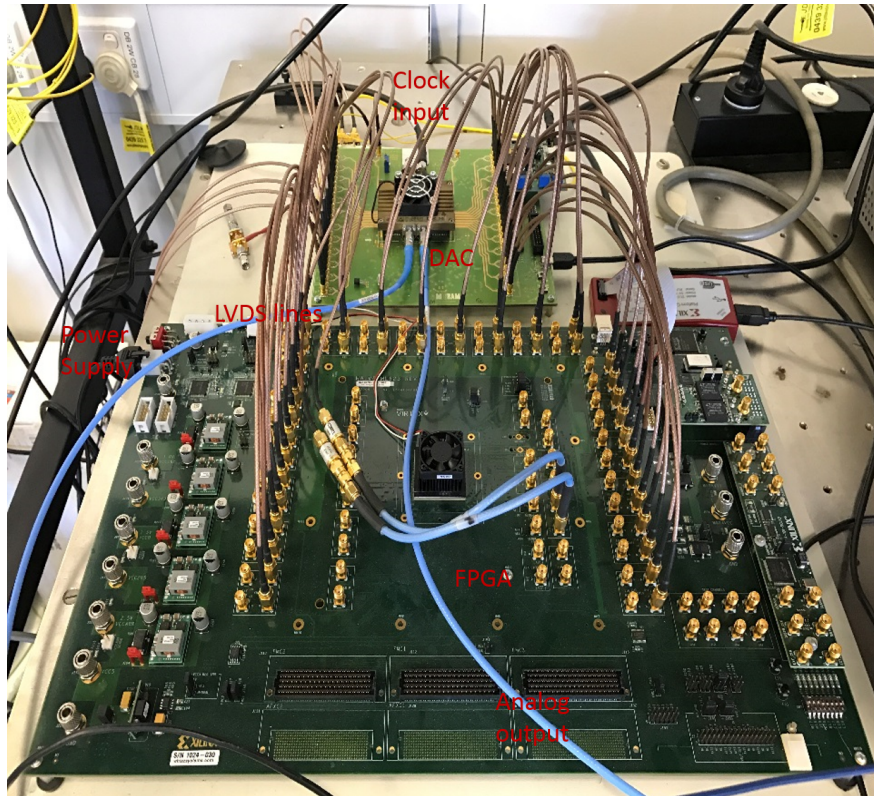
FIGURE 4.19: The LACO-OFDM transmitter setup (connection between FPGA and DAC). One external signal generator provides a clock for the DAC. 20 LVDS channels are connected between FPGA and DAC via SMA cables.

of SSMF, a variable optical attenuator (VOA) was used to adjust the output optical power, followed by a 16-GHz photodetector (DSC-40S) to convert optical signals to electrical signals, which were then sampled by a real-time Digital Storage Oscilloscope (DSO-X92804A) at 80-GS/s. Finally, the captured samples were analyzed by offline DSP in MATLAB. The offline DSP algorithm is illustrated in Fig. 4.18(b), and is the same as that used in typical offline OFDM receivers including frame synchronization, CP removal, serial to parallel conversion and one-tap equalization; however, an iterative demodulation algorithm was used to decode the data layer by layer to ensure that the decoding process was not influenced by the clipping distortion. Some key parameters in the entire transmission link are summarized in Table 4.4.

TABLE 4.4: Key parameters in the experimental setup for LACO-OFDM.

Parameter	Value
Modulation format	QPSK/16-QAM
Oversampling rate	2
Number of layers	4
IFFT size	128-/64-/32-/16-points
IFFT resolution	12 bits
CP length	32 samples
Data-carrying subcarriers	30 (excluding DC and 16th)
FPGA fabric clock	156.25 MHz
DAC sampling rate	25 GSa/s
DAC output voltage	500 mV
DAC resolution	5 bits
Net bit rate	9.375 Gb/s for QPSK or 18.75 Gb/s for 16-QAM
DFB laser wavelength	1550 nm
DFB laser bias current	33 mA
Amplifier bandwidth	40 GHz
Oscilloscope sampling rate	80 GSa/s
Photodetector bandwidth	16 GHz
Transmission distance	20 km for QPSK or 10 km for 16-QAM

4.5.4 Experimental Results

4.5.4.1 QPSK Link

Since 30 subcarriers are used to carry QPSK mapped data, the overall net data rate for this LACO-OFDM transmitter is 9.375 Gb/s ($2 \times 25 \times 30/160$), neglecting an overhead of two training symbols. Firstly, the Q-factor performance for electrical back-to-back configuration (see Fig. 4.18) was measured by connecting the DAC output directly to a DSO. The captured samples were analyzed by offline DSP in MATLAB and the results are shown in Fig. 4.20. As the Q-factors of adjacent-index subcarriers in different layers are very similar, we can conclude that the iterative algorithm in the receiver substantially cancels the clipping distortion.
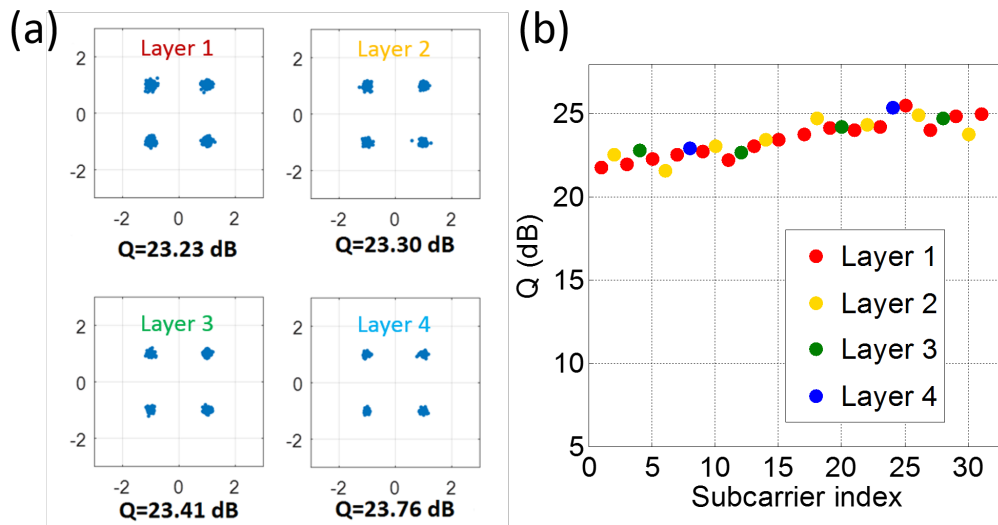
FIGURE 4.20: Q-factors of electrical back-to-back for signal generation using a FPGA and 5-bit MCIRAM DAC.

Offline LACO-OFDM signal generation was also conducted using MATLAB and fed to a Tektronix AWG7102 arbitrary waveform generator (AWG). All the parameters were the same as the FPGA-based signal generation. Its Q-factors of electrical back-to-back were measured and are shown in Fig. 4.21. A 5-dB Q-factor improvement is seen compared with signal generation using FPGA and MICRAM DAC. Since increasing the IFFT resolution did not improve the signal quality, as shown in Fig. 4.15, we believe that the reason for this 5-dB Q-factor difference is that the DAC in the Tektronix AWG has a resolution of 8 bits, which is 3-bits higher than our use of MICRAM DAC.
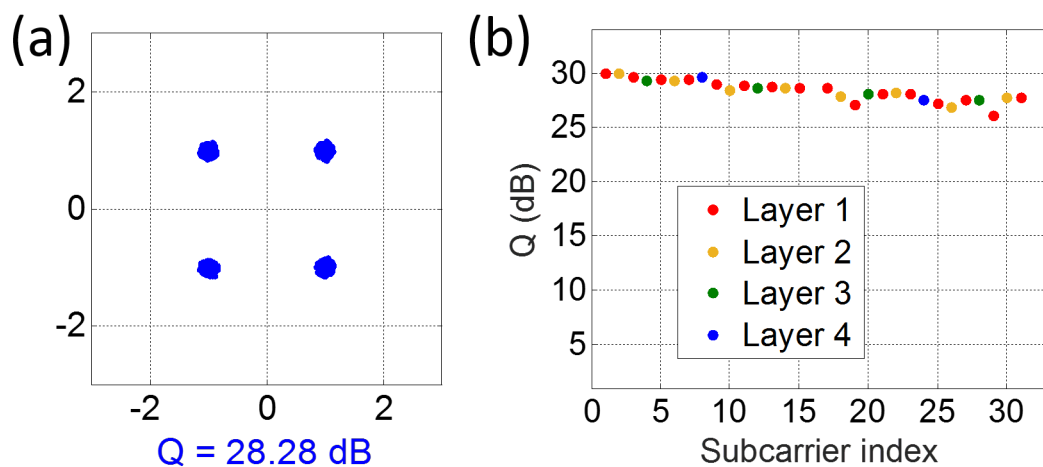
FIGURE 4.21: Q-factors of electrical back-to-back for signal generation using a Tektronix AWG7102.

The back-to-back optical link was then evaluated by directly connecting the

laser output to a VOA. With no optical attenuation, the optical power received by photodetector is 3.32 dBm and the Q-factor of optical back-to-back is 19.61 dB, as shown in Fig. 4.22; a reduction of around 4 dB compared with electrical back-to-back. More specifically, the Q-factors for the low-frequency subcarriers are just 1-dB less than that for electrical back-to-back. We assume that the penalty mainly comes from the laser and photodetector. A 5-dB penalty for the highest-frequency subcarriers, compared with the Q-factor performance of electrical back-to-back, is due to the limitation of the laser's bandwidth. The normalized power spectra versus frequency for optical back-to-back is shown in Fig. 4.23. The bandwidth of this LACO-OFDM signal is 6.25 GHz. We can see that the powers of subcarriers around 6 GHz are a little higher than the lower-index subcarriers due to the relaxation oscillation peak of semiconductor laser. The spectral power above 6.25 GHz is due to the clipping when generating the ACO-OFDM layers, in accordance to the simulation results in [66].
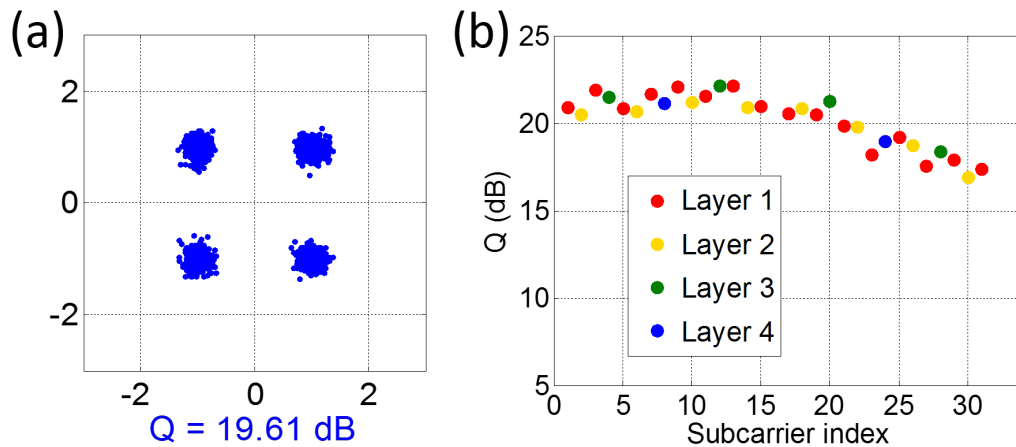
FIGURE 4.22: Q-factors of optical back-to-back.

To investigate the transmission performance considering only the transmission link loss, we adjusted the VOA to attenuate the optical signal and measured the corresponding Q-factors. The results are shown in Fig. 4.24. When the attenuation is set to 4 dB, the Q-factor is about 19 dB, a reduction of only 0.6 dB. For lower attenuations (1-7 dB), the Q-factor drops very slowly, because the noise power from the transmission link is still very small compared with signal power. When the attenuation is between 8 dB and 12 dB, the transmission link noise reduces the Q-factor by 2 dB for every 1-dB optical power attenuation. At this stage, all the clipping distortion still can be cancelled as the Q-factors for all the four layers are very similar. Signal degradation in higher layers occurs when optical power is attenuated more than 12 dB. The 7% FEC limits corresponding to bit-error-ratio (BER) of 3.8×10^{-3} is plotted in Fig. 4.24. The receiver sensitivity
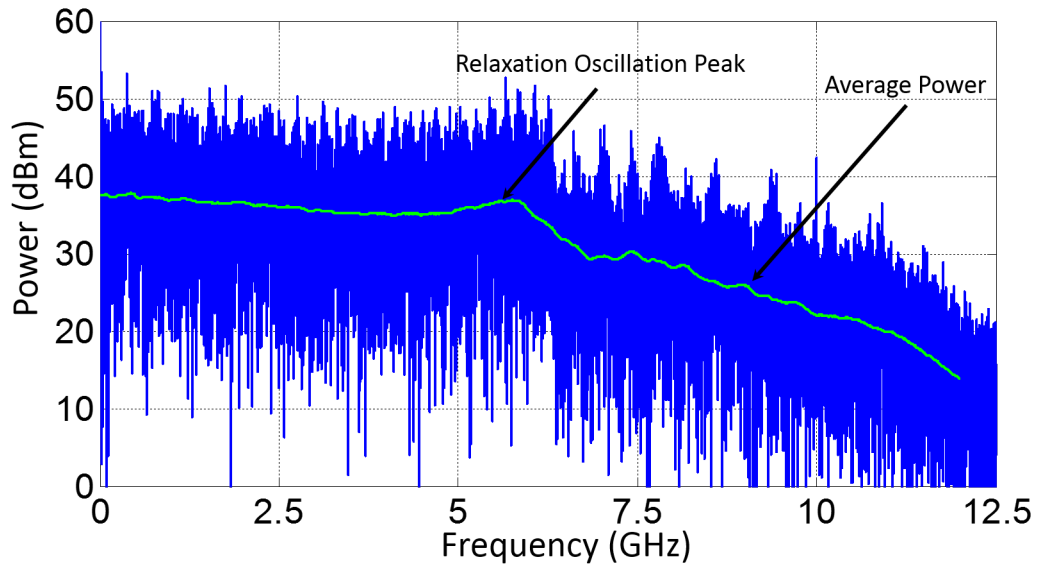
FIGURE 4.23: Normalized power versus frequency after the receiver PD for optical back-to-back.

of PD is -9.68 dBm (=3.32 dBm − 13 dB) at a BER of 3.8×10^{-3}. When the Q-factor hits this 7% FEC limits, it means that the iterative algorithm in the receiver cannot correctly decode the data in the first layer. These decoded errors from the lower layers will be passed to higher layers, leading to more decoding errors in higher layers, which will significantly increase the overall BER because LACO-OFDM requires an iterative receiver algorithm, which relies on the previous layer being correctly decoded to remove clipping distortions.
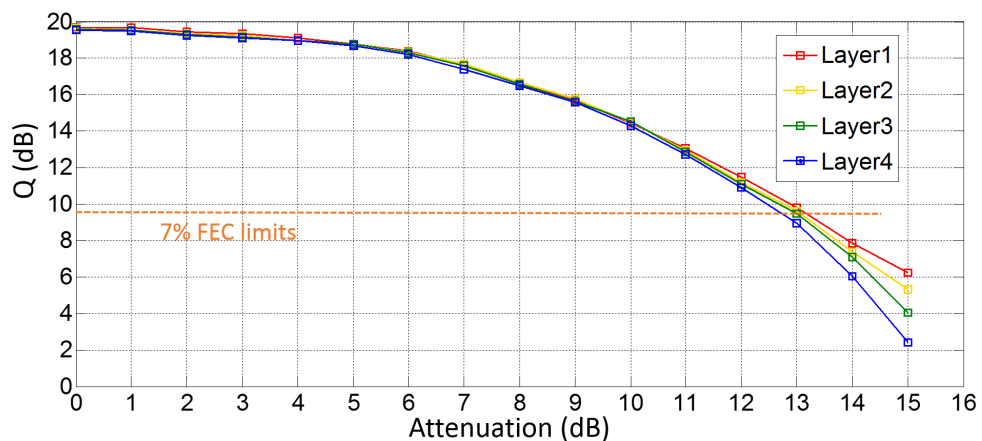
FIGURE 4.24: Q-factors for all the four layers versus optical attenuation.

Finally, the attenuation of VOA was set to zero again when the Q-factor was evaluated after transmission over 20-km SSMF. Without using any optical amplifier, the Q-factor calculated from the average BER is still above 14 dB as shown in

Fig. 4.25. The optical power received by photodetector is -1.96 dBm, so the total
link loss is around 5.3 dB including around 1-dB loss from optical fiber connectors
and around 4-dB loss for the 20-km SSMF. The Q-factors for the lower-index sub-
carriers after transmission over 20-km SSMF is reduced around 1 dB compared
with optical back-to-back, which is in accordance with the reduction of Q-factor
corresponding to the 5-dB attenuation shown in Fig. 4.24. Note, after transmis-
sion over 20-km S-SMF, the higher-index subcarriers suffer a larger penalty of 10
dB, compared with the low-frequency subcarriers.
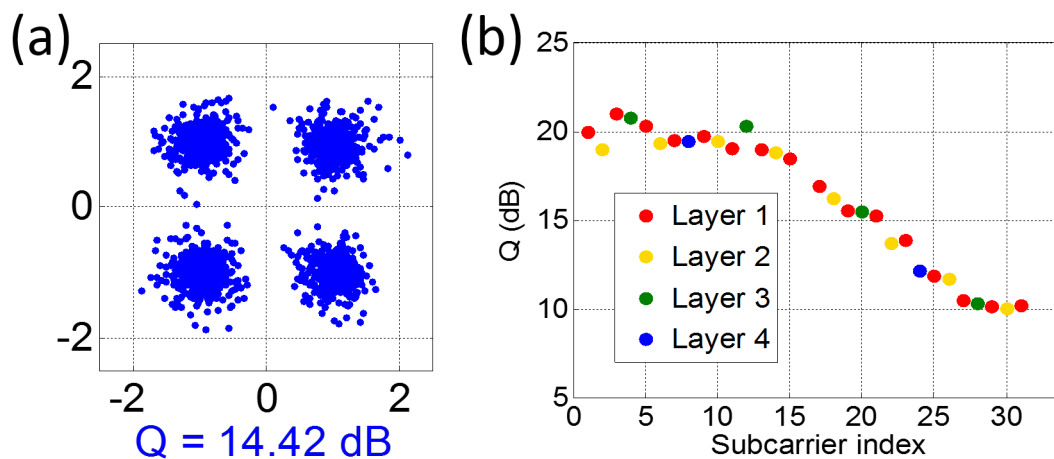
FIGURE 4.25: Q-factors after 20-km transmission.
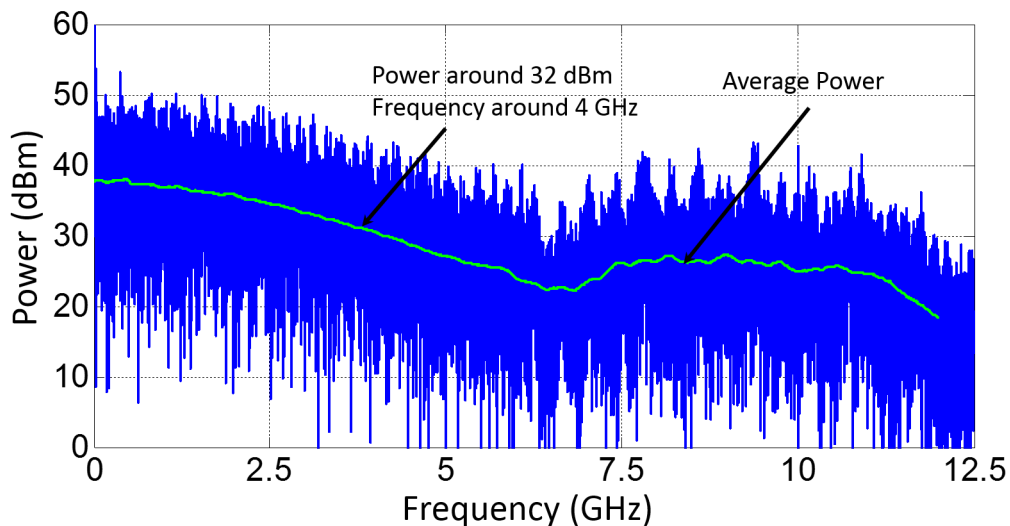
FIGURE 4.26: Normalized power versus frequency after the receiver
PD for 20-km transmission.

The signal power spectra after 20-km transmission are shown in Fig. 4.26. It
shows that the subcarriers above 2 GHz suffer from reduced powers. The signal
power in the 4 GHz drops around 5 dB compared with the near DC frequency,

which explains why the subcarriers adjacent to the 20th subcarrier suffer a 5-dB penalty compared with the lower-index subcarriers as was shown in Fig. 4.25(b).

4.5.4.2 16-QAM Link

In the previsous section, we have shown that the Q-factor was reduced to 14.42 dB after transmission over 20-km SSMF. It will lead to large decoding errors for 16-QAM and these errors will propogate among different layers, increasing the overall BER significantly. Therefore, the transmssion distance was shortened to 10 km for 16-QAM link in our real-time experimental demonstration. Because the subcarriers were modulated with 16-QAM, the data rate was doubled to be 18.75 Gb/s. The block diagrams of this experimental setup is shown in Fig. 4.27, which is almost the same as Fig. 4.18, except the length of fiber.
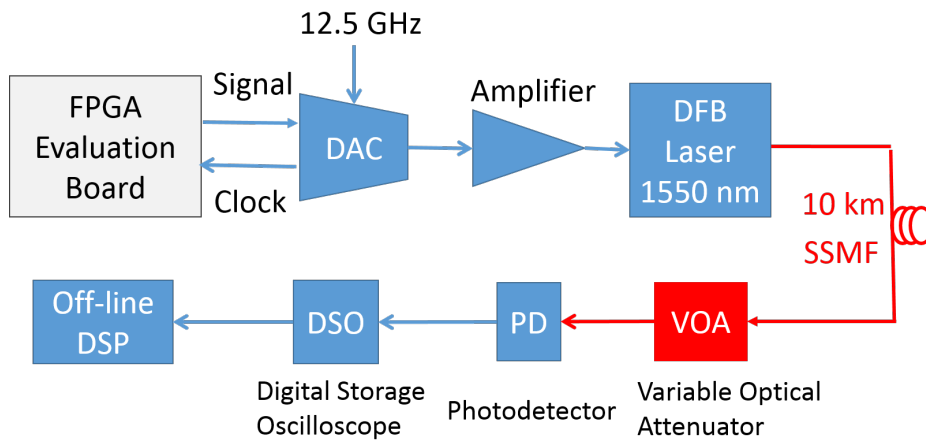
FIGURE 4.27: block diagrams of LACO-OFDM optical transmission link setup for 16-QAM. The setup is similar as the Fig. 4.18(a) except that the fiber length is 10 km in this experiment
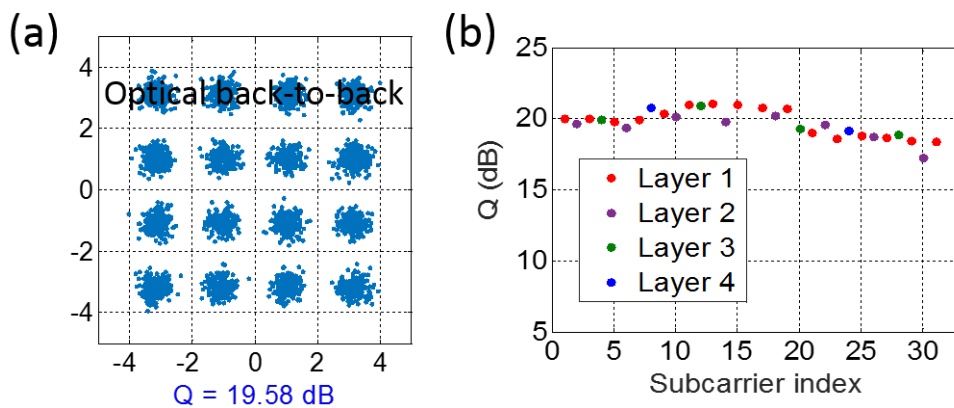
FIGURE 4.28: Q-factor for optical back-to-back for 16-QAM.
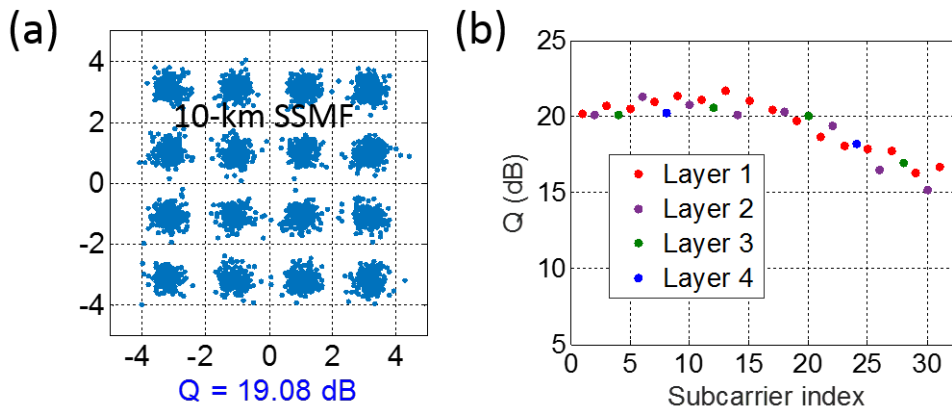
FIGURE 4.29: Q-factor after transmission over 10-km SSMF for 16-QAM.

Firstly, the Q-factor performance for a back-to-back optical link was measured. As shown in Fig. 4.28, the average Q-factor of optical back-to-back is 19.58 dB, which is almost the same with QPSK transmission link. Besides, the Q-factors of adjacent-index subcarriers in different layers are still very similar, we conclude that the iterative algorithm in the receiver substantially cancels the clipping distortion although 16-QAM is modulated on the OFDM subcarriers. Finally, the Q-factor was evaluated after transmission over a 10-km SSMF. Without using optical amplifiers, the Q-factor is still above 19 dB (Q = 16.54 corresponding to a BER of 3.8×10^{-3} for 16QAM) and there is no error propagation to higher layers, as shown in Fig. 4.29. However, the higher-index subcarriers still suffer a larger penalty, compared with the low-frequency subcarriers, probably because of the interaction of laser chirp and fiber dispersion.

4.6 Conclusions

In this chapter, the simulation results and offline experimental demonstration for LACO-OFDM are introduced firstly, which confirm that LACO-OFDM is more power-effcient, in comparison with DCO-OFDM, while they achieve similar spectral efficiency. Then, an FPGA-based LACO-OFDM transmitter with a net data rate up to 18.75 Gb/s has been experimentally demonstrated in a DML-based short-haul fiber-optic link. Although the LACO-OFDM transmitter requires more-complex DSP (more IFFTs) compared with DCO-OFDM transmitters, its implementation requires almost the same amount of logic resources as that for DCO-OFDM by using a *middle-out* IFFT. Because our implementation method does not

change the regularity of traditional IFFT butterfly flow, most of the implementation strategies used for traditional IFFT can also be used in our LACO-OFDM implementation. The same implementation method can also be used in the clipping noise regeneration modules in the receiver. By using offline DSP in the receiver, this LACO-OFDM signal has been successfully transmitted over 20-km SSMF for QPSK link or 10-km SSMF for 16-QAM link without using any optical amplifiers.

Chapter 5

Augmented Spectral Efficiency DMT

5.1   Introduction

In short-haul transmission research, OFDM is often called discrete multi-tone (DMT). As we have discussed, the power efficiency of DCO-OFDM needs to be improved by lowering or eliminating the DC bias. The two well-known techniques are asymmetrically clipped optical OFDM (ACO-OFDM) [55] and pulse amplitude-modulated optical DMT (PAM-DMT) [56]. For both of these schemes, unipolar outputs are achieved by clipping the negative samples to be zero-valued. However, these two schemes cannot use the even-valued subcarrier slots (ACO-OFDM) or the inphase components (PAM-DMT); thus, they sacrifice half of the spectral efficiency. Therefore, compared with DCO-OFDM at the same data rate, they require either higher-order modulation formats, or electrical and optical devices with doubled bandwidths.

In Chapter 4, an efficient real-time LACO-OFDM transmitter has been experimentally demonstrated, which improves the spectral efficiency of ACO-OFDM towards that of DCO-OFDM, by enabling the even-frequency subcarriers to be used. Similarly, augmented spectral efficiency DMT (ASE-DMT) uses layering applied to PAM-DMT, allowing the unused inphase components to be modulated in additional layers [68]. As the clipping procedure is also performed in all the layers for ASE-DMT as in LACO-OFDM, it still maintains a power advantage over DCO-OFDM without halving the spectral efficiency. However, ASE-DMT shares the same problem with LACO-OFDM, in that it requires additional FFT's for the extra layers.

In this chapter, a novel and efficient method of generating ASE-DMT signals using only one IFFT is introduced. Through carefully mapping the layers to the inputs of one IFFT and by extracting the higher layer's waveforms from within the core of a single IFFT, separate outputs for each layer can be obtained, to be clipped separately before combination. This saves approximately 30% logic resources. Using this method, a real-time ASE-DMT transmitter was implemented

in a Virtex-6 FPGA (XC6VLX240T). Its net output data rate is up to 9.2 Gb/s for PAM2-encoded ASE-DMT or 18.4 Gb/s for PAM4-encoded ASE-DMT. Firstly, PAM2 is encoded on the ASE-DMT subcarriers and its transmission performance is evaluated. By upgrading the modulation format to PAM4, a more detailed transmission performance evaluation over different SSMF fiber length is demonstrated. A Q-factor of >19 dB is obtained for an optical back-to-back. Using a 1550-nm DML, the signal can be successfully transmitted over 20-km SSMF for PAM2-encoded transmission link or 10-km SSMF for PAM4-encoded transmission link.

5.2 ASE-DMT Algorithm

The transmitter block diagrams of ASE-DMT is shown in Fig. 5.1. Each layer needs its own IFFT and clipping module. The data-carrying subcarrier allocation and clipping distortion distribution is shown in Fig. 5.2. Only four layers are used in this illustration and more layers can be used until the inphase and quadrature components of all the subcarriers are encoded to give the same spectral efficiency of DCO-OFDM if necessary.

   The first layer of ASE-DMT, which is the same as PAM-DMT, carries pulse amplitude-modulated signal on the quadrature components of all the subcarriers. In a standard QAM modulated DCO-OFDM transmitter, one IFFT module is used to generate and superpose all the subcarriers digitally. For a $2N$-point IFFT, the OFDM time domain signals over one symbol can be written as

$$x(n) = \frac{1}{2N} \sum_{k=0}^{2N-1} X(k) \exp(\frac{j2\pi kn}{2N}), n = 0, 1, ..., 2N - 1 \qquad (5.1)$$
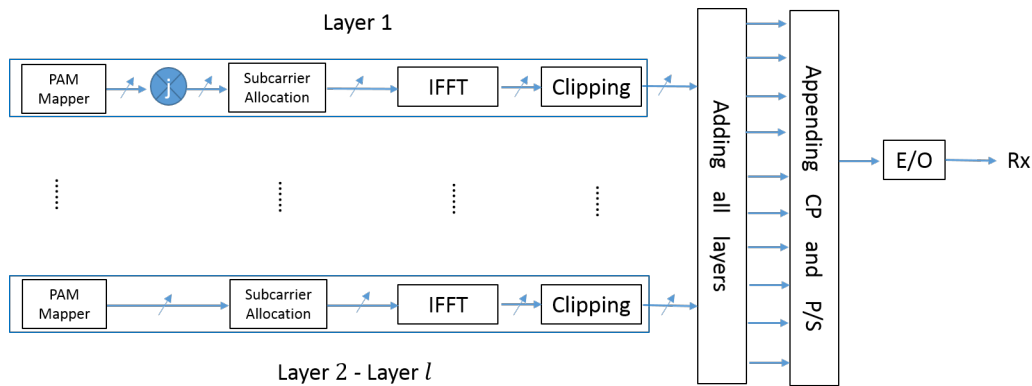
FIGURE 5.1: The functional blocks in an ASE-DMT transmitter. l layers are used. Each layer needs one IFFT and clipping module.
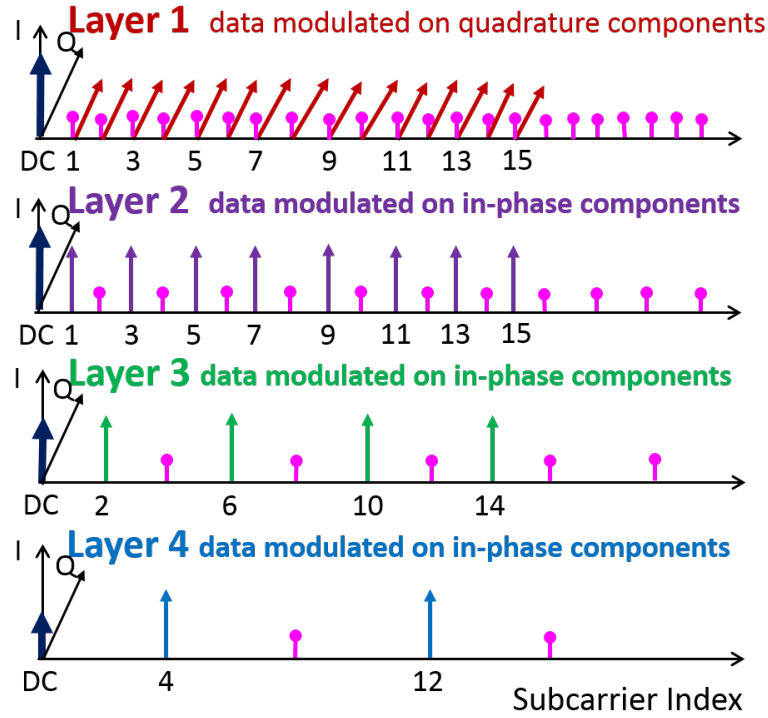
FIGURE 5.2: Data-carrying subcarrier allocation and clipping distortion distribution of layers in an ASE-DMT transmitter. Note the I and Q axis are in orthogonal.

where $X(k) = D(k) + jE(k)(k = 0, 1, ..., 2N - 1)$ are the QAM-modulated inputs to the IFFT module. Hermitian symmetry $(X(2N - k) = X^*(k), k = 1, 2, ..., 2N - 1)$ with $(X(0) = X(N) = 0)$ is usually imposed on the IFFT inputs. In PAM-DMT, only the quadrature components (imaginary parts) of all the subcarriers are used to carry information. Therefore, the inphase components of $X(k)$ are set to be zero-valued and only the quadrature components are pulse-amplitude modulated, resulting in $X(k) = jE(k)(k = 0, 1, ..., 2N - 1)$, where only $X(k) = jE(k)(k = 0, 1, ..., N - 1)$ are independent. Therefore, Equation 5.1 can be simplified to

$$
\begin{aligned}
x(n) &= \frac{1}{2N} \sum_{k=0}^{2N-1} jE(k) \exp(\frac{j2\pi kn}{2N}) \\
&= \frac{1}{2N} \sum_{k=0}^{2N-1} [jE(k) \cos(\frac{2\pi kn}{2N}) - E(k) \sin(\frac{2\pi kn}{2N})] \\
&= \frac{-2}{2N} \sum_{k=0}^{N-1} E(k) \sin(\frac{2\pi kn}{2N}), n = 0, 1, ..., 2N - 1
\end{aligned}
\tag{5.2}
$$

As Equation 5.2 only has $sin(2\pi kn/2N)$ terms, the waveform of PAM-DMT is

antisymmetrical ($x(n) = x(2N - n), n = 1, 2, ..., N - 1$), which is similar to ACO-OFDM. Therefore, the negative values of PAM-DMT waveform can be clipped to be zero-valued without losing any information because the same information has been kept in the positive parts of the waveform. In fact, the clipping distortion falls only on the inphase components (real parts) of all the subcarriers [56], as the first layer shown in Fig. 5.2. Hence, the inphase components of all the subcarriers are wasted. To enable these inphase components to carry data, ASE-DMT adds further layers on-top of this distortion.

As shown in Fig. 5.2, the higher layers, L = (2, 3, 4), carry pulse-amplitude-modulated subcarriers on the inphase components of subcarriers that have frequency indices $2^{(L-1)} \times (2n + 1)$, where n = (0, 1, 2, 3, . . .). Clipping these produces distortion that also falls on the inphase components and is indicated by the pink. In the meantime, its clipping distortion only falls on the subcarriers that have frequency indices $2n \times 2^{(L-2)}$, where n = (1, 2, 3, . . .). Therefore, the clipping distortion from higher layer does not contaminate the data-carrying components (inphase or quadrature) in lower layers. To build the ASE-DMT signal, each layer generates its own outputs using a separate IFFT; then the negative values of each layer's waveform are clipped to become zero-valued. Finally, a unipolar signal output is obtained by adding all the already-clipped waveforms of the four layers. The DC bias is avoided because each layer's waveform has already been clipped to be non-negative.
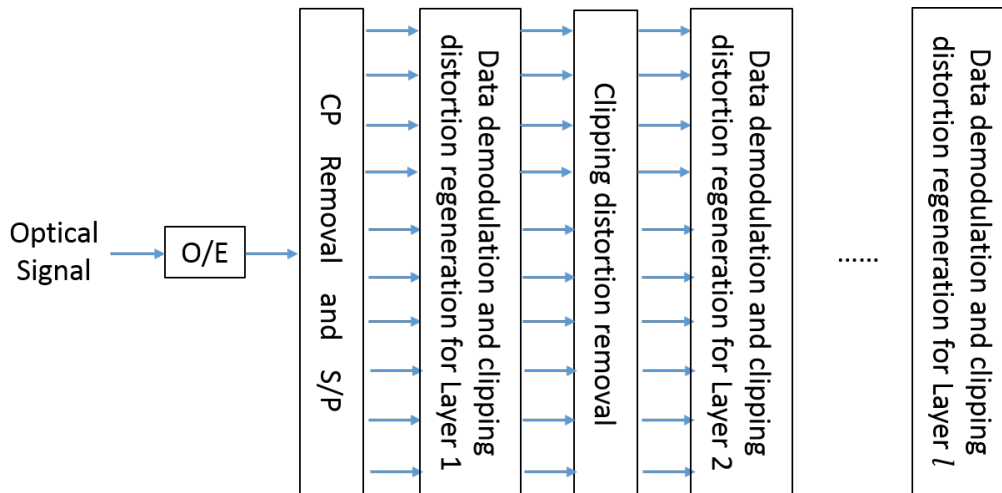
FIGURE 5.3: ASE-DMT receiver block diagrams.

The block diagrams for ASE-DMT receiver are shown in Fig. 5.3. After converting the optical signal to the electrical signals, CP removal and serial to parallel conversion are preformed, which is the same as the regular OFDM receivers. An
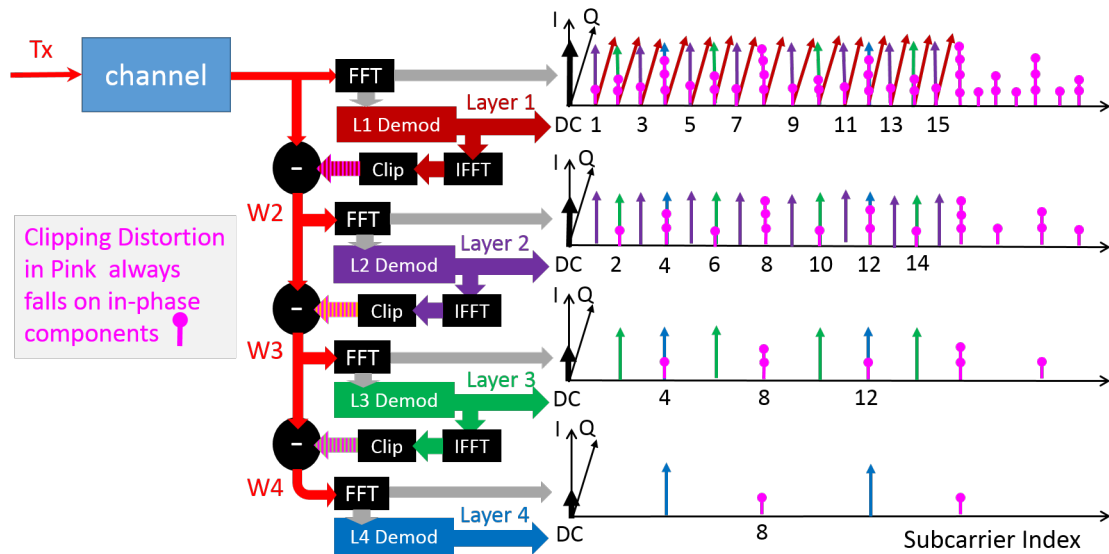
FIGURE 5.4: Iterative receiver processing and intermediate spectra
in an ASE-DMT transceiver.

iterative algorithm is used to decode the data layer-by-layer in the ASE-DMT re-
ceiver. In order to achieve clipping distortion free before decoding the data in
higher layers, the data in the lower layers must be recovered; then these data
are used to regenerate its clipping distortion, which are removed from the wave-
form next. This is very similar to the concept of the iterative receiver used in
the LACO-OFDM receiver. The intermediate spectra among the layer by layer
decoding is shown in Fig. 5.4. The clipping distortion from all the layers only
falls on the inphase components. Therefore, Layer 1 (red) is free of clipping dis-
tortion, and so is decoded first, using a FFT and a slicer to recover the encoded
data. This recovered data is then used to regenerate a facsimile of Layer 1's trans-
mitted waveform using an IFFT and a clipper, which is then subtracted from the
received waveform, as indicated in W2, to reveal the inphase components of the
second layer. Now the inphase components (purple) in Layer 2 become free of
clipping distortion because the remained clipping distortion is generated by >1
Layers and orthogonal to the data-carrying components of Layer 2. So the data
in Layer 2 can be decoded next and then the recovered data is used to regenerate
a facsimile of Layer 2's transmitted waveform to remove the clipping distortion
falling on data carrying subcarriers in Layer 3. The same procedure is repeated
layer-by-layer until the data in all the layers are recovered.

5.3   ASE-DMT Transmitter Implementation

5.3.1   Computation of Real-valued FFT

In order to improve the spectral efficiency of ASE-DMT, more layers are required. However, as one IFFT module is required in every layer, several IFFTs will significantly increase the overall computational complexity. It has been shown that only one IFFT has occupied most of the logic resource usage in the DCO-OFDM transmitter [155]. Therefore, the implementation of ASE-DMT transmitter needs to be simplified. In the different layer of ASE-DMT transmitter, only the inphase components (real parts) or the quadrature components (imaginary parts) of the IFFT's inputs are used. Therefore, real-valued FFT algorithm can be used in the implementation of ASE-DMT transmitter to reduce its computational complexity.

One straightforward way to compute the real-valued FFT is to use the complex-valued FFT directly by expanding the sequence with a zero imaginary part to obtain complex inputs. Apparently, it is not efficient due to the same number of complex multiplications required as the complex-valued FFT with the same length.

The second technique can compute two real-valued sequences simultaneously by using only one complex-valued FFT [169], [188]. In [189], Brigham showed that the two N-point real-valued FFTs could be achieved using one N-point complex valued FFT with $2N - 4$ extra additions to separate the two real-valued FFT. It's supposed that $x(n)$ and $y(n)$ are real-valued, so the FFT of $z(n) = x(n) + jy(n)$ is

$$
\begin{aligned}
FFT[z(n)] &= Z(K) \\
&= Z_r(K) + jZ_i(K) \\
&= FFT[x(n) + jy(n)] \\
&= \{X_r(K) - Y_i(K)\} + j\{X_i(K) + Y_r(K)\}
\end{aligned}
\tag{5.3}
$$

where subscripts r and i denote real and imaginary parts respectively. As both the $x(n)$ and $y(n)$ are real-valued, so $X(K)$ has an even real part and an odd imaginary part. Therefore, for $k = 0, 1, ..., N/2$,

$$
Z(N - K) = \{X_r(K) + Y_i(K)\} - j\{X_i(K) - Y_r(K)\}
\tag{5.4}
$$

so,

$$FFT[x(n)] = X_r(K) + jX_i(K)$$
$$= \frac{1}{2}\{Z_r(K) + Z_r(N-K)\} + j\frac{1}{2}\{Z_i(K) - Z_i(N-K)\} \quad (5.5)$$

$$FFT[y(n)] = Y_r(K) + jY_i(K)$$
$$= \frac{1}{2}\{Z_i(K) + Z_i(N-K)\} + j\frac{1}{2}\{Z_r(N-K) - Z_r(K)\} \quad (5.6)$$

5.3.2 Efficient IFFT Implementation

In IMDD based optical OFDM communication system, only the inphase compo-
nents of IFFT's output are used to drive the intensity of the layer because Hermi-
tian symmetrical inputs of the IFFT force its quadrature components of output to
be zero-valued. Therefore, it can be regarded as a real-valued FFT. As we have
discussed in the previous sections, one complex FFT can be used to compute two
real-valued FFTs [67], [169]. However, in order to achieve a high spectral effi-
ciency, ASE-DMT requires >= 3 layers. Therefore, it cannot be used to generate
the ASE-DMT signal directly. In this section, the generation of the ASE-DMT
signal using only one complexed-valued FFT will be discussed.

In a standard QAM DCO-OFDM transmitter, one IFFT module is used to gen-
erate and superpose all the subcarriers digitally. For a $2N$-point IFFT, the OFDM
time domain signals over one symbol can be written as

$$x(n) = \frac{1}{2N}\sum_{k=0}^{2N-1} X(k)\exp(\frac{j2\pi kn}{2N}), n = 0, 1, ..., 2N-1 \quad (5.7)$$

where $X(k) = D(k) + jE(k)(k = 0, 1, ..., 2N - 1)$ are the QAM-modulated inputs
to the IFFT module. Hermitian symmetry $(X(2N-k) = X^*(k), k = 1, 2, ..., 2N-1)$
with $(X(0) = X(N) = 0)$ is usually imposed on the IFFT inputs [190]. Therefore,
Equation 5.7 can be simplified to

$$x(n) = \frac{2}{2N}\sum_{k=0}^{N-1}[D(k)\cos(\frac{2\pi kn}{2N}) - E(k)\sin(\frac{2\pi kn}{2N})], n = 0, 1, ..., 2N-1 \quad (5.8)$$

From Equation 5.8, it can be seen that the imaginary values at the IFFT's out-
put are always zero. These real parts are often used to drive an optical modulator
or laser. Alternatively, the IFFT's input pairs with the same imaginary part but a
negated real part $(X(2N - k) = -X^*(k), k = 1, 2, ..., 2N - 1.X(0) = X(N) = 0)$,

which is named skew-Hermitian symmetry [191], can be used to force the real parts of the IFFT's output to zero, producing a signal only at its imaginary outputs. This can be concluded from Equation 5.9, which is written for when $X(k)$ has skew-Hermitian symmetry.

$$x(n) = \frac{2j}{2N} \sum_{k=0}^{N-1} [D(k) \sin(\frac{2\pi kn}{2N}) + E(k) \cos(\frac{2\pi kn}{2N})], n = 0, 1, ..., 2N-1 \quad (5.9)$$
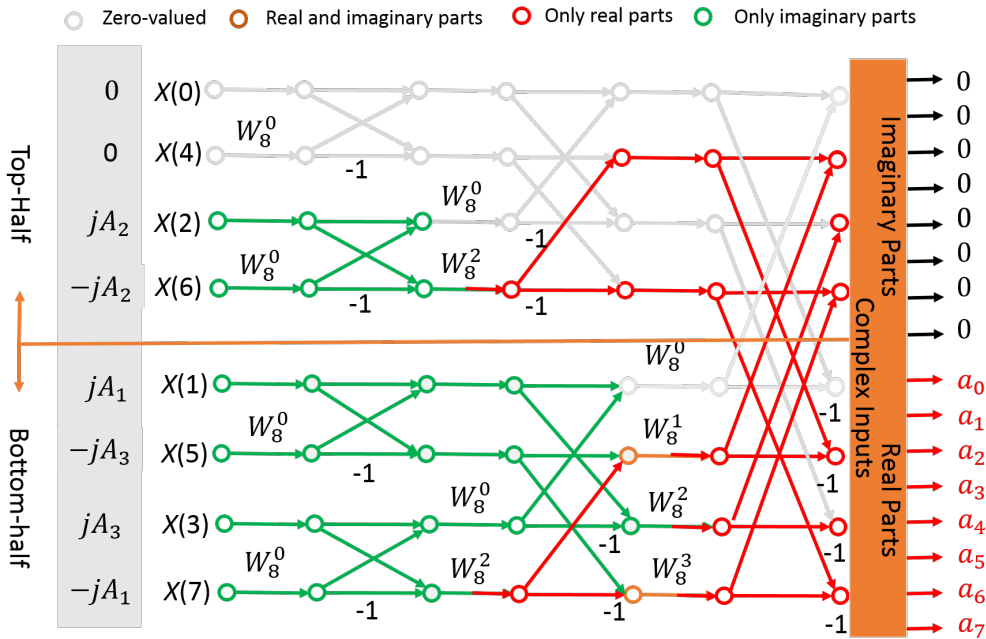
FIGURE 5.5: An 8-point radix-2 decimation-in-time IFFT butterfly flow chart, which is used to illustrate the waveform generation for Layer 1.

We have learned that one complex-valued FFT could be used to compute two real-valued FFTs. If the Hermitian symmetrical and skew-Hermitian symmetrical signals are used as the IFFT's inputs, we can obtain corresponding waveforms from the real and imaginary parts of IFFT's outputs. It has been proven that smaller IFFT sizes can be used in the higher layers for LACO-OFDM because the signals in higher layers are periodic [65]. As the ASE-DMT signals also use different layers to remove the clipping distortion, smaller IFFT sizes can also be applied to the implementation of higher layers in the ASE-DMT transmitter. By using both the real and imaginary parts of IFFT and using smaller IFFTs in higher layers, I now experimentally demonstrate that: (a) re-arranging the IFFT's inputs and (b) extracting signals from within the IFFT, can reduce the computation for all layers of ASE-DMT to that of one complex IFFT. This algorithm requires only a slight change to a standard IFFT module.
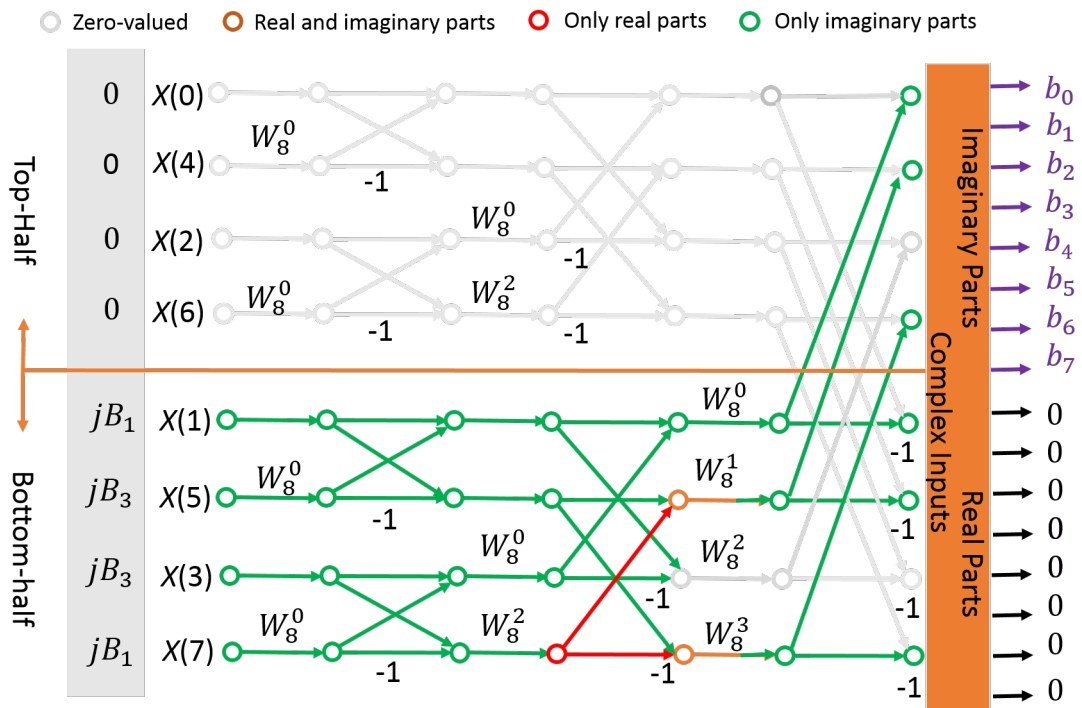
FIGURE 5.6: An 8-point radix-2 decimation-in-time IFFT butterfly flow chart, which is used to illustrate the waveform generation for Layer 2.
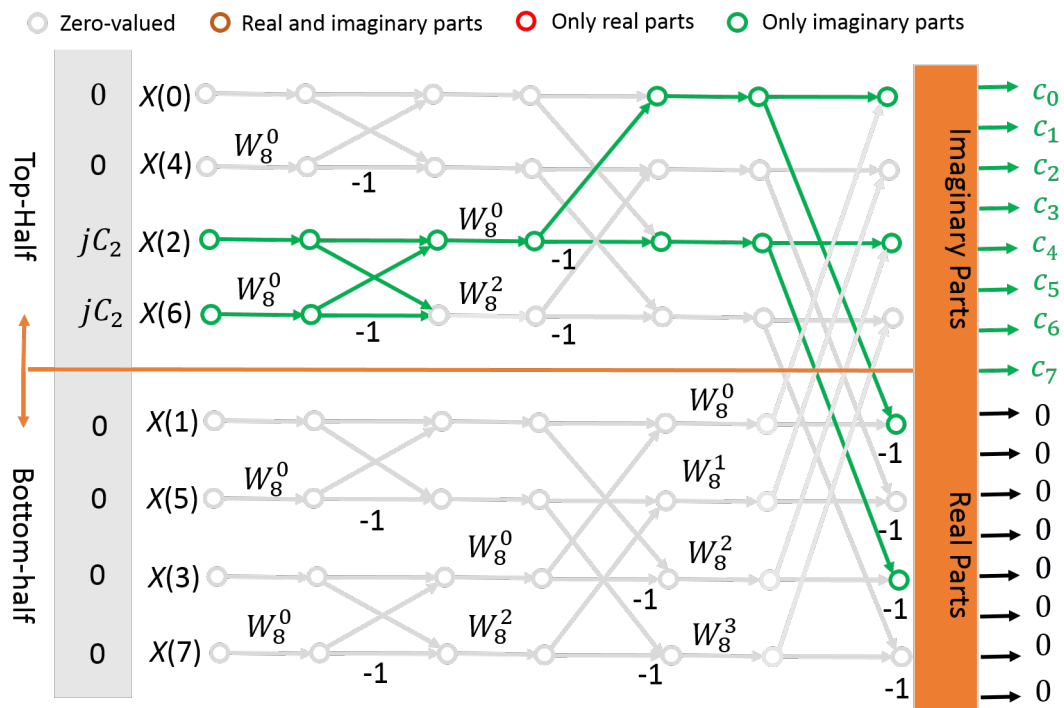
FIGURE 5.7: An 8-point radix-2 decimation-in-time IFFT butterfly flow chart, which is used to illustrate the waveform generation for Layer 3.

Fig. 5.5, 5.6 and 5.7 illustrate how a complex 8-point DIT radix-2 IFFT butterfly can generate separate outputs for three layers simultaneously. The $X(0)$ and $X(4)$ inputs of the 8-point IFFT are zero-valued. In modification (a), Layer 1's PAM modulator outputs (A_1, A_2, A_3) and their Hermitian counterparts $(-A_1, -A_2, -A_3)$ are assigned to the imaginary IFFT inputs; Layer 2's PAM modulator outputs (B_1, B_3) and their skew-Hermitian counterparts (B_1, B_3) are also assigned to the same imaginary IFFT inputs but only in the bottom-half; Layer 3's PAM modulator output (C_2) and its skew-Hermitian counterpart (C_2) are distributed to the corresponding IFFT's imaginary inputs in the top-half. The data streaming in the butterfly for the three layers are shown in Fig. 5.5 for Layer 1, Fig. 5.6 for Layer 2 and Fig. 5.7 for Layer 3. All the PAM signals from all layers are distributed to the imaginary parts of the IFFT. Finally, the data is steered separately to the real parts (a_n) and imaginary parts $(b_n$ and $c_n)$ of the IFFT's outputs, although complex values occur in the internal butterfly. This is because that the PAM signal from the first layer has Hermitian symmetry; whereas the PAM signals from the second and third layers have skew-Hermitian symmetry.
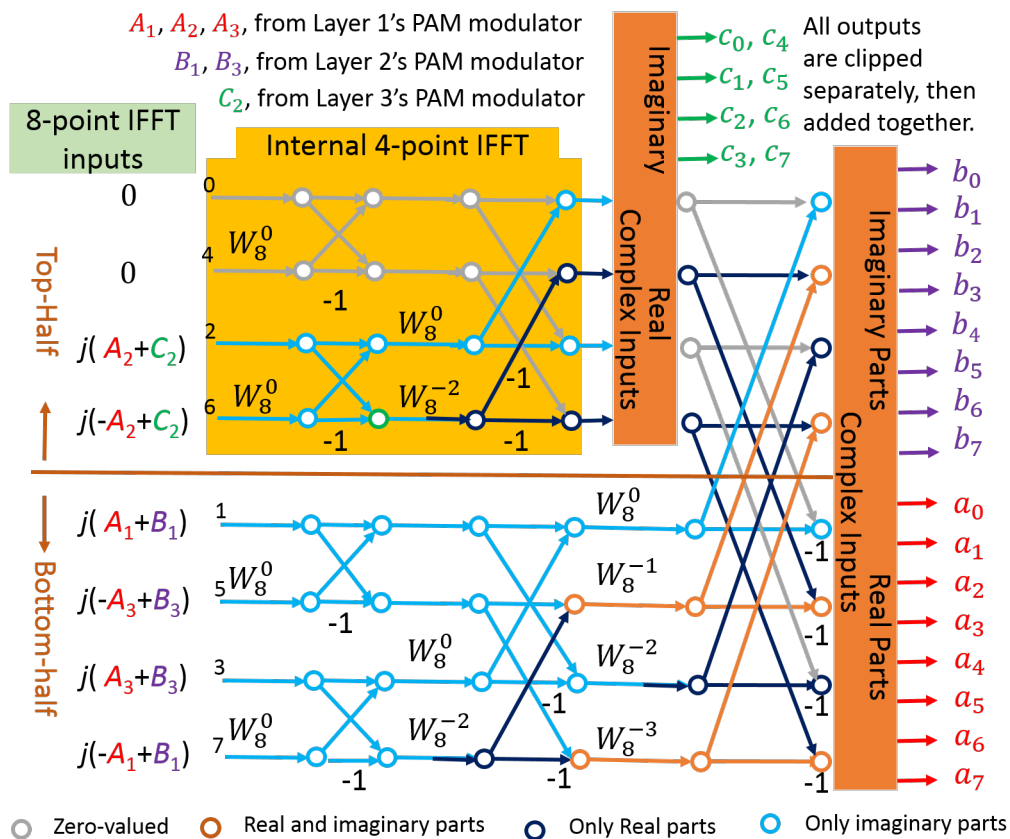
FIGURE 5.8: An 8-point radix-2 decimation-in-time IFFT butterfly flow chart.

However, as the results $(b_n$ and $c_n)$ from Layer 2 and Layer 3 both flow to the

imaginary outputs of IFFT, we need to separate them within the IFFT butterfly before their data flows interact. In modification (b), as shown in Fig. 5.8, we uses the convenient fact that the top/bottom data flows in complex IFFTs are separate except in the final butterfly. Thus, the 4-point sub-IFFT (orange area in Fig. 5.8) is used for Layer 3, and similarly the bottom-half computations for Layer 2. By extracting the output of the sub-IFFT of Layer 3 (c_n) before the final butterfly, the outputs of Layer 2 are not polluted by the outputs of Layer 3. This is achieved by separating the real and imaginary parts of the data just after the 4-point sub-IFFT: the become Layer 3's real waveform after the block (c_1, c_2, c_3, c_4) is duplicated. The real parts of the orange area flow into the final butterfly, which calculates the waveforms for Layer 1. Conveniently, Layer 1 (a_n) is contained in the real parts of the IFFT's final outputs and Layer 2 (b_n) is in its imaginary parts. Thus these two waveforms can be separately clipped before summation with Layer 3's clipped waveform. By applying Modification (b) multiple times, ASE-DMT transmitter with more than 3 layers can also be implemented using one IFFT.

5.3.3 Transmitter DSP Implementation

In ASE-DMT, four layers will give the 93.75% (= 1/2 + 1/4 + 1/8 + 1/16) spectral efficiency of DCO-OFDM. By further increasing the number of layers, the ASE-DMT will eventually achieve the same spectral efficiency as DCO-OFDM. However, as the iterative receiver needs to repeat the decoding process for each layer, there is a trade-off between increasing spectral efficiency and reducing computational complexity. Four layers were used in our experimental demonstration.
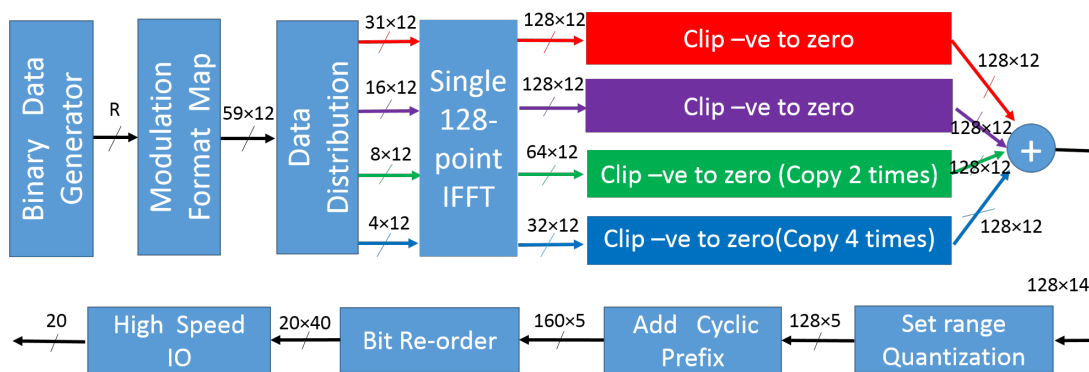
FIGURE 5.9: DSP function implemented in the FPGA with a single 128-point IFFT.

The Spiral FFT/IFFT IP Core Generator [180] was also used to generate one fully streaming 128-point IFFT Verilog code in this chapter. In this experimental

demonstration, I slightly modified the generated Verilog code in order to extract the temporary calculation results within the IFFT module. All the DSP functions were implemented in a Virtex-6 FPGA chip. Fig. 5.9 shows DSP functions performed in the FPGA. The test data and two training symbols were stored in the FPGA. For each clock cycle, R data bits were mapped to 59 PAM symbols. R depends on the modulation format on all the subcarriers, with $R = 30 \times \log_2 M$ for M-PAM, so R=59 for 2-PAM or R=118 for 4-PAM. The IFFT core used 12-bit resolution, which was carefully selected as a compromise between computational accuracy and hardware resource occupation, which has been discussed in Chapter 4. Afterwards, these 59 symbols, combined with their Hermitian counterparts, were distributed to the four layers through a data distribution module in the way as illustrated in Fig. 5.8. Within the IFFT module, the waveforms of each layer were extracted at different IFFT butterfly stages. As the IFFT module was fully pipelined, in order to align the outputs in all the layers, additional registers were added to delay the outputs of higher layers by a certain number of clocks. In each layer, the waveforms were clipped to remove all negative values and then repeated to form 128 12-bit real words before being added together. In order to reduce the required number of adders, the same adding procedure was used as the real-time LACO-OFDM transmitter. The set-range and quantization module transformed the 128 14-bit words into 128 5-bit words, each being a sample of the OFDM waveform within one OFDM symbol. Then a 32-sample cyclic prefix (CP) was pre-pended to every OFDM symbol, producing 160 5-bit words. The DAC required four data streams at one quarter of the sample rate, thus 20 FPGA's LVDS (low voltage differential signaling) channels must be used, each at a rate of 6.25 Gbaud. The DAC multiplexed these 4 channels, then produced a 25 Gsample/s 5-bit resolution analog output.

5.3.4   Logic Resource Utilization

We have shown that the ASE-DMT transmitter can be implemented in the FPGA using only one 128-point IFFT. This is called Scheme 4. In order to see its hardware resource utilization advantage, another ASE-DMT transmitter was also implemented in the FPGA using four IFFT modules, which is called Scheme 5. In Layer 1, a 128-point IFFT was used. In Layers 2, 3 and 4, 128-point, 64-point and 32-point IFFTs were used. We optimized the IFFT Verilog code of Layers 2, 3 and 4 to only calculate the bottom-half of the butterfly chart, as these three layers had regular zero-valued IFFT's inputs. This optimization method has been discussed

in Chapter 4. The other DSP functions were all the same for these two schemes, as shown in Fig. 5.9.
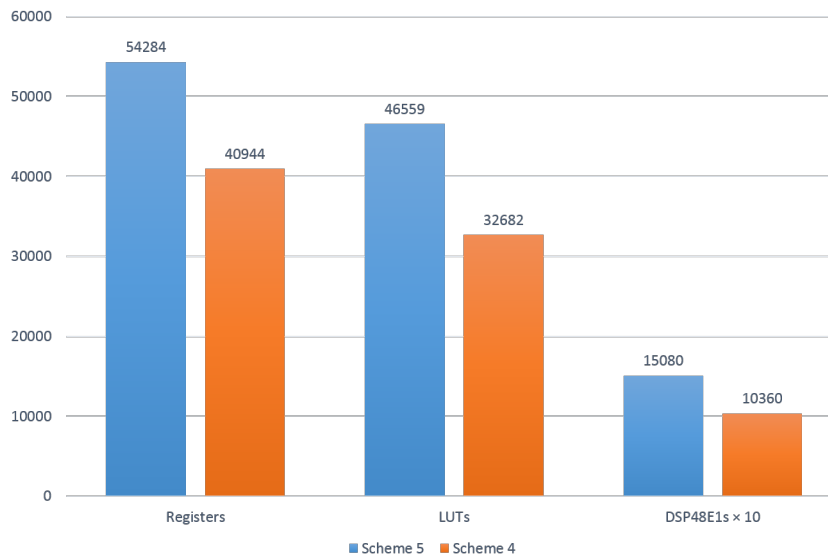
FIGURE 5.10: Resource utilization of the implementation for Schemes 4 and 5.

The implementation cost for Scheme 4 and 5 are shown in Fig. 5.10. Of the available resources on the Vertix-6 FPGA (XC6VLX240T), it was reported by the Xilinx Integrated Synthesis Environment (ISE) that the Scheme 4 used 13% of the slice registers (40944), 21% of the slice LUTs (32682) and 134% of the DSP48E1s (1036) and the Scheme 5 used 18% of the slice registers (54284), 30% of the slice LUTs (46559) and 196% of the DSP48E1s (1508). Obviously, this is not implementable, because during the synthesis, the ISE software was forced to use DSP48E1s to implement the multipliers. In the actual hardware implementation, other parts of the logic resource can be allocated to do the multiplications. In this way, Scheme 4 used 16% of the slice registers (49557), 30% of the slice LUTs (46411) and 100% of the DSP48E1s (768), so all the DSP functions still fit into the XC6VLX240T. It is clear that Scheme 4 has saved around 30% of logic resources compared with Scheme 5. This represents a significant reduction of hardware, especially for the required number of multipliers, which usually dominate the computational complexity in the IFFT implementation. Our proposed Scheme 4 can not only help to save power but also make it easily implementable in a FPGA that has limited hardware resources. This is very important for optical communication systems, which have a very high data throughput, requiring the very fast FPGAs.

5.4   Experimental Setup
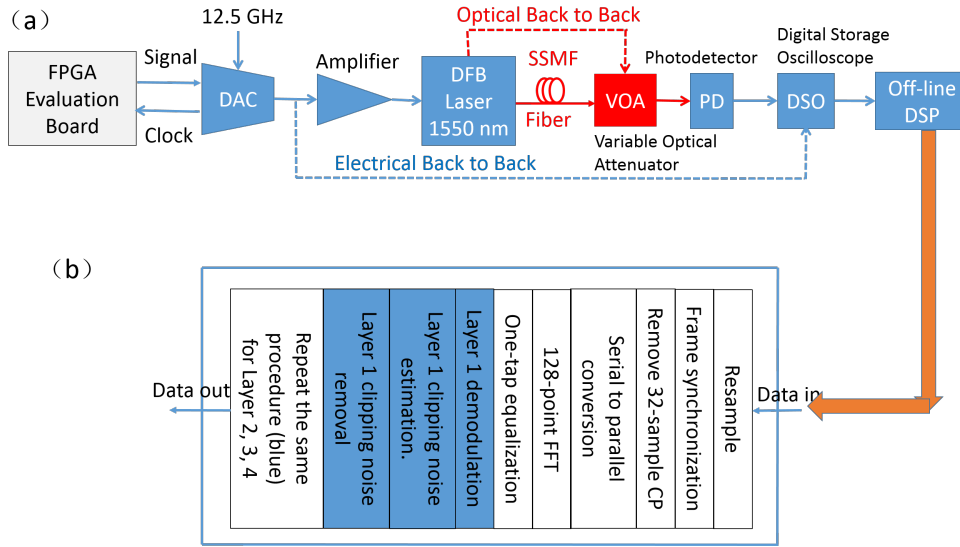
FIGURE 5.11: ASE-DMT optical transmission link: (a) setup block
diagram (b) offline DSP algorithm performed in the MATLAB.

Fig. 5.11 shows the experimental setup. A 156.25-MHz clock generated by
the DAC provided a clock for the FPGA, which was used to control all the DSP
modules in the FPGA and synchronize the FPGA and DAC. The DAC and FPGA
channels were connected via 20 pairs of length-matched coaxial cables for LVDS.
The MICRAM DAC had a resolution of 6 bits, so full operation would require
24 high-speed transmitter channels from the FPGA. However, as there were only
20 high-speed transmitters available on our FPGA evaluation board (ML623), the
four inputs corresponding to the least significant bit of DAC were connected to
logic zero, which led to a 5-bit resolution. Because 59 or 118 data bits were en-
coded for PAM2 or PAM 4, the net data rate was 9.2 or 18.4 Gb/s excluding 32-
sample CP appended in one clock.

Fig. 5.11(a) shows the block diagram for all the real-time transmission link.
The DAC's analog output signal was around 500-mV peak-to-peak. The signal
was attenuated by 18 dB, then fed through a 24-dB gain 40-GHz bandwidth linear
electrical amplifier (SHF- 807). The resulting 1-volt (p-p) output was connected to
the 1550-nm distributed feedback laser biased at 36 mA. A variable optical atten-
uator (VOA) was used to adjust the output optical power, followed by a 16-GHz
photodetector (DSC-40S) to convert optical signals to electrical signals, which
were then sampled by a real-time Digital Storage Oscilloscope (DSOX92804A)
with an 80-GS/s sampling rate. Finally, the captured samples were analysed by
offline DSP in MATLAB. The offline DSP algorithm is illustrated in Fig. 5.11(b).
After the frame synchronization, serial to parallel conversion and CP removal

were conducted, followed by a one-tap equalizer before the iterative decoding process was performed to decode the data layer by layer. Some key parameters in the entire transmission link are summarized in Table 5.1.

TABLE 5.1: Key parameters in the experimental setup for ASE-DMT.

Parameter	Value
Modulation format	PAM2 or PAM4
Oversampling rate	2
Number of layers	4
IFFT size	128-points
IFFT resolution	12 bits
CP length	32 samples
FPGA fabric clock	156.25MHz
DAC clock	12.5 GHz
DAC output voltage	500 mV
DAC sampling rate	25 GSa/s
DAC resolution	5 bits
Net bit rate	9.2 Gb/s for PAM2 or 18.4 Gb/s for PAM4
DFB laser wavelength	1550 nm
DFB laser bias current	36 mA
Amplifier bandwidth	40 GHz
Oscilloscope sampling rate	80 GSa/s
Photodetector bandwidth	16 GHz
Transmission distance	20 km for PAM2 and 10 km for PAM4

5.5 Experimental Results

5.5.1 PAM2 Link

5.5.1.1 Optical Back-to-Back

The optical back-to-back Q-factor was measured by directly connecting the laser output to the VOA set for zero optical attenuation. As shown in Fig. 5.12, the average Q-factor is 19.6 dB. There is a 3-dB penalty for the highest-frequency subcarriers, resulting from the limited laser bandwidth. The Q-factors for nearby

frequencies are very similar. Additional signal quality degradation is not seen in the high layers, indicating that there is little error propagation.
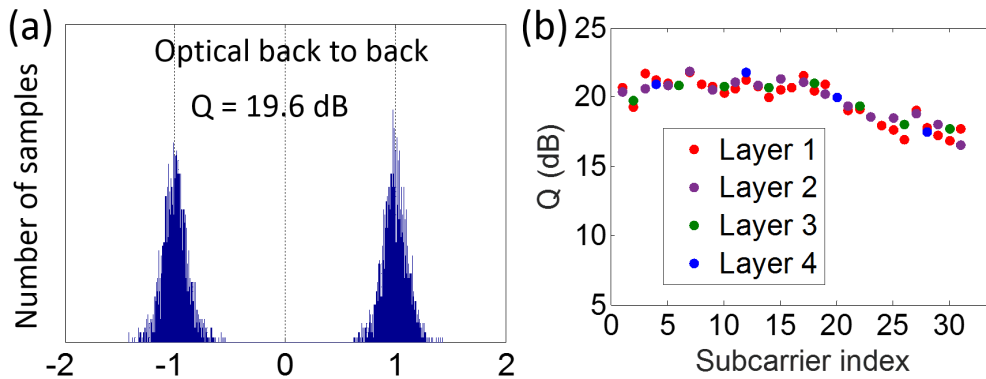
FIGURE 5.12: Histogram of (a) amplitudes and (b) Q-factor *vs* sub-carrier index for optical back-to-back in PAM2 transmission link.

5.5.1.2   Fiber Transmission
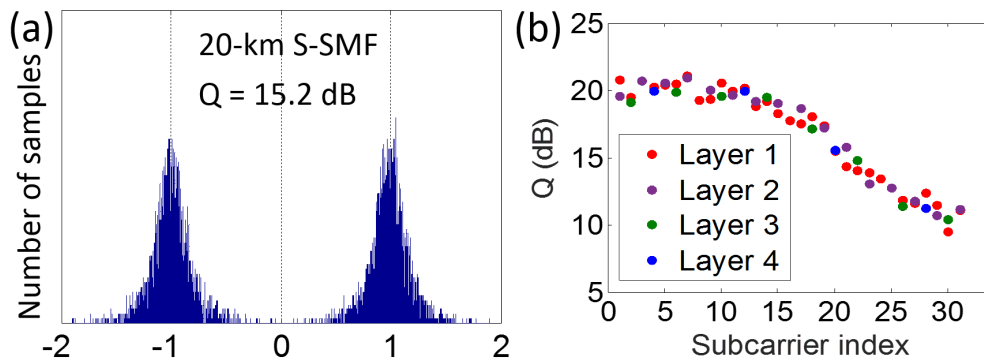
FIGURE 5.13: Histogram of (a) amplitudes and (b) Q-factor *vs* sub-carrier index for 20-km PAM2 transmission link.

The Q-factor was evaluated after transmission over a 20-km span of SSMF, without optical amplification. The Q-factor calculated from the average BER is 15.2 dB as shown in Fig. 5.13. No error propagation occurs on different layers.

5.5.2   PAM4 Link

5.5.2.1   Electrical Back-to-Back

Firstly, the Q-factor performance for electrical back-to-back configuration [see Fig. 5.11(a)] was measured by connecting the DAC output directly to a DSO. The captured samples were analyzed by offline DSP in MATLAB and the results

are shown in Fig. 5.14. As the Q-factors of adjacent-index subcarriers for the different layers are very similar, we can conclude that the iterative algorithm in the receiver substantially cancels the clipping distortion, without error propagation.
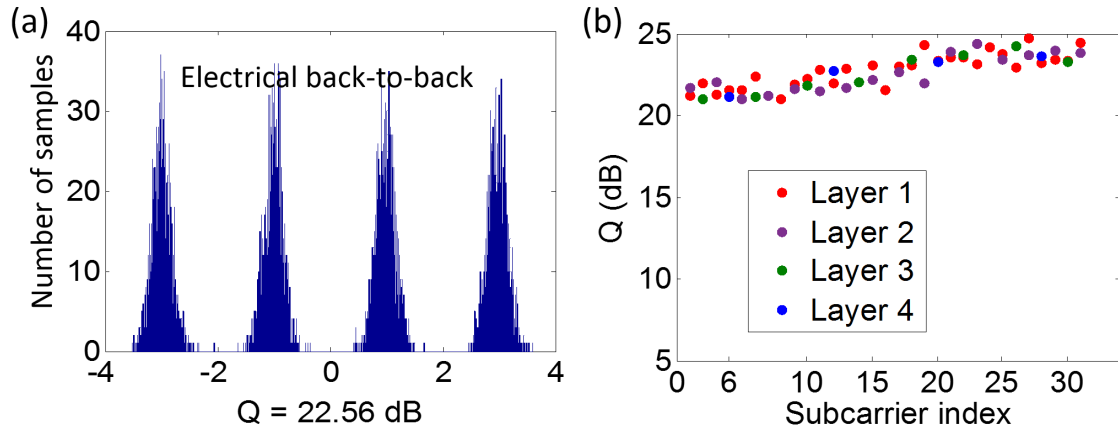
FIGURE 5.14: Histogram of (a) amplitudes and (b) Q-factor *vs* subcarrier index for electrical back-to-back in PAM4 transmission link.

5.5.2.2 Optical Back-to-Back
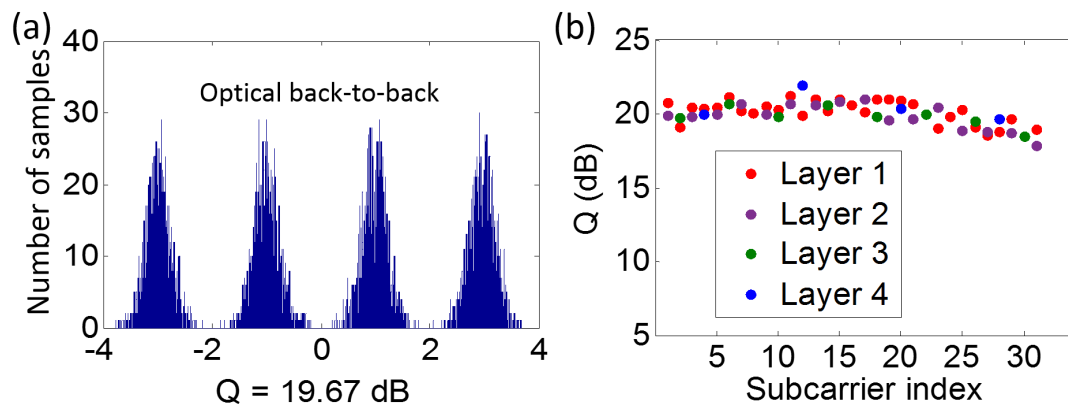
FIGURE 5.15: Histogram of (a) amplitudes and (b) Q-factor *vs* subcarrier index for optical back-to-back in PAM4 transmission link.

The optical back-to-back Q-factor was measured by directly connecting the laser output to the VOA. With zero optical attenuation, the optical power received by the photodetector was 3.53 dBm. As shown in Fig. 5.15, the average Q-factor is 19.67 dB. There is a 3-dB penalty for the highest-frequency subcarriers, resulting from the limited laser bandwidth. The Q-factors for nearby frequencies are still similar. Additional signal quality degradation is not seen in the high layers, indicating that there is little error propagation.

5.5.2.3 Fiber Transmission

Finally, the BER and Q-factors for 10-km and 20-km SSMF transmission are shown in Fig. 5.16 and 5.17 separately. The optical power after transmission over 10-km SSMF was 0.4 dBm and the average Q-factor was 18.51 dB, as shown in Fig. 5.16. There is a 5-dB penalty for the highest-frequency subcarriers; a 2-dB increase compared with optical back-to-back transmission. This is probably because of the uneven channel response induced by the interaction of laser chirp and fiber dispersion, which can be seen more clearly in Fig. 5.17. After 20-km SSMF transmission, the optical power reduced to -2.62 dBm and the signal qualities for higher-frequency subcarriers are seriously degraded. Even in the first layer, the Q-factors of the higher-frequency subcarriers are below 10 dB. A Q-factor of <10 dB means a very large number of decoding errors for PAM4. The iterative receiver will pass these decoding errors from the lower layers to the higher layers; that is why the lowest Q-factors are seen in the highest layer. Therefore, the BER after 20-km SSMF transmission is >0.1.
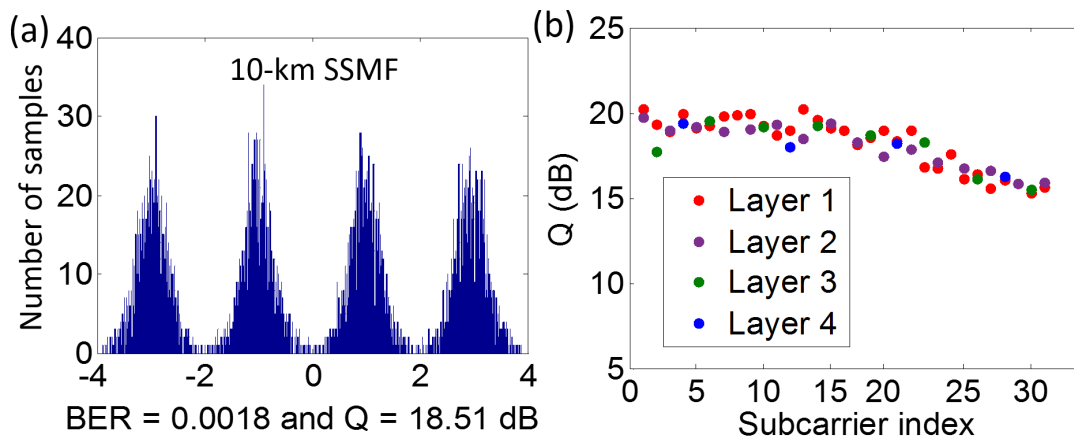
FIGURE 5.16: Histogram of (a) amplitudes and (b) Q-factor *vs* subcarrier index for 10-km PAM4 transmission link.

In order to identify the influence of fiber dispersion, the optical power attenuation was set to 6.15 dB (3.53 dBm - (-2.62 dBm)) by the VOA, to mimic the power attenuation of the 20-km SSMF and optical connectors. For back-to-back, the Q-factor was measured and is shown in Fig. 5.18. The average Q-factor is around 17 dB and it is almost equal for the adjacent subcarriers in all the four layers; no decoding error propagation occurs between different layers. The BER is 2.6×10^{-3}, is still below the 7% FEC limit, corresponding to the BER of 3.8×10^{-3}. Both the Q-factors and BERs shown in Fig. 5.18 are significantly better when compared with those in Fig. 5.17, which means that the 6.15-dB power attenuation from the

(a)

(b)
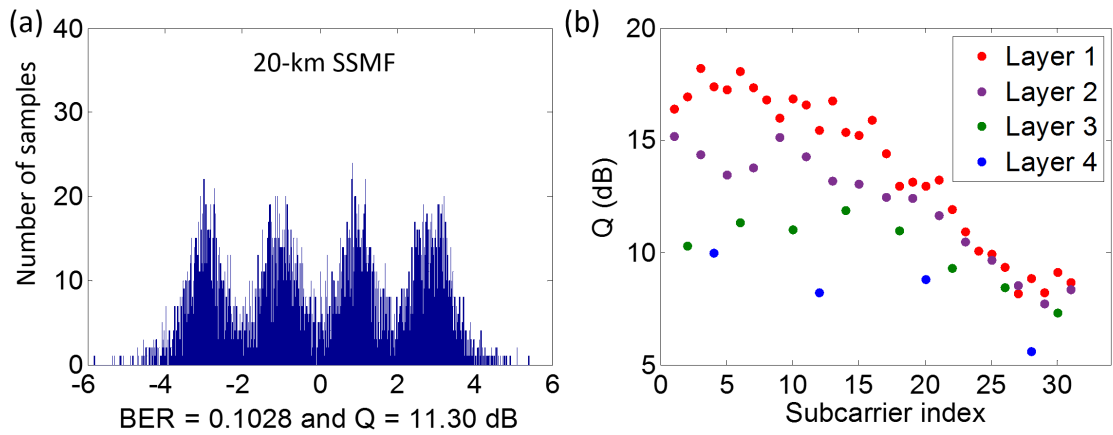
FIGURE 5.17: Histogram of (a) amplitudes and (b) Q-factor *vs* subcarrier index for 20-km PAM4 transmission link.

(a)

(b)
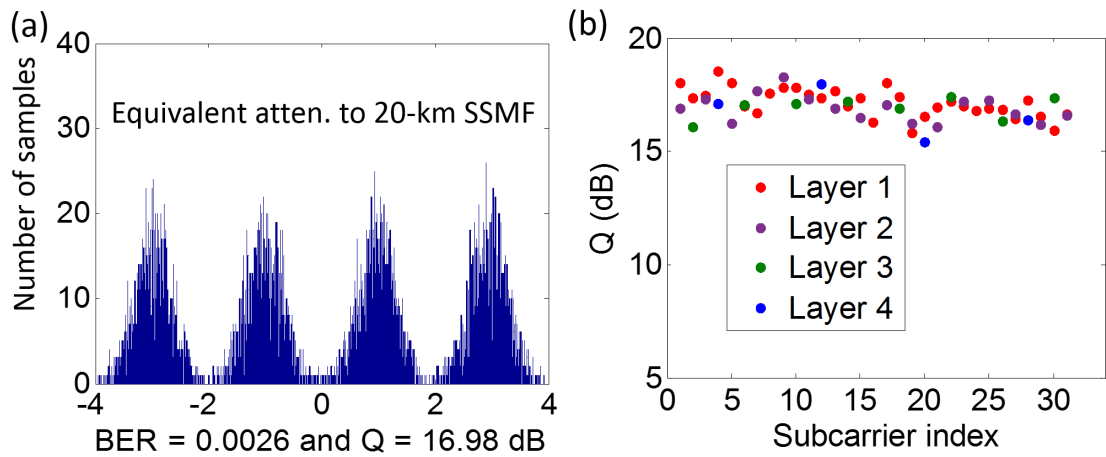
FIGURE 5.18: Histogram of (a) amplitudes and (b) Q-factor *vs* subcarrier index for back-to-back PAM4 transmission link with 6.15 dB optical power attenuation.

20-km SSMF and optical connectors cannot alone lead to the transmission failure. Therefore, we can conclude that the serious higher frequency signal quality degradation, as shown in Fig. 5.17, leads to the transmission failure over 20-km SSMF, which mainly result from the interaction of laser chirp and fiber dispersion.

5.6 Conclusions

In this chapter, a computationally efficient real-time modulated ASE-DMT transmitter has been proposed and experimentally demonstrated. A net data rate of 9.2 Gb/s for PAM2 or 18.4 Gb/s for PAM4 is achieved. ASE-DMT transmitter usually requires one IFFT per layer, we show that by inputs mapping and extracting outputs from within the IFFT, only one IFFT is required to generate the

outputs of all the layers. By implementing within one FPGA chip, 30% logic re-source utilization can be saved, compared with a common ASE-DMT transmitter using one IFFT per layer. With off-line signal processing in the receiver, the ASE-DMT signals have been successfully transmitted over 20-km SSMF for PAM2 and 10-km SSMF for PAM4.

Chapter 6

Conclusions

6.1 Thesis Overview

This thesis has investigated the power-efficient OFDM algorithms and their efficient implementation method in short-haul optic-fiber links. All these power-efficient OFDM signals were generated in real-time using a FPGA and DAC. Their implementation cost in the transmitter was optimized. By using a real-time oscilloscope and offline DSP in MATLAB, their signal quality was measured and analysed in the short-haul fiber-optic link.

Chapter 2 introduced the research background and literature review. It consisted of three major parts. Firstly, the promising modulation formats with higher spectral efficiency, which could further upgrade the data rate in short-haul fiber-optic links were reviewed. Then development of power-efficient optical OFDM algorithms used in IMDD based optical communication system was discussed. Finally, the real-time experiments carried out in both the short-haul and long-haul optical communication systems were generally discussed.

Chapter 3 began with an efficient implementation of an ACO-OFDM transmitter, by discarding the Hermitian symmetrical constraints on the IFFT's inputs. Via interleaving the inphase and quadrature components of OFDM subcarriers in the transceiver, the size of IFFT/FFT could be reduced by half. Furthermore, by taking advantage of the zero-inputs in the ACO-OFDM transmitter, the implementation cost for ACO-OFDM transmitter was further reduced. Finally, a real-time ACO-OFDM transmitter was experimentally demonstrated using a FPGA and DAC in the transmitter and offline signal processing in the receiver.

Chapter 4 gave a detailed analysis of LACO-OFDM algorithm. Firstly, the algorithm's principle was depicted, followed by some simulation results, showing that LACO-OFDM consumed less optical power compared with DCO-OFDM. Then experiments were shown using offline signal processing in the transceiver. The results showed that LACO-OFDM can reach the maximum transmission performance with a lower DC bias of laser. A more powerful equalizer such as a

Volterra filter was useful to further enhance the performance of LACO-OFDM. Finally, a novel implementation method for LACO-OFDM transmitter was proposed. Previous designs require one IFFT per layer. I proposed that one *middle-out* IFFT was enough to generate the waveforms for all the layers by mapping all the data-carrying subcarriers into one IFFT and extracting the waveforms for all layers from this single IFFT. The implementation results indicated that almost the same logic resource utilization was achieved for LACO-OFDM, compared with the DCO-OFDM transmitter. Using offline DSP in the receiver, a real-time LACO-OFDM signal was successfully experimentally transmitted in a fiber link.

Chapter 5 analysed the ASE-DMT algorithm. As the ASE-DMT still used the layer concept to encode data on the unused inphase components of OFDM subcarriers, the waveform extraction within the IFFT module was also useful in the implementation of ASE-DMT transmitter. However, I altered the mapping method to fit into the fact that only inphase or quadrature components of OFDM subcarriers are used to carry data in ASE-DMT. By mapping all the PAM signals with their Hermitian or skew-Hermitian counterparts into the imaginary parts of one IFFT, the waveforms for all the layers could be obtained from the inphase and quadrature components of a single *middle-out* IFFT. Finally, the ASE-DMT transmitter was implemented in the FPGA and experimentally demonstrated in a short-haul fiber-optic link by using offline DSP in the receiver.

6.2   Future Work

6.2.1   Non-Hermitian Symmetrical LACO-OFDM

In Chapter 3 and Chapter 4, two different efficient implementation methods are proposed for ACO-OFDM and LACO-OFDM. By using Non-Hermitian symmetrical IFFT, the size of IFFT for ACO-OFDM transmitter is reduced by half. I also propose that the LACO-OFDM signal can be generated by using only one *middle-out* IFFT. Because Hermitian symmetry is not necessary for the single-IFFT implementation of LACO-OFDM transmitter, the non-Hermitian symmetrical implementation method should also be useful for LACO-OFDM. By combining these two techniques, a more efficient implementation is expected for LACO-OFDM transmitter. Of course, the concatenation and split of inphase and quadrature components for LACO-OFDM will bring challenges, which will be an interesting research direction. It should be note that the single-IFFT implementation for

ASE-DMT depends on the Hermitian symmetrical inputs, so non-Hermitian symmetrical IFFT cannot be used directly. It is also very interesting to exploit whether a similar efficient implementation method exists or not for ASE-DMT.

6.2.2 Real-Time LACO-OFDM and ASE-DMT Receivers

The real-time LACO-OFDM and ASE-DMT receivers have not been demonstrated because there is no ADC available in our Lab. Compared with the DSP in the transmitter, the DSP in the receiver is more complex. For example, both several IFFTs and FFTs are required in the receiver. Since all the IFFTs in the receiver are used to regenerate the clipping noise, our single-IFFT method can definitely be used to merge all the IFFTs into one IFFT. However, for the many FFTs, novel ideas are required to reduce the overall implementation cost. Besides, in the receiver, synchronization of OFDM symbols and equalization will significantly increase the utilization of logic resources, which maybe have an impact on the signal quality in the transmission experiment, because the limited resources may reduce the accuracy of the synchronization and equalization.

6.2.3 Bit- and Power-loading for LACO-OFDM and ASE-DMT

In the real-time experimental demonstrations for LACO-OFDM and ASE-DMT, compared with the low-frequency subcarriers, the high-frequency subcarriers suffer a larger penalty after transmission over 20-km SSMF, which leads to the occurrence of the decoding error in the first layer for 16-QAM. These errors propagate to higher layers, causing a larger and larger decoding errors, which limits the signal's transmission distance at a high data rate.

Bit- and power-loading has been used in the optical OFDM system to improve its transmission performance because different modulation formats and power can be loaded into separate OFDM subcarriers according to the measured SNR in the receiver [192], [193]. Because the high-frequency subcarriers for LACO-OFDM and ASE-DMT have a lower SNR, so a less spectrally efficient modulation format (QPSK) or a larger power can be allocated to these subcarriers to reduce their decoding errors. It is expected that there will be no error propagation among different layers. By using bit- and power-loading, LACO-OFDM and ASE-DMT should be able to transmit over a longer distance at a higher data rate.

Appendix A

Channel Synchronization of FPGA

The commercially available FPGA is usually not able to operate source synchronization in gigabit SerDes mode [194], so the FPGA channels need to be aligned to guarantee that the digital outputs from FPGA arrive at the DAC at the same time. There are two modes that can be used to synchronize all the high-speed channels in the FPGA. In our experiment, the Sync2PRBS mode is selected for the synchronization using the built-in PRBS of the DAC. In this mode, the bit stream from the FPGA is de-scrambled (XOR) with the built-in PRBS from DAC. Therefore, the bit stream needs to be scrambled in the FPGA fabric. When both sequences are identical, we have a constant output of logic 0 after descrambling.
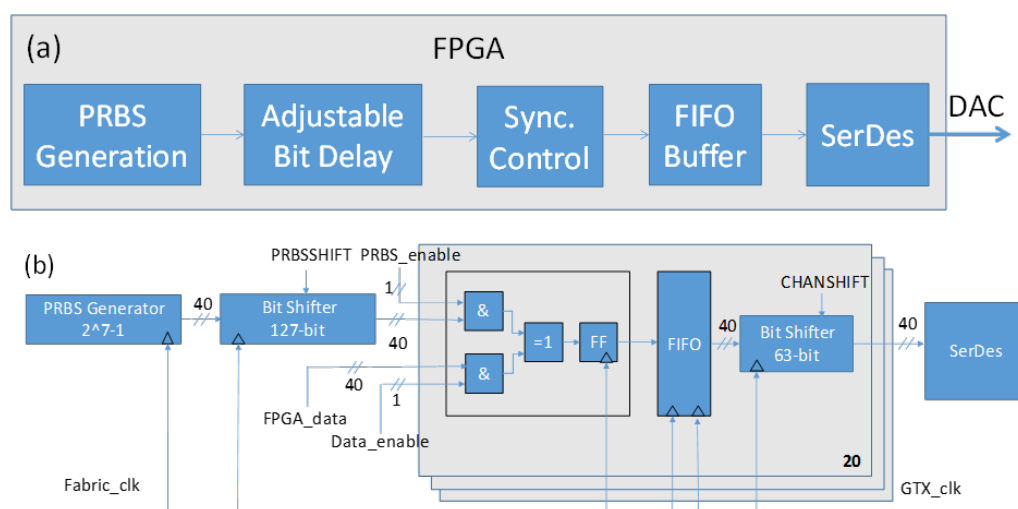
FIGURE A.1: Channel Synchronization (a) FPGA channel synchronization blocks (b) Synchronization modules implementation.

The channel synchronization modules and their implementation in the FPGA are shown in Fig. A.1 (a) and (b) [181]. In Fig. A.1(a), PRBS module generates the synchronization pattern. Its bit can be delayed through the bit delay module. Synchronization control module is used to change status between synchronization and data transmission. Asynchronous first-in first-out (FIFO) buffers guarantee data consistency before they are passed to the SerDes to achieve parallel to

serial conversion. In Fig. A.1(b), the GTX_clk and Fabric_clk are running at the SerDes data rate divided by 40. In our experiment, the data rate of SerDes was 6.25 Gb/s, so both GTX_clk and Fabric_clk were 156.25 MHz. The high speed transmitter (GTX) from FPGA were configured to work with 40-bit wide data, and all buffering and encoding blocks were bypassed. In this configuration, we had two GTX clock domains because 20 SerDes channels were configured, but one GTX clock can only drive up to 12 SerDes channels. One GTX clock was selected to drive the fabric logic, so 20 small FIFOs of 16-word depth were required to compensate for the phase different between GTX_clk and Fabric_clk. In the synchronization module, all the GTX channels shared the same master 2^7-1 PRBS generator, which can generate 40-bit wide data words in one clock. One master bit shifter which can be shifted up to 127 bits were implemented following the PRBS generator. This master bit shifter was initialized to shift 0 position. In addition, each channel had individual bit shifter, which can allow for shifting each channel up to 63-bit positions. These bit shifters were all initialized to shift 32-bit positions. During synchronization, setting Data_enable = 0 and PRBS_enable =1 in the FPGA to ensure that FPGA sent PRBS without data on all channels. The synchronization can start with any channel. Firstly, the bit delay of first channel was kept constant at 32 bits and the master bit shifter was used instead. Once a synchronization was detected, the FPGA PRBS was aligned to the DAC PRBS. Then all the other channels were synchronized one-by-one. For each channel, its CHANSHIFT was swept from 0 to 63. Once the synchronization was detected for one channel by reading the synchronization status from register in the DAC constantly, another channel was synchronized using the same procedure until all the 20 channels had been synchronized. In this situation, all the input data streams to the DAC were constant zero. After successful synchronization of all channels, data transmission can be started by setting Data_enable = 1 and PRBS_enable =1.

Bibliography

[1] Cisco, *The zettabyte era: trends and analysis,* `https://www.cisco.com/c/en/us/solutions/collateral/service-provider/visual-networking-index-vni/`.

[2] J. Hecht, *City of light: the story of fiber optics.* Oxford University Press on Demand, 2004.

[3] K. Kao and G. A. Hockham, "Dielectric-fibre surface waveguides for optical frequencies", in *Proceedings of the Institution of Electrical Engineers*, IET, vol. 113, 1966, pp. 1151–1158.

[4] F. Kapron, D. B. Keck, and R. D. Maurer, "Radiation losses in glass optical waveguides", *Applied Physics Letters*, vol. 17, no. 10, pp. 423–425, 1970.

[5] T. Miya, Y Terunuma, T. Hosaka, and T. Miyashita, "Ultimate low-loss single-mode fibre at 1.55 μm", *Electronics Letters*, vol. 15, no. 4, pp. 106–108, 1979.

[6] T. D. Germann, "Semiconductor laser concepts", in *Design and Realization of Novel GaAs Based Laser Concepts*, Springer, 2012, pp. 5–15.

[7] G. Keiser, *Optical fiber communications.* Wiley Online Library, 2003.

[8] T. Okoshi, K Emura, K Kikuchi, and R. T. Kersten, "Computation of bit-error rate of various heterodyne and coherent-type optical communication schemes", *Journal of Optical Communications*, vol. 2, no. 3, pp. 89–96, 1981.

[9] R. J. Mears, L Reekie, I. Jauncey, and D. N. Payne, "Low-noise erbium-doped fibre amplifier operating at 1.54 μm", *Electronics Letters*, vol. 23, no. 19, pp. 1026–1028, 1987.

[10] K. Fukuchi, T. Kasamatsu, M. Morie, R. Ohhira, T. Ito, K. Sekiya, D. Ogasahara, and T. Ono, "10.92-Tb/s (273 x 40-Gb/s) triple-band/ultra-dense WDM optical-repeatered transmission experiment", in *Optical Fiber Communication Conference*, Optical Society of America, 2001, PD24.

[11] M. S. Faruk and S. J. Savory, "Digital signal processing for coherent transceivers employing multilevel formats", *Journal of Lightwave Technology*, vol. 35, no. 5, pp. 1125–1141, 2017.

[12]   R. A. Soriano, F. N. Hauske, N. G. Gonzalez, Z. Zhang, Y. Ye, and I. T. Monroy, "Chromatic dispersion estimation in digital coherent receivers", *Journal of Lightwave Technology*, vol. 29, no. 11, pp. 1627–1637, 2011.

[13]   K. Kikuchi and S. Tsukamoto, "Evaluation of sensitivity of the digital coherent receiver", *Journal of Lightwave Technology*, vol. 26, no. 13, pp. 1817–1822, 2008.

[14]   R. Griffin and A. Carter, "Optical differential quadrature phase-shift key (oDQPSK) for high capacity optical transmission", in *Optical Fiber Communication Conference and Exhibit, 2002. OFC 2002*, IEEE, 2002, pp. 367–368.

[15]   H. Sun, K.-T. Wu, and K. Roberts, "Real-time measurements of a 40 Gb/s coherent system", *Optics Express*, vol. 16, no. 2, pp. 873–879, 2008.

[16]   E. Yamazaki, S. Yamanaka, Y. Kisaka, T. Nakagawa, K. Murata, E. Yoshida, T. Sakano, M. Tomizawa, Y. Miyamoto, S. Matsuoka, *et al.*, "Fast optical channel recovery in field demonstration of 100-Gbit/s Ethernet over OTN using real-time DSP", *Optics Express*, vol. 19, no. 14, pp. 13 179–13 184, 2011.

[17]   M. Birk, P. Gerard, R. Curto, L. Nelson, X. Zhou, P. Magill, T. Schmidt, C. Malouin, B. Zhang, E. Ibragimov, *et al.*, "Real-time single-carrier coherent 100 Gb/s PM-QPSK field trial", *Journal of Lightwave Technology*, vol. 29, no. 4, pp. 417–425, 2011.

[18]   A. J. Lowery, L. Du, and J. Armstrong, "Orthogonal frequency division multiplexing for adaptive dispersion compensation in long haul wdm systems", in *Optical Fiber Communication Conference*, Optical Society of America, 2006, PDP39.

[19]   W. Shieh and C Athaudage, "Coherent optical orthogonal frequency division multiplexing", *Electronics letters*, vol. 42, no. 10, pp. 587–589, 2006.

[20]   B. J. Schmidt, Z. Zan, L. B. Du, and A. J. Lowery, "120 Gbit/s over 500-km using single-band polarization multiplexed self-coherent optical OFDM", *Journal of lightwave technology*, vol. 28, no. 4, pp. 328–335, 2010.

[21]   B. J. Schmidt, Z. Zan, L. B. Du, and A. J. Lowery, "100 Gbit/s transimssion using single-band direct-detection optical OFDM", in *National Fiber Optic Engineers Conference*, Optical Society of America, 2009, PDPC3.

[22]   W.-R. Peng, I. Morita, H. Takahashi, and T. Tsuritani, "Transmission of high-speed (> 100 Gb/s) direct-detection optical OFDM superchannel", *Journal of Lightwave Technology*, vol. 30, no. 12, pp. 2025–2034, 2012.

[23] W. Shieh, Q. Yang, and Y. Ma, "107 Gb/s coherent optical OFDM transmission over 1000-km SSMF fiber using orthogonal band multiplexing", *Optics Express*, vol. 16, no. 9, pp. 6378–6386, 2008.

[24] Y. Ma, Q. Yang, Y. Tang, S. Chen, and W. Shieh, "1-tb/s single-channel coherent optical ofdm transmission over 600-km ssmf fiber with subwavelength bandwidth access", *Optics express*, vol. 17, no. 11, pp. 9421–9427, 2009.

[25] S Chandrasekhar, X. Liu, B Zhu, and D. Peckham, "Transmission of a 1.2-Tb/s 24-carrier no-guard-interval coherent OFDM superchannel over 7200-km of ultra-large-area fiber", in *Optical Communication, 2009. ECOC'09. 35th European Conference on*, IEEE, vol. 2009, 2009, pp. 1–2.

[26] OFC2018, *Dsp for short reach and client optics - what makes sense?*, `https://www.ofcconference.org/en-us/home/program-speakers/workshops/dsp-for-short-reach-and-client-optics/`.

[27] Ethernet-Alliance, *The 2018 ethernet roadmap*, `https://ethernetalliance.org/the-2018-ethernet-roadmap/`.

[28] A. Andrae, "Total consumer power consumption forecast", Oct. 2017.

[29] R. S. Tucker, "Green optical communications—part I: energy limitations in transport", *IEEE Journal of selected topics in quantum electronics*, vol. 17, no. 2, pp. 245–260, 2011.

[30] P. J. Winzer and R.-J. Essiambre, "Advanced optical modulation formats", *Proceedings of the IEEE*, vol. 94, no. 5, pp. 952–985, 2006.

[31] B. S. G. Pillai, B. Sedighi, K. Guan, N. P. Anthapadmanabhan, W. Shieh, K. J. Hinton, and R. S. Tucker, "End-to-end energy modeling and analysis of long-haul coherent transmission systems", *Journal of Lightwave Technology*, vol. 32, no. 18, pp. 3093–3111, 2014.

[32] P. Winzer, A. Gnauck, C. Doerr, M Magarini, and L. Buhl, "Spectrally efficient long-haul optical networking using 112-Gb/s polarization multiplexed 16-QAM", *Journal of lightwave technology*, vol. 28, no. 4, pp. 547–556, 2010.

[33] S. Wolf, M. Lauermann, P. Schindler, G. Ronniger, K. Geistert, R. Palmer, S. Köber, W. Bogaerts, J. Leuthold, W. Freude, *et al.*, "DAC-less amplifierless generation and transmission of QAM signals using sub-volt silicon-organic hybrid modulators", *Journal of Lightwave Technology*, vol. 33, no. 7, pp. 1425–1432, 2015.

[34] G.-W. Lu, M. Sköld, P. Johannisson, J. Zhao, M. Sjödin, H. Sunnerud, M. Westlund, A. Ellis, and P. A. Andrekson, "40-Gbaud 16-QAM transmitter using tandem IQ modulators with binary driving electronic signals", *Optics Express*, vol. 18, no. 22, pp. 23 062–23 069, 2010.

[35] T. Sakamoto, A. Chiba, and T. Kawanishi, "50-Gb/s 16-QAM by a quad-parallel mach-zehnder modulator", in *Optical Communication-Post-Deadline Papers (published 2008), 2007 33rd European Conference and Exhibition of*, VDE, 2007, pp. 1–2.

[36] G.-W. Lu, T. Sakamoto, A. Chiba, T. Kawanishi, T. Miyazaki, K. Higuma, M. Sudo, and J. Ichikawa, "Reconfigurable multilevel transmitter using monolithically integrated quad mach-zehnder IQ modulator for optical 16-QAM and 8-PSK generation", *Opt. Express*, vol. 19, no. 6, pp. 5596–5601, 2011.

[37] Y. Ehrlichman, O. Amrani, and S. Ruschin, "Generation of M-ary signals using a single mach zehnder interferometer", in *Integrated Optics: Devices, Materials, and Technologies XIII*, International Society for Optics and Photonics, vol. 7218, 2009, p. 72180L.

[38] A. Shastri, C. Muzio, M. Webster, G. Jeans, P. Metz, S. Sunder, B. Chattin, B. Dama, and K. Shastri, "Ultra-low-power single-polarization QAM-16 generation without DAC using a CMOS photonics based segmented modulator", *Journal of Lightwave Technology*, vol. 33, no. 6, pp. 1255–1260, 2015.

[39] M. Vanhoecke, A. Aimone, N. Argyris, S. Dris, R. Vaernewyck, K. Verheyen, M. Gruner, G. Fiol, D. Apostolopoulos, H. Avramopoulos, *et al.*, "Segmented optical transmitter comprising a CMOS driver array and an InP IQ-MZM for advanced modulation formats", *Journal of Lightwave Technology*, vol. 35, no. 4, pp. 862–867, 2017.

[40] T. N. Huynh, N. Dupuis, R. Rimolo-Donadio, J. E. Proesel, D. M. Gill, C. W. Baks, A. V. Rylyakov, C. L. Schow, W. M. Green, and B. G. Lee, "Flexible silicon photonic transmitter with segmented modulator and 32 nm CMOS driver IC", in *Lasers and Electro-Optics (CLEO), 2016 Conference on*, IEEE, 2016, pp. 1–2.

[41] D. A. Morero, M. A. Castrillón, A. Aguirre, M. R. Hueda, and O. E. Agazzi, "Design tradeoffs and challenges in practical coherent optical transceiver implementations", *Journal of Lightwave Technology*, vol. 34, no. 1, pp. 121–136, 2016.

[42] P Poggiolini, A Carena, V Curri, and F Forghieri, "Evaluation of the computational effort for chromatic dispersion compensation in coherent optical PM-OFDM and PM-QAM systems", *Optics express*, vol. 17, no. 3, pp. 1385–1403, 2009.

[43] C. Fougstedt, P. Johannisson, L. Svensson, and P. Larsson-Edefors, "Dynamic equalizer power dissipation optimization", in *Optical Fiber Communication Conference*, Optical Society of America, 2016, W4A–2.

[44] D. Cardenas, D. Lavery, P. Watts, and S. J. Savory, "Reducing the power consumption of the CMA equalizer update for a digital coherent receiver", in *Optical Fiber Communications Conference and Exhibition (OFC), 2014*, IEEE, 2014, pp. 1–3.

[45] D. E. Crivelli, M. R. Hueda, H. S. Carrer, M. Del Barco, R. R. López, P. Gianni, J. M. Finochietto, N. Swenson, P. Voois, and O. E. Agazzi, "Architecture of a single-chip 50 Gb/s DP-QPSK/BPSK transceiver with electronic dispersion compensation for coherent optical channels.", *IEEE Trans. on Circuits and Systems*, vol. 61, no. 4, pp. 1012–1025, 2014.

[46] K. Cushon, P. Larsson-Edefors, and P. Andrekson, "Improved low-power LDPC FEC for coherent optical systems", in *Optical Communication (ECOC), 2017 European Conference on*, IEEE, 2017, pp. 1–3.

[47] G Bergland, "Fast Fourier transform hardware implementations - an overview", *IEEE Transactions on Audio and Electroacoustics*, vol. 17, no. 2, pp. 104–108, 1969.

[48] S. Kilts, *Advanced FPGA design: architecture, implementation, and optimization*. John Wiley & Sons, 2007.

[49] Y.-W. Lin, H.-Y. Liu, and C.-Y. Lee, "A 1-Gs/s FFT/IFFT processor for UWB applications", *IEEE Journal of solid-state circuits*, vol. 40, no. 8, pp. 1726–1735, 2005.

[50] S.-N. Tang, J.-W. Tsai, and T.-Y. Chang, "A 2.4-GS/s FFT processor for OFDM-based WPAN applications", *IEEE Transactions on Circuits and Systems II: Express Briefs*, vol. 57, no. 6, pp. 451–455, 2010.

[51] M. Dreschmann, J. Meyer, M. Hübner, R. Schmogrow, D. Hillerkuss, J. Becker, J. Leuthold, and W. Freude, "Implementation of an ultra-high speed 256-point FFT for Xilinx virtex-6 devices", in *Industrial Informatics (INDIN), 2011 9th IEEE International Conference on*, IEEE, 2011, pp. 829–834.

[52]   T. Pfau, S. Hoffmann, and R. Noé, "Hardware-efficient coherent digital receiver concept with feedforward carrier recovery for M-QAM constellations", *Journal of Lightwave Technology*, vol. 27, no. 8, pp. 989–999, 2009.

[53]   M. Kuschnerov, T. Bex, and P. Kainzmaier, "Energy efficient digital signal processing", in *Optical Fiber Communication Conference*, Optical Society of America, 2014, Th3E–7.

[54]   A. J. Lowery and J. Armstrong, "10 Gbit/s multimode fiber link using power-efficient orthogonal-frequency-division multiplexing", *Optics Express*, vol. 13, no. 25, pp. 10 003–10 009, 2005.

[55]   J. Armstrong and A. Lowery, "Power efficient optical OFDM", *Electronics Letters*, vol. 42, no. 6, pp. 370–372, 2006.

[56]   S. C. J. Lee, S. Randel, F. Breyer, and A. M. Koonen, "PAM-DMT for intensity modulated and direct detection optical communication systems", *IEEE Photonics Technology Letters*, vol. 21, no. 23, pp. 1749–1751, 2009.

[57]   J. Yong, "Modulation and demodulation apparatuses and methods for wired /wireless communication", *Korea Patent WO2007/064*, vol. 165, 2007.

[58]   N. Fernando, Y. Hong, and E. Viterbo, "Flip-OFDM for unipolar communication systems", *IEEE Transactions on Communications*, vol. 60, no. 12, pp. 3726–3733, 2012.

[59]   J. Armstrong and B. J. Schmidt, "Comparison of asymmetrically clipped optical OFDM and DC-biased optical OFDM in AWGN", *IEEE Communications Letters*, vol. 12, no. 5, 2008.

[60]   N. Wu and Y. Bar-Ness, "A novel power-efficient scheme asymmetrically and symmetrically clipping optical (ASCO)-OFDM for IM/DD optical systems", *EURASIP Journal on Advances in Signal Processing*, vol. 2015, no. 1, p. 3, 2015.

[61]   B. Ranjha and M. Kavehrad, "Hybrid asymmetrically clipped OFDM-based IM/DD optical wireless system", *IEEE/OSA Journal of Optical Communications and Networking*, vol. 6, no. 4, pp. 387–396, 2014.

[62]   D. Tsonev, S. Videv, and H. Haas, "Unlocking spectral efficiency in intensity modulation and direct detection systems", *IEEE Journal on Selected Areas in Communications*, vol. 33, no. 9, pp. 1758–1770, 2015.

[63]   L. Chen, B. Krongold, and J. Evans, "Successive decoding of anti-periodic OFDM signals in IM/DD optical channel", in *Communications (ICC), 2010 IEEE International Conference on*, IEEE, 2010, pp. 1–6.

[64] E. Lam, S. K. Wilson, H. Elgala, and T. D. Little, "Spectrally and energy efficient OFDM (SEE-OFDM) for intensity modulated optical wireless systems", *arXiv preprint arXiv:1510.08172*, 2015.

[65] Q. Wang, C. Qian, X. Guo, Z. Wang, D. G. Cunningham, and I. H. White, "Layered ACO-OFDM for intensity-modulated direct-detection optical wireless transmission", *Optics Express*, vol. 23, no. 9, pp. 12 382–12 393, 2015.

[66] A. J. Lowery, "Comparisons of spectrally-enhanced asymmetrically clipped optical OFDM systems", *Optics Express*, vol. 24, no. 4, pp. 3950–3966, 2016.

[67] M. S. Islim, D. Tsonev, and H. Haas, "On the superposition modulation for OFDM-based optical wireless communication", in *Signal and Information Processing (GlobalSIP), 2015 IEEE Global Conference on*, IEEE, 2015, pp. 1022–1026.

[68] M. S. Islim and H. Haas, "Augmenting the spectral efficiency of enhanced PAM-DMT-based optical wireless communications", *Optics Express*, vol. 24, no. 11, pp. 11 932–11 949, 2016.

[69] D. Law, D. Dove, J. D'Ambrosia, M. Hajduczenia, M. Laubach, and S. Carlson, "Evolution of Ethernet standards in the IEEE 802.3 working group", *IEEE Communications Magazine*, vol. 51, no. 8, pp. 88–96, 2013.

[70] P. Winzer, "Beyond 100G Ethernet", *IEEE Communications Magazine*, vol. 48, no. 7, 2010.

[71] Y. Matsui, T. Pham, T. Sudo, G. Carey, B. Young, and C. Roxlo, "112-Gb/s WDM link using two directly modulated Al-MQW BH DFB lasers at 56 gb/s", in *Optical Fiber Communication Conference*, Optical Society of America, 2015, Th5B–6.

[72] C. Chen, X. Tang, and Z. Zhang, "Transmission of 56-Gb/s PAM-4 over 26-km single mode fiber using maximum likelihood sequence estimation", in *Optical Fiber Communication Conference*, Optical Society of America, 2015, Th4A–5.

[73] N. Stojanovic, Z. Qiang, C. Prodaniuc, and F. Karinou, "Performance and DSP complexity evaluation of a 112-Gbit/s PAM-4 transceiver employing a 25-Ghz TOSA and ROSA", in *Optical Communication (ECOC), 2015 European Conference on*, IEEE, 2015, pp. 1–3.

[74] H. Yamazaki, M. Nagatani, S. Kanazawa, H. Nosaka, T. Hashimoto, A. Sano, and Y. Miyamoto, "160-Gbps Nyquist PAM4 transmitter using a digital-preprocessed analog-multiplexed DAC", in *Optical Communication (ECOC), 2015 European Conference on*, IEEE, 2015, pp. 1–3.

[75] L. E. Nelson, "Advances in 400 Gigabit Ethernet field trials", in *Optical Fiber Communication Conference*, Optical Society of America, 2018, W1B.1.

[76] M. H. Eiselt, N. Eiselt, and A. Dochhan, "Direct-detection solutions for 100G and beyond", in *Optical Fiber Communication Conference*, Optical Society of America, 2017, Tu3I–3.

[77] J. Wei, Q. Cheng, R. V. Penty, I. H. White, and D. G. Cunningham, "400 Gigabit Ethernet using advanced modulation formats: performance, complexity, and power dissipation", *IEEE Communications Magazine*, vol. 53, no. 2, pp. 182–189, 2015.

[78] N. Cvijetic, "OFDM for next-generation optical access networks", *Journal of lightwave technology*, vol. 30, no. 4, pp. 384–398, 2012.

[79] A. J. Lowery and L. B. Du, "Optical orthogonal division multiplexing for long haul optical communications: a review of the first five years", *Optical Fiber Technology*, vol. 17, no. 5, pp. 421–438, 2011.

[80] S. Randel, F. Breyer, S. C. Lee, and J. W. Walewski, "Advanced modulation schemes for short-range optical communications", *IEEE Journal of Selected Topics in Quantum Electronics*, vol. 16, no. 5, pp. 1280–1289, 2010.

[81] J. Wei, J. Ingham, D. Cunningham, R. Penty, and I. White, "Performance and power dissipation comparisons between 28 Gb/s NRZ, PAM, CAP and optical OFDM systems for data communication applications", *Journal of Lightwave Technology*, vol. 30, no. 20, pp. 3273–3280, 2012.

[82] J. Wei, D. Cunningham, R. Penty, and I. White, "Study of 100 Gigabit Ethernet using carrierless amplitude/phase modulation and optical OFDM", *Journal of Lightwave Technology*, vol. 31, no. 9, pp. 1367–1373, 2013.

[83] K. Kikuchi, "Fundamentals of coherent optical fiber communications", *journal of Lightwave Technology*, vol. 34, no. 1, pp. 157–179, 2016.

[84] B. Spinnler, "Equalizer design and complexity for digital coherent receivers", *IEEE Journal of Selected Topics in Quantum Electronics*, vol. 16, no. 5, pp. 1180–1192, 2010.

[85] K. Ho, "Subband equaliser for chromatic dispersion of optical fibre", *Electronics letters*, vol. 45, no. 24, p. 1, 2009.

[86] R. Kudo, T. Kobayashi, K. Ishihara, Y. Takatori, A. Sano, E. Yamada, H. Masuda, and Y. Miyamoto, "PMD compensation in optical coherent single carrier transmission using frequency-domain equalisation", *Electronics Letters*, vol. 45, no. 2, pp. 124–125, 2009.

[87] E. Ip, A. P. T. Lau, D. J. Barros, and J. M. Kahn, "Coherent detection in optical fiber systems", *Optics express*, vol. 16, no. 2, pp. 753–791, 2008.

[88] M. Kuschnerov, F. N. Hauske, K. Piyawanno, B. Spinnler, M. S. Alfiad, A. Napoli, and B. Lankl, "DSP for coherent single-carrier receivers", *Journal of lightwave technology*, vol. 27, no. 16, pp. 3614–3622, 2009.

[89] S. J. Savory, "Digital coherent optical receivers: algorithms and subsystems", *IEEE Journal of Selected Topics in Quantum Electronics*, vol. 16, no. 5, pp. 1164–1179, 2010.

[90] J.-P. Elbers, N. Eiselt, A. Dochhan, D. Rafique, and H. Grießer, "PAM4 vs coherent for DCI applications", in *Signal Processing in Photonic Communications*, Optical Society of America, 2017, SpTh2D–1.

[91] K. Zhong, X. Zhou, J. Huo, C. Yu, C. Lu, and A. P. T. Lau, "Digital signal processing for short-reach optical communications: a review of current technologies and future trends", *Journal of Lightwave Technology*, vol. 36, no. 2, pp. 377–400, 2018.

[92] S. Bae, H. Kim, and Y. Chung, "Transmission of 51.56-Gb/s OOK signal using 1.55-μm directly modulated laser and duobinary electrical equalizer", *Optics express*, vol. 24, no. 20, pp. 22 555–22 562, 2016.

[93] A. Dochhan, H. Griesser, N. Eiselt, M. H. Eiselt, and J.-P. Elbers, "Solutions for 80 km DWDM systems", *Journal of Lightwave Technology*, vol. 34, no. 2, pp. 491–499, 2016.

[94] M. Sharif, J. K. Perin, and J. M. Kahn, "Modulation schemes for single-laser 100 Gb/s links: single-carrier", *Journal of Lightwave Technology*, vol. 33, no. 20, pp. 4268–4277, 2015.

[95] IEEE, *The zettabyte era: trends and analysis,* `https://ieeexplore.ieee.org/document/8207825/`.

[96] W. Wang, P. Zhao, Z. Zhang, H. Li, D. Zang, N. Zhu, and Y. Lu, "First demonstration of 112 Gb/s PAM-4 amplifier-free transmission over a record reach of 40 km using 1.3 μm directly modulated laser", in *Optical Fiber Communication Conference*, Optical Society of America, 2018, Th4B–8.

[97] J. Tatum, G. Landry, D. Gazula, J. K. Wade, and P. Westbergh, "VCSEL-based optical transceivers for future data center applications", in *Optical Fiber Communication Conference*, Optical Society of America, 2018, M3F–6.

[98]   R. Rodes, M. Müeller, B. Li, J. Estaran, J. B. Jensen, T. Gruendl, M. Ortsiefer, C. Neumeyr, J. Rosskopf, K. J. Larsen, *et al.*, "High-speed 1550 nm VCSEL data transmission link employing 25 GBd 4-PAM modulation and hard decision forward error correction", *Journal of Lightwave Technology*, vol. 31, no. 4, pp. 689–695, 2013.

[99]   R. Rodes, J. Estaran, B. Li, M. Mueller, J. B. Jensen, T. Gründl, M. Ortsiefer, C. Neumeyr, J. Rosskopf, K. J. Larsen, *et al.*, "100 Gb/s single VCSEL data transmission link", in *Optical Fiber Communication Conference*, Optical Society of America, 2012, PDP5D–10.

[100] N. Eiselt, H. Griesser, J. Wei, R. Hohenleitner, A. Dochhan, M. Ortsiefer, M. H. Eiselt, C. Neumeyr, J. J. V. Olmos, and I. T. Monroy, "Experimental demonstration of 84 Gb/s PAM-4 over up to 1.6 km SSMF using a 20-GHz VCSEL at 1525 nm", *Journal of Lightwave Technology*, vol. 35, no. 8, pp. 1342–1349, 2017.

[101] Q. Zhang, N. Stojanovic, C. Prodaniuc, C. Xie, M. Koenigsmann, and P. Laskowski, "Single-lane 180 Gbit/s PAM-4 signal transmission over 2 km SSMF for short-reach applications", *Optics letters*, vol. 41, no. 19, pp. 4449–4452, 2016.

[102] K. Zhong, X. Zhou, T. Gui, L. Tao, Y. Gao, W. Chen, J. Man, L. Zeng, A. P. T. Lau, and C. Lu, "Experimental study of PAM-4, CAP-16, and DMT for 100 Gb/s short reach optical transmission systems", *Optics express*, vol. 23, no. 2, pp. 1176–1189, 2015.

[103] L. Sun, J. Du, and Z. He, "Multiband three-dimensional carrierless amplitude phase modulation for short reach optical communications", *Journal of Lightwave Technology*, vol. 34, no. 13, pp. 3103–3109, 2016.

[104] M. I. Olmedo, T. Zuo, J. B. Jensen, Q. Zhong, X. Xu, S. Popov, and I. T. Monroy, "Multiband carrierless amplitude phase modulation for high capacity optical data links", *Journal of Lightwave Technology*, vol. 32, no. 4, pp. 798–804, 2014.

[105] J. Shi, J. Zhang, X. Li, N. Chi, G.-K. Chang, and J. Yu, "112 Gb/s/λ CAP signals transmission over 480 km in IM-DD system", in *Optical Fiber Communication Conference*, Optical Society of America, 2018, W1J.5.

[106] B. J. Schmidt, A. J. Lowery, and J. Armstrong, "Experimental demonstrations of electronic dispersion compensation for long-haul transmission using direct-detection optical OFDM", *Journal of Lightwave Technology*, vol. 26, no. 1, pp. 196–203, 2008.

[107] A. J. Lowery, L. B. Du, and J. Armstrong, "Performance of optical OFDM in ultralong-haul WDM lightwave systems", *Journal of Lightwave Technology*, vol. 25, no. 1, pp. 131–138, 2007.

[108] E. d. V. Pereira, R. d. O. Helder, R. B. Nunes, M. E. Segatto, and J. A. Silva, "Impact of optical power in the guard-band reduction of an optimized DDO-OFDM system", *Journal of Lightwave Technology*, vol. 33, no. 23, pp. 4717–4725, 2015.

[109] J.-H. Yan, Y.-W. Chen, B.-C. Tsai, and K.-M. Feng, "A multiband DDO-OFDM system with spectral efficient iterative SSBI reduction DSP", *IEEE Photonics Technol. Lett.*, vol. 28, no. 2, pp. 119–122, 2016.

[110] W.-R. Peng, B. Zhang, K.-M. Feng, X. Wu, A. E. Willner, and S. Chi, "Spectrally efficient direct-detected OFDM transmission incorporating a tunable frequency gap and an iterative detection techniques", *Journal of Lightwave Technology*, vol. 27, no. 24, pp. 5723–5735, 2009.

[111] W.-R. Peng, X. Wu, V. R. Arbab, K.-M. Feng, B. Shamee, L. C. Christen, J.-Y. Yang, A. E. Willner, and S. Chi, "Theoretical and experimental investigations of direct-detected RF-tone-assisted optical OFDM systems", *Journal of Lightwave Technology*, vol. 27, no. 10, pp. 1332–1339, 2009.

[112] W. Shieh, H. Bao, and Y Tang, "Coherent optical OFDM: theory and design", *Optics Express*, vol. 16, no. 2, pp. 841–859, 2008.

[113] S. L. Jansen, I. Morita, T. C. Schenk, N. Takeda, and H. Tanaka, "Coherent optical 25.8-Gb/s OFDM transmission over 4160-km SSMF", *Journal of Lightwave Technology*, vol. 26, no. 1, pp. 6–15, 2008.

[114] Y. Tang, W. Shieh, X. Yi, and R. Evans, "Optimum design for RF-to-optical up-converter in coherent optical OFDM systems", *IEEE Photonics Technology Letters*, vol. 19, no. 5/8, p. 483, 2007.

[115] X. Yi, W. Shieh, and Y. Tang, "Phase estimation for coherent optical OFDM", *IEEE Photonics Technology Letters*, vol. 19, no. 9/12, p. 919, 2007.

[116] Z. Liu, B. Kelly, J. O'Carroll, R. Phelan, D. J. Richardson, and R. Slavík, "Discrete multitone format for repeater-less direct-modulation direct detection over 150 km", *Journal of Lightwave Technology*, vol. 34, no. 13, pp. 3223–3229, 2016.

[117] D. Pilori, C. Fludger, and R. Gaudino, "Comparing DMT variants in medium reach 100G optically amplified systems", *Journal of Lightwave Technology*, vol. 34, no. 14, pp. 3389–3399, 2016.

[118]   G. N. Liu, L. Zhang, T. Zuo, and Q. Zhang, "IM/DD transmission tech-
        niques for emerging 5G fronthaul, DCI, and metro applications", *Journal
        of Lightwave Technology*, vol. 36, no. 2, pp. 560–567, 2018.

[119]   Y. Benlachtar, R. Bouziane, R. I. Killey, C. R. Berger, P. Milder, R. Koutsoy-
        annis, J. C. Hoe, M. Püschel, and M. Glick, "Optical OFDM for the data
        center", in *Transparent Optical Networks (ICTON), 2010 12th International
        Conference on*, IEEE, 2010, pp. 1–4.

[120]   T. Takahara, T. Tanaka, M. Nishihara, Y. Kai, L. Li, Z. Tao, and J. Ras-
        mussen, "Discrete multi-tone for 100 Gb/s optical access networks", in
        Optical Fiber Communication Conference, Optical Society of America, 2014,
        pp. M2I–1.

[121]   J. Lee, "Discrete multitone modulation for short-range optical communi-
        cations", *Eindhoven: Technische Universiteit Eindhoven*, 2009.

[122]   C. Xie, P. Dong, S. Randel, D. Pilori, P. J. Winzer, S. Spiga, B. Kögel, C.
        Neumeyr, and M. Amann, "Single-VCSEL 100-Gb/s short-reach system
        using discrete multi-tone modulation and direct detection", in *Optical Fiber
        Communication Conference*, Optical Society of America, 2015, Tu2H–2.

[123]   J. Lee, P. Dong, N. Kaneda, and Y.-K. Chen, "Discrete multi-tone transmis-
        sion for short-reach optical connections", in *Optical Fiber Communication
        Conference*, Optical Society of America, 2016, Th1G–1.

[124]   H. Yang, S. J. Lee, E. Tangdiongga, C. Okonkwo, H. P. van den Boom, F.
        Breyer, S. Randel, and A. Koonen, "47.4 Gb/s transmission over 100 m
        graded-index plastic optical fiber based on rate-adaptive discrete multi-
        tone modulation", *Journal of Lightwave Technology*, vol. 28, no. 4, pp. 352–
        359, 2010.

[125]   C. Kottke, C. Caspar, V. Jungnickel, R. Freund, M. Agustin, and N. Ledent-
        sov, "High speed 160 Gb/s DMT VCSEL transmission using preequaliza-
        tion", in *Optical Fiber Communication Conference*, Optical Society of Amer-
        ica, 2017, W4I–7.

[126]   L. Zhang, T. Zuo, Y. Mao, Q. Zhang, E. Zhou, G. N. Liu, and X. Xu, "Be-
        yond 100-Gb/s transmission over 80-km SMF using direct-detection SSB-
        DMT at C-band", *Journal of Lightwave Technology*, vol. 34, no. 2, pp. 723–
        729, 2016.

[127] R Okabe, B Liu, M Nishihara, T Tanaka, T Takahara, L Li, Z Tao, and J. Rasmussen, "Unrepeated 100 km SMF transmission of 110.3 Gbps/lambda DMT signal", in *Optical Communication (ECOC), 2015 European Conference on*, IEEE, 2015, pp. 1–3.

[128] S. Randel, D. Pilori, S Chandrasekhar, G. Raybon, and P. Winzer, "100-Gb/s discrete-multitone transmission over 80-km SSMF using single sideband modulation with novel interference-cancellation scheme", in *Optical Communication (ECOC), 2015 European Conference on*, IEEE, 2015, pp. 1–3.

[129] C. Y. Wong, S. Zhang, L. Liu, T. Wang, Q. Zhang, Y. Fang, S. Deng, G. N. Liu, *et al.*, "56 Gb/s direct detected single-sideband DMT transmission over 320-km SMF using silicon IQ modulator", in *Optical Fiber Communication Conference*, Optical Society of America, 2015, Th4A–3.

[130] Y.-H. Wang, C.-C. Wei, H. Taga, and T. Tsuritani, "Novel IM/DD single-sideband OFDM generation featuring tolerance to dispersion-related fading and distortion", in *ECOC 2016; 42nd European Conference on Optical Communication; Proceedings of*, VDE, 2016, pp. 1–3.

[131] J. Zhou, L. Zhang, T. Zuo, Q. Zhang, S. Zhang, E. Zhou, and G. N. Liu, "Transmission of 100-Gb/s DSB-DMT over 80-km SMF using 10-G class TTA and direct-detection", in *ECOC 2016; 42nd European Conference on Optical Communication; Proceedings of*, VDE, 2016, pp. 1–3.

[132] L. Zhang, T. Zuo, Q. Zhang, J. Zhou, E. Zhou, and G. N. Liu, "150-Gb/s DMT over 80-km SMF transmission based on spectrally efficient SSBI cancellation using guard-band twin-SSB technique", in *ECOC 2016; 42nd European Conference on Optical Communication; Proceedings of*, VDE, 2016, pp. 1–3.

[133] L. Zhang, T. Zuo, Q. Zhang, J. Zhou, E. Zhou, and G. N. Liu, "Single wavelength 248-Gb/s transmission over 80-km SMF based on twin-SSB-DMT and direct detection", in *ECOC 2016; 42nd European Conference on Optical Communication*, 2016.

[134] M. G. Taylor, "Coherent detection method using DSP for demodulation of signal and subsequent equalization of propagation impairments", *IEEE Photonics Technology Letters*, vol. 16, no. 2, pp. 674–676, 2004.

[135] K. Kikuchi, "Phase-diversity homodyne detection of multilevel optical modulation with digital carrier phase estimation", *IEEE Journal of Selected Topics in Quantum Electronics*, vol. 12, no. 4, pp. 563–570, 2006.

[136]   S. J. Savory, G. Gavioli, R. I. Killey, and P. Bayvel, "Electronic compensation of chromatic dispersion using a digital coherent receiver", *Optics express*, vol. 15, no. 5, pp. 2120–2126, 2007.

[137]   S. J. Savory, "Digital filters for coherent optical receivers", *Optics express*, vol. 16, no. 2, pp. 804–817, 2008.

[138]   S. Tsukamoto, K. Katoh, and K. Kikuchi, "Coherent demodulation of optical multilevel phase-shift-keying signals using homodyne detection and digital signal processing", *IEEE Photonics Technology Letters*, vol. 18, no. 10, pp. 1131–1133, 2006.

[139]   Y. Mori, C. Zhang, K. Igarashi, K. Katoh, and K. Kikuchi, "Unrepeated 200-km transmission of 40-Gbit/s 16-QAM signals using digital coherent receiver", *Optics Express*, vol. 17, no. 3, pp. 1435–1441, 2009.

[140]   P. M. Watts, R. Waegemans, Y. Benlachtar, V. Mikhailov, P. Bayvel, and R. I. Killey, "10.7 Gb/s transmission over 1200 km of standard single-mode fiber by electronic predistortion using FPGA-based real-time digital signal processing", *Optics Express*, vol. 16, no. 16, pp. 12 171–12 180, 2008.

[141]   R. Waegemans, S. Herbst, L. Holbein, P. Watts, P. Bayvel, C. Fürst, and R. I. Killey, "10.7 Gb/s electronic predistortion transmitter using commercial FPGAs and D/A converters implementing real-time DSP for chromatic dispersion and SPM compensation", *Optics express*, vol. 17, no. 10, pp. 8630–8640, 2009.

[142]   T. Pfau, S. Hoffmann, R. Peveling, S. Bhandare, S. K. Ibrahim, O. Adamczyk, M. Porrmann, R. Noé, and Y. Achiam, "First real-time data recovery for synchronous QPSK transmission with standard DFB lasers", *IEEE Photonics Technology Letters*, vol. 18, no. 18, pp. 1907–1909, 2006.

[143]   T. Pfau, R. Peveling, J. Hauden, N. Grossard, H. Porte, Y. Achiam, S. Hoffmann, S. K. Ibrahim, O. Adamczyk, S. Bhandare, *et al.*, "Coherent digital polarization diversity receiver for real-time polarization-multiplexed QPSK transmission at 2.8 Gb/s", *IEEE Photonics Technology Letters*, vol. 19, no. 24, pp. 1988–1990, 2007.

[144]   N. Eiselt, H. Griesser, J. Wei, A. Dochhan, M. Eiselt, J.-P. Elbers, J. J. V. Olmos, and I. T. Monroy, "Real-time evaluation of 26-GBaud PAM-4 intensity modulation and direct detection systems for data-center interconnects", in *Optical Fiber Communications Conference and Exhibition (OFC), 2016*, IEEE, 2016, pp. 1–3.

[145] N. Eiselt, J. Wei, H. Griesser, A. Dochhan, M. Eiselt, J.-P. Elbers, J. J. V. Olmos, and I. T. Monroy, "First real-time 400G PAM-4 demonstration for inter-data center transmission over 100 km of SSMF at 1550 nm", in *Optical Fiber Communications Conference and Exhibition (OFC), 2016*, IEEE, 2016, pp. 1–3.

[146] Y. F. Chang, "Link performance investigation of industry first 100G PAM4 IC chipset with real-time DSP for data center connectivity", in *Optical Fiber Communication Conference*, Optical Society of America, 2016, Th1G–2.

[147] A. Josten, B. Bäuerle, M. Eppenberger, E. Dornbierer, D. Hillerkuss, and J. Leuthold, "168 Gb/s line rate real-time PAM receiver enabled by timing recovery with 8/7 oversampling in a single FPGA", in *Optical Fiber Communication Conference*, Optical Society of America, 2017, W2A–24.

[148] S. L. Jansen, I. Morita, N. Takeda, and H. Tanaka, "20-Gb/s OFDM transmission over 4160-km SSMF enabled by RF-pilot tone phase noise compensation", in *National Fiber Optic Engineers Conference*, Optical Society of America, 2007, PDP15.

[149] S. L. Jansen, I. Morita, T. C. Schenk, and H. Tanaka, "121.9-Gb/s PDM-OFDM transmission with 2-b/s/Hz spectral efficiency over 1000 km of SSMF", *Journal of Lightwave Technology*, vol. 27, no. 3, pp. 177–188, 2009.

[150] A Sano, E Yamada, H Masuda, E Yamazaki, T Kobayashi, E Yoshida, Y Miyamoto, S Matsuoka, R Kudo, K Ishihara, *et al.*, "13.4-Tb/s (134× 111-Gb/s/ch) no-guard-interval coherent OFDM transmission over 3,600 km of SMF with 19-ps average PMD", in *Optical Communication, 2008. ECOC 2008. 34th European Conference on*, IEEE, 2008, pp. 1–2.

[151] Q. Yang, S. Chen, Y. Ma, and W. Shieh, "Real-time reception of multi-gigabit coherent optical OFDM signals", *Optics express*, vol. 17, no. 10, pp. 7985–7992, 2009.

[152] S. Chen, Q. Yang, Y. Ma, and W. Shieh, "Real-time multi-gigabit receiver for coherent optical MIMO-OFDM signals", *Journal of Lightwave Technology*, vol. 27, no. 16, pp. 3699–3704, 2009.

[153] N. Kaneda, Q. Yang, X. Liu, S Chandrasekhar, W. Shieh, and Y.-K. Chen, "Real-time 2.5 GS/s coherent optical receiver for 53.3-Gb/s sub-banded OFDM", *Journal of Lightwave Technology*, vol. 28, no. 4, pp. 494–501, 2010.

[154]   R Schmogrow, M Winter, D Hillerkuss, B Nebendahl, S Ben-Ezra, J Meyer, M Dreschmann, M Huebner, J Becker, C Koos, *et al.*, "Real-time OFDM transmitter beyond 100 Gbit/s", *Optics express*, vol. 19, no. 13, pp. 12 740–12 749, 2011.

[155]   B. Inan, S. Adhikari, O. Karakaya, P. Kainzmaier, M. Mocker, H. von Kirchbauer, N. Hanik, and S. L. Jansen, "Real-time 93.8-Gb/s polarization multiplexed OFDM transmitter with 1024-point IFFT", *Optics express*, vol. 19, no. 26, B64–B68, 2011.

[156]   N. Kaneda, T. Pfau, H. Zhang, J. Lee, Y.-K. Chen, C. J. Youn, Y. H. Kwon, E. S. Num, and S Chandrasekhar, "Field demonstration of 100-Gb/s real-time coherent optical OFDM detection", *Journal of Lightwave Technology*, vol. 33, no. 7, pp. 1365–1372, 2015.

[157]   X. Xiao, F. Li, J Yu, X Li, Y Xia, and F Chen, "100-Gb/s single-band real-time coherent optical DP-16QAM-OFDM transmission and reception", in *Optical Fiber Communications Conference and Exhibition (OFC), 2014*, IEEE, 2014, pp. 1–3.

[158]   S. Lee, F Breyer, D Cardenas, S Randel, and A. Koonen, "Real-time gigabit DMT transmission over plastic optical fibre", *Electronics letters*, vol. 45, no. 25, pp. 1342–1343, 2009.

[159]   Y. Benlachtar, P. M. Watts, R. Bouziane, P. Milder, D. Rangaraj, A. Cartolano, R. Koutsoyannis, J. C. Hoe, M. Püschel, M. Glick, *et al.*, "Generation of optical OFDM signals using 21.4 GS/s real time digital signal processing", *Optics Express*, vol. 17, no. 20, pp. 17 658–17 668, 2009.

[160]   X. Jin, R. Giddings, and J. Tang, "Real-time transmission of 3Gb/s 16-QAM encoded optical OFDM signals over 75km SMFs with negative power penalties", *Optics Express*, vol. 17, no. 17, pp. 14 574–14 585, 2009.

[161]   R. Giddings, X. Jin, E Hugues-Salas, E Giacoumidis, J. Wei, and J. Tang, "Experimental demonstration of a record high 11.25 Gb/s real-time optical OFDM transceiver supporting 25km SMF end-to-end transmission in simple IMDD systems", *Optics Express*, vol. 18, no. 6, pp. 5541–5555, 2010.

[162]   F. Li, X. Xiao, X. Li, and Z. Dong, "Real-time demonstration of DMT-based DDO-OFDM transmission and reception at 50Gb/s", in *Optical Communication (ECOC 2013), 39th European Conference and Exhibition on*, IET, 2013, pp. 1–3.

[163] X. Xiao, F. Li, J. Yu, Y. Xia, and Y. Chen, "Real-time demonstration of 100Gbps class dual-carrier DDO-16QAM-DMT transmission with directly modulated laser", in *OFC 2014*, 2014, pp. 1–3.

[164] F. Li, X. Xiao, J. Yu, J. Zhang, and X. Li, "Real-time direct-detection of quad-carrier 200Gbps 16QAM-DMT with directly modulated laser", in *Optical Communication (ECOC), 2015 European Conference on*, IEEE, 2015, pp. 1–3.

[165] S. D. Brown, *Fundamentals of digital logic with Verilog design*. Tata McGraw-Hill Education, 2007.

[166] Xilinx, *Xilinx UG369 Virtex-6 FPGA DSP48E1 slice, user guide*, `https://www.xilinx.com/support/documentation/user_guides/ug369.pdf`.

[167] MICRAM, *VEGA DAC II*, `http://micram.net/wp-content/uploads/2014/08/Micram-VEGA-DAC-II-Data-Sheet.pdf`.

[168] J. K. Perin, M. Sharif, and J. M. Kahn, "Modulation schemes for single-laser 100 Gb/s links: multicarrier", *Journal of Lightwave Technology*, vol. 33, no. 24, pp. 5122–5132, 2015.

[169] H. V. Sorensen, D Jones, M. Heideman, and C Burrus, "Real-valued fast Fourier transform algorithms", *IEEE Transactions on Acoustics, Speech, and Signal Processing*, vol. 35, no. 6, pp. 849–863, 1987.

[170] V. Oksman and S. Galli, "G. hn: the new itu-t home networking standard", *IEEE Communications Magazine*, vol. 47, no. 10, 2009.

[171] F. Barrami, Y. Le Guennec, E. Novakov, J.-M. Duchamp, and P. Busson, "A novel FFT/IFFT size efficient technique to generate real time optical OFDM signals compatible with IM/DD systems", in *Microwave Conference (EuMC), 2013 European*, IEEE, 2013, pp. 1247–1250.

[172] C. Aupetit-Berthelemot and M. F. O. Sanya, "An IFFT/FFT size efficient improved ACO-OFDM scheme for next-generation passive optical network", in *Networks and Optical Communications (NOC), 2016 21st European Conference on*, IEEE, 2016, pp. 111–116.

[173] M. F. Sanya, L. Djogbe, A Vianou, and C Aupetit-Berthelemot, "DC-biased optical OFDM for IM/DD passive optical network systems", *Journal of Optical Communications and Networking*, vol. 7, no. 4, pp. 205–214, 2015.

[174] M. Chen, X. Xiao, Z. R. Huang, J. Yu, F. Li, Q. Chen, and L. Chen, "Experimental demonstration of an IFFT/FFT size efficient DFT-spread OFDM for short reach optical transmission systems", *Journal of Lightwave Technology*, vol. 34, no. 9, pp. 2100–2105, 2016.

[175] C. Chen, W.-D. Zhong, and D. Wu, "Non-Hermitian symmetry orthogonal frequency division multiplexing for multiple-input multiple-output visible light communications", *IEEE/OSA Journal of Optical Communications and Networking*, vol. 9, no. 1, pp. 36–44, 2017.

[176] R. Bouziane, P. Milder, R. Koutsoyannis, Y. Benlachtar, J. Hoe, M. Glick, and R. Killey, "Dependence of optical OFDM transceiver ASIC complexity on FFT size", in *Optical Fiber Communication Conference*, Optical Society of America, 2012, JW2A–58.

[177] L. Chen, B. Krongold, and J. Evans, "Diversity combining for asymmetrically clipped optical OFDM in IM/DD channels", in *Global Telecommunications Conference, 2009. GLOBECOM 2009. IEEE*, IEEE, 2009, pp. 1–6.

[178] S. D. Dissanayake and J. Armstrong, "Novel techniques for combating DC offset in diversity combined ACO-OFDM", *IEEE Communications Letters*, vol. 15, no. 11, pp. 1237–1239, 2011.

[179] T. Liu, "A novel scheme for demodulation of ACO-OFDM in the presence of DC offset", *Journal of the Franklin Institute*, vol. 352, no. 3, pp. 802–812, 2015.

[180] P. Milder, F. Franchetti, J. C. Hoe, and M. Püschel, "Computer generation of hardware for linear digital signal processing transforms", *ACM Transactions on Design Automation of Electronic Systems (TODAES)*, vol. 17, no. 2, p. 15, 2012.

[181] R Schmogrow, D Hillerkuss, M Dreschmann, M Huebner, M Winter, J Meyer, B Nebendahl, C Koos, J Becker, W Freude, *et al.*, "Real-time software defined multiformat transmitter generating 64QAM at 28 GBd", *IEEE Photonics Technology Letters*, vol. 22, no. 21, pp. 1601–1603, 2010.

[182] P. Winzer, C Woodworth, F Fidler, P. Reddy, H Song, and A Adamiecki, "Temporal alignment of high-speed transmit channels of FPGA", *Electronics Letters*, vol. 44, no. 2, pp. 113–114, 2008.

[183] B. Song, C. Zhu, B. Corcoran, Q. Wang, L. Zhuang, and A. J. Lowery, "Experimental layered/enhanced ACO-OFDM short-haul optical fiber link", *IEEE Photonics Technology Letters*, vol. 28, no. 24, pp. 2815–2818, 2016.

[184] W. Yan, B. Liu, L. Li, Z. Tao, T. Takahara, and J. C. Rasmussen, "Nonlinear distortion and DSP-based compensation in metro and access networks using discrete multi-tone", in *European Conference and Exhibition on Optical Communication*, Optical Society of America, 2012, Mo–1.

[185] N. S. André, K. Habel, H. Louchet, and A. Richter, "Adaptive nonlinear Volterra equalizer for mitigation of chirp-induced distortions in cost effective IMDD OFDM systems", *Optics Express*, vol. 21, no. 22, pp. 26 527–26 532, 2013.

[186] A. Zhu and T. J. Brazil, "Behavioral modeling of RF power amplifiers based on pruned Volterra series", *IEEE Microwave and Wireless components letters*, vol. 14, no. 12, pp. 563–565, 2004.

[187] M. Chen, J. He, and L. Chen, "Real-time demonstration of 1024-QAM OFDM transmitter in short-reach IMDD systems", *IEEE Photonics Technology Letters*, vol. 27, no. 8, pp. 824–827, 2015.

[188] R Singleton, "A method for computing the fast Fourier transform with auxiliary memory and limited high-speed storage", *IEEE Transactions on Audio and Electroacoustics*, vol. 15, no. 2, pp. 91–98, 1967.

[189] E. O. Brigham and E. O. Brigham, *The fast Fourier transform and its applications*. prentice Hall Englewood Cliffs, NJ, 1988, vol. 448.

[190] H. Lin and P. Siohan, "OFDM/OQAM with hermitian symmetry: design and performance for baseband communication", in *Communications, 2008. ICC'08. IEEE International Conference on*, IEEE, 2008, pp. 652–656.

[191] R. A. Horn, R. A. Horn, and C. R. Johnson, *Matrix analysis*. Cambridge university press, 1990.

[192] Q. Yang, W. Shieh, and Y. Ma, "Bit and power loading for coherent optical OFDM", *IEEE Photonics Technology Letters*, vol. 20, no. 15, pp. 1305–1307, 2008.

[193] D. Bykhovsky and S. Arnon, "An experimental comparison of different bit-and-power-allocation algorithms for DCO-OFDM", *Journal of Lightwave Technology*, vol. 32, no. 8, pp. 1559–1564, 2014.

[194] Xilinx, *Virtex-6 FPGA GTX Transceivers - User Guide*, `http://www.xilinx.com/support/documentation/user_guides/ug366.pdf`.